5-1-2011

Hydrogenated amorphous silicon photonics

Karthik Narayanan

HYDROGENATED AMORPHOUS SILICON PHOTONICS

by

KARTHIK NARAYANAN

A DISSERTATION

Submitted in partial fulfillment for the requirements
For the degree of Doctor of Philosophy
in
Microsystems Engineering
at the
Rochester Institute of Technology

May 2011

Author:

_____

Microsystems Engineering Program

Certified by:

_____

Stefan F. Preble, Ph.D.
Assistant Professor of Microsystems Engineering

Approved by:

_____

Bruce W. Smith, Ph.D.
Director of Microsystems Engineering Program

Certified by:

_____

Harvey J. Palmer, Ph.D.
Dean, Kate Gleason College of Engineering

NOTICE OF COPYRIGHT

REPRODUCITON PERMISSION STATEMENT

Permission Granted

TITLE:

"Hydrogenated Amorphous Silicon Photonics"

I, *Karthik Narayanan*, hereby grant permission to the Wallace Library of Rochester Institute of Technology to reproduce my dissertation in whole or part. Any reproduction will not be for commercial use or profit.

Signature of Author: _____ Date:_____

HYDROGENATED AMORPHOUS SILICON PHOTONICS

By

Karthik Narayanan

Submitted by Karthik Narayanan in partial fulfillment of the requirements for the degree of Doctor of Philosophy in Microsystems Engineering and accepted on behalf of the Rochester Institute of Technology by the dissertation committee.

We, the undersigned members of the Faculty of the Rochester Institute of Technology, certify that we have advised and/or supervised the candidate on the work described in this dissertation. We further certify that we have reviewed the dissertation manuscript and approve it in partial fulfillment of the requirements of the degree of Doctor of Philosophy in Microsystems Engineering.

Dr. Stefan F. Preble _____
(Committee Chair and Dissertation Advisor)

Dr. Sean L. Rommel _____

Dr. Seth Hubbard _____

Dr. Zhaolin Lu _____

Dr. Bruce W. Smith _____
(Director, Microsystems Engineering)

Dr. Harvey J. Palmer _____
(Dean, Kate Gleason College of Engineering)

MICROSYSTEMS ENGINEERING PROGRAM
ROCHESTER INSTITUTE OF TECHNOLOGY

ABSTRACT

Kate Gleason College of Engineering
Rochester institute of Technology

Degree Doctor of Philosophy **Program** Microsystems Engineering

Name of Candidate Karthik Narayanan

Title Hydrogenated Amorphous Silicon Photonics

Silicon Photonics is quickly proving to be a suitable interconnect technology for meeting the future goals of on-chip bandwidth and low power requirements. However, it is not clear how silicon photonics will be integrated into CMOS chips, particularly microprocessors. The issue of integrating photonic circuits into electronic IC fabrication processes to achieve maximum flexibility and minimum complexity and cost is an important one. In order to minimize usage of chip real estate, it will be advantageous to integrate in three-dimensions. Hydrogenated amorphous silicon (a-Si:H) is emerging as a promising material for the 3-D integration of silicon photonics for on-chip optical interconnects. In addition, a-Si:H film can be deposited using CMOS compatible low temperature plasma-enhanced chemical vapor deposition (PECVD) process at any point in the fabrication process allowing maximum flexibility and minimal complexity. In this thesis, we demonstrate a-Si:H as a high performance alternate platform to crystalline silicon, enabling backend integration of optical interconnects in a hybrid photonic-electronic network-on-chip architecture. High quality passive devices are fabricated on a low-loss a-Si:H platform enabling wavelength division multiplexing schemes. We demonstrate a broadband all-optical modulation scheme based on free-carrier absorption effect, which can enable compact electro-optic modulators in a-Si:H. Furthermore, we comprehensively characterize the optical nonlinearities in a-Si:H and observe that a-Si:H exhibits enhanced nonlinearities as compared to crystalline silicon. Based on the enhanced nonlinearities, we demonstrate low-power four-wave mixing in a-Si:H waveguides enabling high speed all-optical devices in an a-Si:H platform. Finally, we demonstrate a novel data encoding scheme using thermal and all-optical tuning of silicon waveguides, increasing the spectral efficiency in an interconnect link.

Abstract Approval: Committee Chair _____

Program Director _____

Dean KGCOE _____

To my mother and father

ACKNOWLEDGEMENTS

First and foremost, I would like to thank my advisor Professor Stefan Preble for providing me with this wonderful opportunity to conduct research and for his constant support, guidance and encouragement through the duration of this dissertation. Working with him, I have had access to the best research facilities, equipment and resources. His warm, enthusiastic demeanor along with infinite patience has made it an immense pleasure to conduct my research with him.

I would like to acknowledge my dissertation committee members, Professor Seth Hubbard, Professor Sean Rommel, Professor Zhaolin Lu and Professor Bruce Smith for taking their time to assess my progress through the dissertation process. I also thank Sharon Stevens for keeping a watchful eye over my administrative responsibilities.

I would like to acknowledge the staff at Cornell Nanoscale Science and Technology Facility (CNF), especially Alan Bleier for his help with the electron-beam lithography system and Phil Infante for his invaluable suggestions in using the PECVD tool. I would also like to thank Sean O'Brien and John Nash at Semiconductor and Microsystems Fabrication Laboratory (SMFL) for training and helping me during multiple fabrication process steps.

To the RIT Nanophotonics Group members: Ali Elshaari, Abdelsalam Aboketaf, Liang Cao, I would like to express my gratitude for fostering a cordial, friendly and vibrant atmosphere in the group and for always being ready to help with fabrication and characterization processes. I would like to thank Gregory Madejski for proofreading and suggesting revisions to the manuscript. I would like to give a shout out to the undergraduate researchers in the group: Robert (Bobby) Brown and Steven McDermott for being a good sport with all the fun and tricks played out in the lab.

To Stacy Kowsz (PEW PEW), I cherish the companionship during the innumerable driving trips to Ithaca. The joint efforts during operation sand tunnels has made summer of 2010 a summer to remember and cultivated an enduring friendship.

I also would like to thank Sankha Mukherjee, BinduMadhav Sabnavis and Supraja Murali who enhanced my experiences in Rochester with their friendship.

I extend my heartfelt gratitude to my roommate for four wonderful years, Archana Devasia. From accompanying me to multiple emergency room visits, to sharing a common interest in the adventures of Harry Potter and Lisbeth Salander and a liking for Chilean Carménère , I thank you for being there.

Finally, to my parents, I dedicate this thesis to you. I would not be here without your support and sacrifices. I thank you for guiding me, instilling in me the value of education, believing in my abilities and being patient with me for all these years. I express my most sincere appreciation for all that you have done for me.

TABLE OF CONTENTS

LIST OF TABLES

LIST OF FIGURES

CHAPTER 1

INTRODUCTION

1.1 Electrical Interconnects vs. Optical Interconnects

Silicon Photonics can be broadly defined as the use of silicon based materials to generate, control, transfer, and detect light over a distance to enable communications in chip multiprocessors (CMPs) [1]. The motivation for silicon photonics as a medium for optical interconnects (OI) is driven by the power and delay limitations predicted in copper based electrical interconnects (EI). As device sizes have shrunk with Moore's Law as a general rule, ultra-short distance communications on chips have mostly been dominated by electrical interconnects due to the relative ease in their design and fabrication, as well as tolerable power and delay requirements at remarkably low cost. The older 1.0 μm Al/SiO_2 technology generation had transistor delays on the order of 20 ps and RC delays of 1 ps/mm. With scaling to finer technology nodes due to innovations in lithography, the 35 nm Cu/low-κ transistors are expected to have transistor delays of 1 ps [2].

However, as processor speeds increase, it is becoming more difficult to keep a balance between logic operations (i.e. floating point operations or FLOPS) on the chips and the read/write operations of bytes of information into and out of memory. A good rule of thumb is to keep a ratio of 1 byte/FLOP [3]. However, modern systems cannot achieve anything close to this ratio. Current predictions for electrical interconnects indicate this ratio is going to get progressively smaller due to limitations on wiring.

The RC delays in electrical interconnect based devices are predicted to be 250 ps/mm [2]. The EI delay can be reduced by increasing the interconnect width at the

expense of smaller bandwidth density. However, it is predicted that minimum achievable delay shall reach a limit at 20 ps/mm despite a scaling towards finer technology nodes seen here in Figure 1 [4].

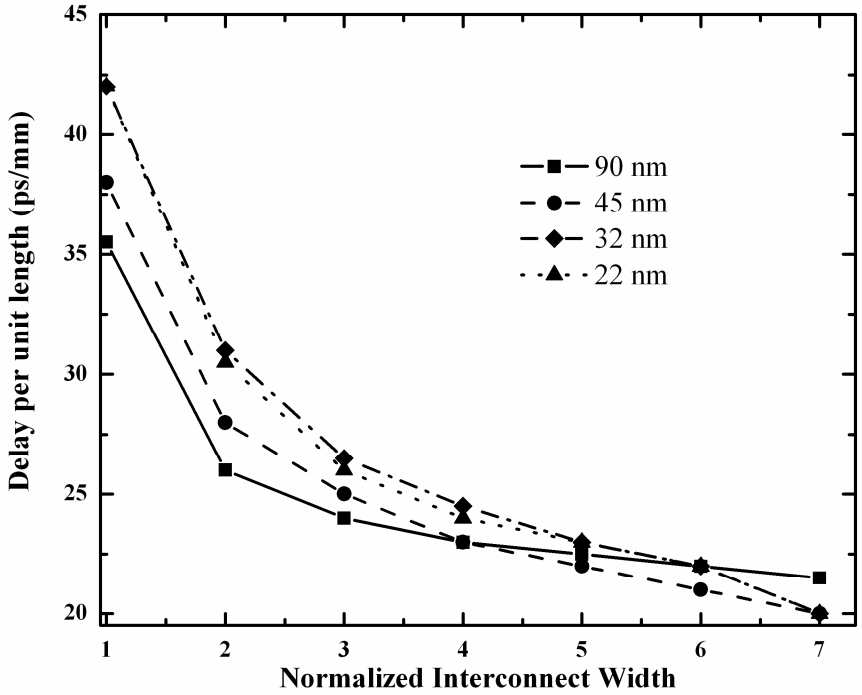

Figure 1.1 Propagation delay in Electrical Interconnects as a function of normalized interconnect width for different technology nodes **[4]**.

Optical interconnects (OI) are proposed as an alternate solution for on-chip communications. This is due to their speed of light propagation and large bandwidth due to the high frequency of optical signals, of the order of 200 – 1000 THz for the corresponding free-space wavelengths of ~ 1.5 μm to 300 nm. The short wavelength of light enables the use of dielectric waveguides to guide these waves with very low transmission losses. The minimal interaction between photons leads to minimal cross-talk between signals being transmitted. Thus optical interconnects have a significant advantage over the undesirable cross-talk generated in metal-dielectric interconnects. Due to speed of light propagation, OIs provide a significant advantage in terms of propagation

delay over electrical interconnects. Electrical signals, however, have to be converted to optical signals to utilize the propagation speeds offered in OIs and have to be converted back into electrical signals for further processing. This conversion requires a fixed amount of delay which is independent of the interconnect distance [4]. It has also been shown that on-chip optical interconnects can achieve lower power and latency than their electronic counterparts when the interconnect length is greater than 1000 times the wavelength [5]. Therefore, optical interconnects tend to have an advantage over electronic interconnects over long communication distances as seen in Figure 2, where a comparison between cu/low-κ electrical interconnect and a silicon waveguide optical interconnect is shown [4]. In keeping with these trends, the International Technology Roadmap for Semiconductors (2007, Interconnects) envisions the integration of optical interconnects for long communications in upper metal layers of CMOS fabrication process.

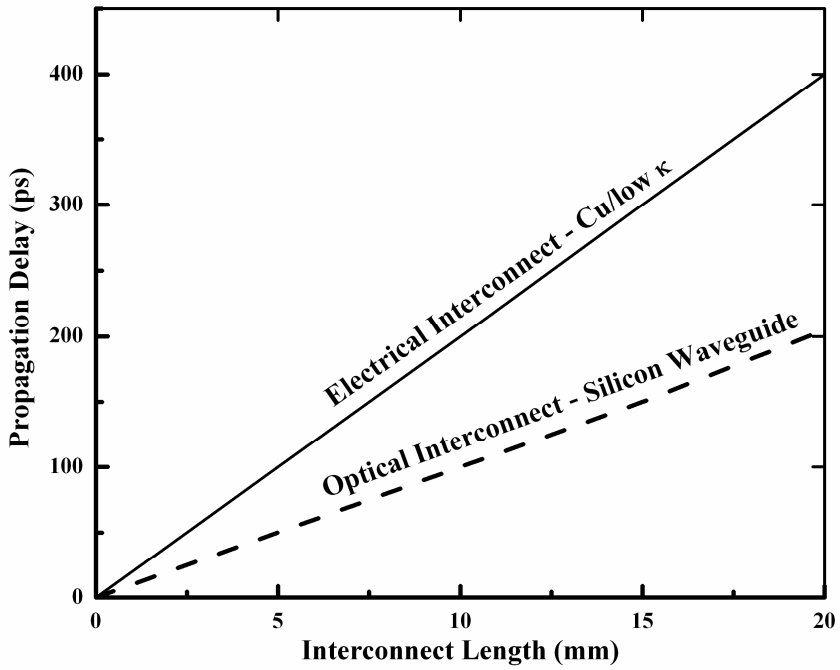

Figure 1.2 Propagation delays in cu-based electrical interconnects and silicon based optical interconnects **[4]**.

1.2. Hybrid Photonic-Electronic Networks-on-Chip Architecture

Networks-on-chip (NoCs) have been proposed to replace the traditional electrical busses [6,7]. Although electronic NoCs have demonstrated some improvements in bandwidth and latency, power consumption remains a critical issue because of high switching activity in electrical interconnects [8,9]. The application of photonics to NoCs is projected to be a more attractive method in simultaneously achieving low power consumption, low latency, and high bandwidth [10]. Recently, a global on-chip optical bus has been applied to remote memory access paths in a multi-core processor [11]. The bus successfully obtained 50% latency reduction over some applications and about 30% power reduction over a baseline electrical bus. A hybrid photonic NoC integrating a photonic circuit-switched network for message transmission and electronic packet-switching for routing path set-up has been presented as well [12]. Based on the strengths of these works, a multicore chip architecture utilizing a hybrid electronic-photonic network is proposed to achieve low power, low latency, high bandwidth and reliable interconnection between cores. Figure 1.3 shows the CMP cores arranged in a grid pattern and connected to their neighbors by electronic and photonic interconnections.

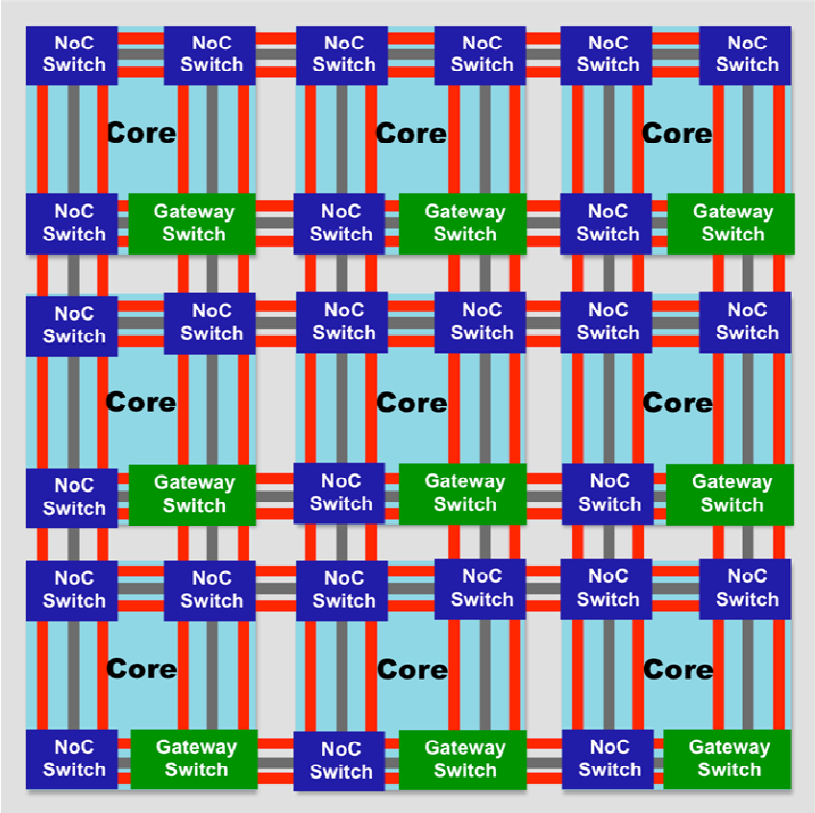

Figure 1.3 Hybrid NoC architecture. The cores are connected to the hybrid photonic-electronic NoC by gateway switches that inject and eject photonic and electronic packets into the network.

To illustrate the operation of a hybrid NoC, the path taken by a typical message between two cores on the chip is described. After the core determines the amount of data to be transmitted to another core over the photonic NoC, an electronic path setup packet containing the source and destination address, photonic message length, error information and priority information is broadcast over the electronic network. To enable the data to be routed across the network, photonic routers are reconfigured while the packet propagates through the network. If a path cannot be established, a message is sent back to the source indicating a bottleneck in the network. If no contentions occur during the path setup, the destination sends an acknowledgement over the photonic network. The photonic path being bi-directional automatically propagates the acknowledgement back to the source. Once the acknowledgement is received, the data is transmitted over the photonic network.

1.3. Silicon-based Photonic Interconnects

In a hybrid network-on-chip (NoC) architecture, the issue of where to integrate photonic circuits into electronic IC fabrication processes to achieve maximum flexibility and minimize complexity and cost is an important one. The backend integration of photonic components in the upper metal layers of CMOS fabrication process is an envisioned solution. The compatibility of silicon photonics with complementary metal-oxide semiconductor (CMOS) processes used in the development of electronic processors has also contributed to its rapid emergence as a cost-effective solution to integrate photonic and electronic circuits on a single platform. Recent advances have enabled the demonstration of integrated modulators and detectors that form the core of an optical interconnect network [13-17]. These devices have primarily been fabricated on single layer crystalline silicon-on-insulator substrate.

However, with increasing device density on a single layer, the design of future generations of interconnect networks will be a challenge. Vertical stacking of silicon layers to form a 3-D hybrid photonic-electronic network-on-chip (NOC) is a proposed solution to overcome the constraints posed by the device density [10,18]. Photonic devices on three vertically stacked layers of crystalline silicon have been demonstrated [19]. The process is fabrication intensive involving multiple implantation and epitaxial growth processes, and is not likely to be cost effective. More recently, polycrystalline silicon [20-22] and amorphous silicon [23-26] have been proposed as alternate solutions for large scale 3D integration of optical interconnect networks.

Although it is a viable solution, polysilicon has higher optical losses due to scattering at imperfections and grain boundaries. Backend integration of photonic devices also limit

the thermal budget of the interconnect architecture. To achieve device quality substrates, polysilicon films need to be annealed at elevated temperatures (>600 C), thereby increasing the thermal budget. An alternate solution is to anneal amorphous silicon films with short pulse lasers to form local polycrystalline regions [27]. This process, however, can add to the complexity of fabrication of the electro-optic NoC architecture. Integrated optical devices fabricated in deposited silicon crystallized at room temperature have been measured to have extremely high optical losses [28].

Amorphous silicon is characterized by the absence of long range order in its atomic structure. This causes the material to have a large density of point defects and dangling bonds, collectively called coordination defects, caused when an atom has too many or too few bonds [29]. Addition of hydrogen to amorphous silicon reduces the defect density by saturating the dangling bonds resulting in a low loss platform for nanophotonics. Hydrogenated amorphous silicon (a-Si:H) can be deposited using low temperature (~250-400 ºC) plasma-enhanced chemical vapor deposition (PECVD) which is automatically compatible with the backend thermal budget in the CMOS fabrication process. Therefore, amorphous silicon can be integrated at any point in the fabrication process with minimal complexity. This makes hydrogenated amorphous silicon (a-Si:H) a material of choice in the backend integration of a hybrid NoC.

A proposed hybrid photonic-electronic multicore chip using a-Si:H is shown in Figure 4. The transistors reside on the bottom layer and will further be connected to the photonic circuits through the metallization stack. The photonic circuit primarily consists of 0.46 μm by 0.25 μm cross section amorphous silicon ‘wires’. The photonic wires are similar in function to metal wires in that they can have arbitrary lengths and make sharp

bends. However, they are fundamentally different since they do not require any power to propagate the signal. Once the light is coupled in these wires, it will freely propagate at the speed of light and can intersect with other wires with minimal interference between signals. Also seen in this cross-section are lasers and SiGe photodetectors whose implementation on chip has been proposed by others [30].

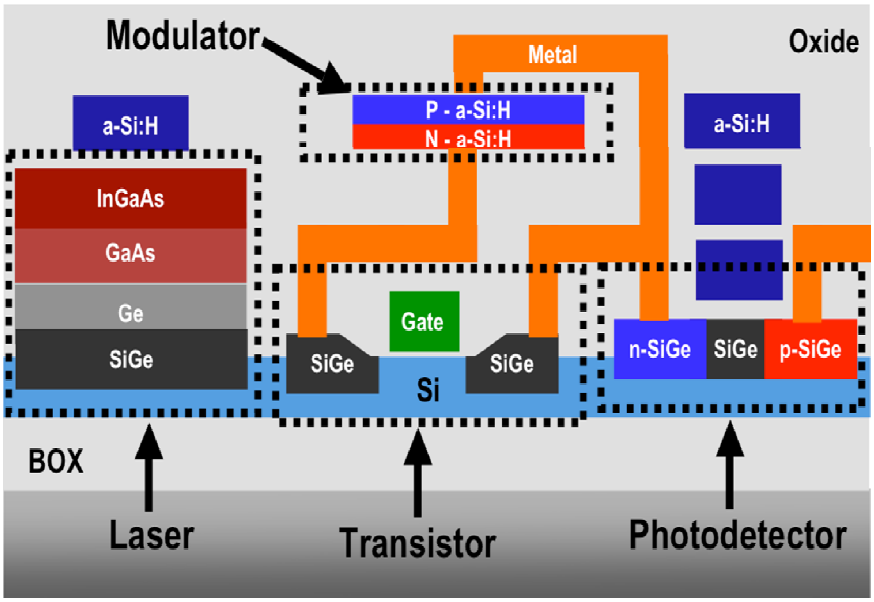

Figure 1.4 Cross section of a proposed hybrid photonic-electronic chip. The structure is based on SOI with embedded SiGe regions for transistor strain, growing laser materials, and for photodetectors. Hydrogenated amorphous silicon wires (a-Si:H) are integrated in the metal stack and used to transfer light throughout the chip. Multiple a-Si layers are used for transferring light from layer-to-layer.

The proposed research in this thesis will characterize hydrogenated amorphous silicon (a-Si:H) waveguides for its feasibility as photonic platform in its integration in a hybrid photonic-electronic network-on-chip (NoC) architecture.

CHAPTER 2

HYDROGENATED AMORPHOUS SILICON

2.1 Atomic Structure in Amorphous silicon (a-Si)

Silicon is currently the most attractive material of choice for electronic devices because of its abundance and unique semiconducting properties. It is used to make transistors and integrated circuits used in the computer industry, flat-panel displays, and solar-cell applications. Silicon exists in monocrystalline, polycrystalline, and amorphous forms. Monocrystalline or single-crystal Si consists of an unbroken, continuous crystal lattice structure with no grain boundaries. Polycrystalline silicon consists of multiple small silicon crystals that are connected together by grain boundaries. Amorphous silicon on the other hand is the non-crystalline form of silicon. In amorphous silicon, there is an absence of any long range order, and an emphasis is placed on short-range coordination bonds [29].

The disorder of the atomic structure is the main feature that distinguishes amorphous silicon from its crystalline counterpart. The short range order and long range disorder lead to a model of continuous random network as shown in Figure 2.1. The periodic crystalline structure is replaced by a random network where each atom has a specific number of bonds to its immediate neighbor called coordination bonds. This random network can easily incorporate atoms of different coordination even in small concentrations. This contrasts with the crystalline nature of silicon where impurities are constrained to have the coordination of the host because of long range ordering of the lattice. The short range ordering in amorphous silicon manifests as the elementary defect when an atom has too many or too few bonds as seen in Figure 2.2 (b).

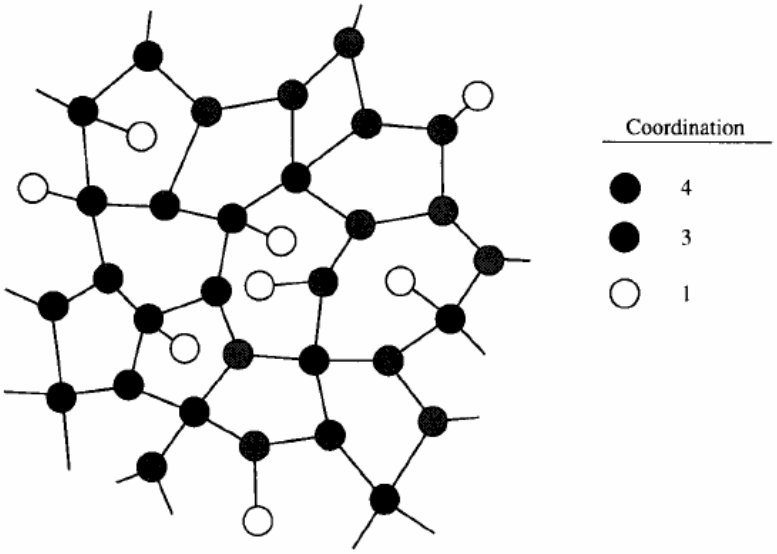

Figure 2.1 Continuous random network containing atoms of different bonding coordination **[29]**.

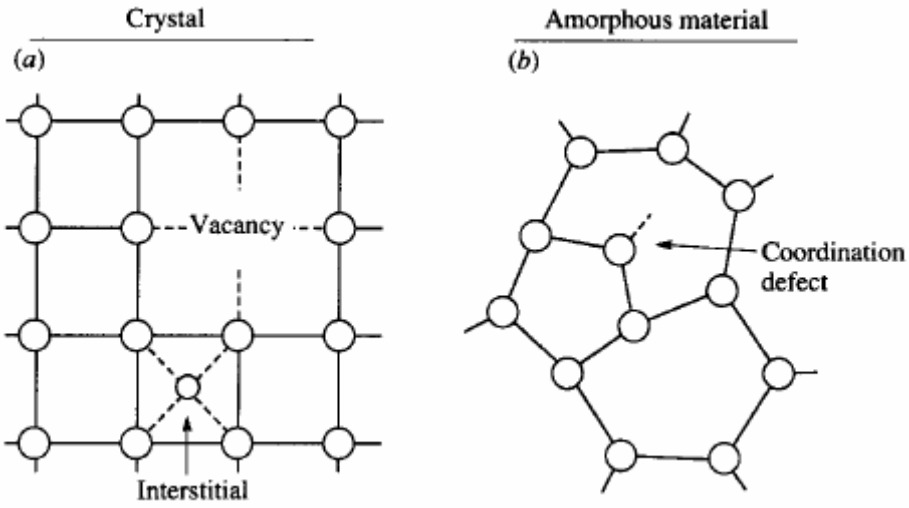

Figure 2.2 Illustration showing the different types of defects in (a) crystalline and (b) amorphous silicon **[29]**.

In crystalline silicon, any atom that is out of place in the crystal is a defect. The simplest defects in c-Si are vacancies and interstitials as seen in Figure 2.2 (a). The ability of the disordered network on a-Si to adapt to any atomic coordination allows for an isolated defect, which is not possible in c-Si.

2.2 Electronic Structure in Amorphous silicon (a-Si)

The fundamental property of a semiconductor is its band gap structure that separates the occupied valence band from the empty conduction band. The band gap is a consequence of the periodicity of the crystalline lattice as defined by the free electron theory. The bands are influenced strongly by the short range order in both crystalline and amorphous silicon and the absence of periodicity in a-Si acts as a small perturbation.

The principal features of a-Si are defined by its short range order, long range disorder and the coordination defects. Short range order results in similar electronic structure in the case of crystalline and amorphous silicon. However, the abrupt edges in crystalline silicon are replaced by a broadened tail of states in amorphous silicon that extend into the forbidden gap that originates from bong length and angle deviations arising from long range disorder as seen in Figure 2.3 [29].

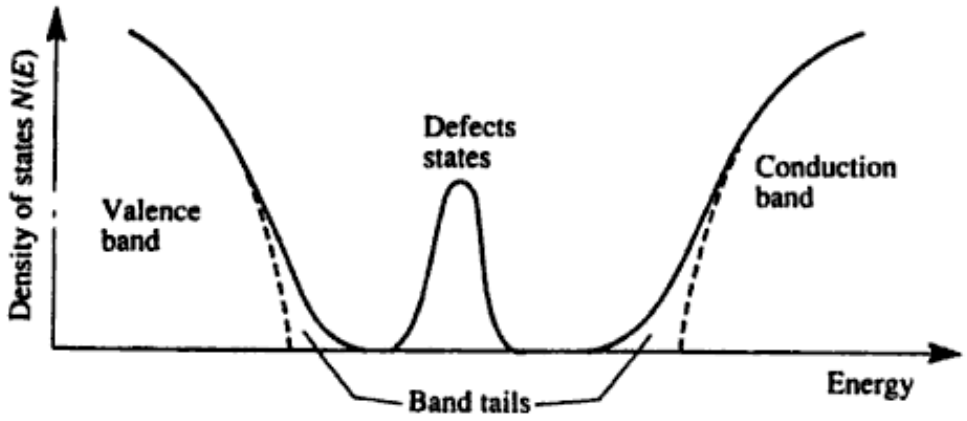

Figure 2.3 Schematic showing the density of states distribution for amorphous silicon with band, band tails and defect states in the band gap. The dashed curves represent the equivalent density of states in a crystal **[29]**.

The band tails play an important role because the electronic transport occurs at the band edge. The electronic states occur deep within the band gap arise due to departures

from the ideal network. These defect states determine many electronic properties by controlling the trapping and recombination of carriers. The broadened tail states that result due to deviations cause carrier localization which in turn strongly scatters the carriers. The strong scattering of the carriers results in lower carrier mobilities in amorphous silicon (< 10 $cm^2/V \cdot s$) and causes the profound effect of localizing the wave function. The disorder in the structure in amorphous silicon also manifests in the loss of momentum (*k*) conservation in electronic transitions. There is a greater emphasis on the spatial location of the carrier than on its momentum. It also results in the loss of distinction between a direct and indirect band gap in amorphous silicon. Instead the transitions occur between states which overlap in space. Therefore in pure a-Si, many silicon atoms are three-fold coordinated which leaves one dangling bond. The dangling bonds are considered to be the most major defect from the localized states in the middle of the band gap [29]. The density of these defects in pure a-Si (> 10^{19} cm^{-3}) makes them a high loss platform for optical waveguides. The first a-Si waveguides patterned using Xe ion irradiation and reactive ion sputtering had measured losses of ~500 dB/cm and ~30 dB/cm respectively [24].

However, addition of hydrogen to amorphous silicon reduces the defect density and results in a low loss platform for photonic devices.

2.3 Hydrogenated Amorphous Silicon (a-Si:H)

The incorporation of hydrogen during growth of amorphous silicon results in the passivation of the dangling bonds and reduces the density of midgap states to ~ 10^{15} – 10^{16} cm^{-3}. The resulting film is called hydrogenated amorphous silicon (a-Si:H). Most

features of the a-Si:H depend on the details of the deposition process and therefore the properties of the film vary with the growth conditions.

The usual method of deposition a-Si:H is by plasma decomposition of silane gas, SiH_4, in the presence of an inert gas. Silane can decompose in the absence of plasma at temperatures above 450 ºC, but the films deposited tend to be mostly of low quality because the temperature is too high to retain hydrogen. The decomposition of hydrogenated amorphous silicon films at lower temperatures requires a source of energy to dissociate the silane molecule which is performed by the plasma.

The first plasma deposition system for amorphous silicon was developed by Chittick et al and was a radio frequency (rf) inductive system in which an induction coil outside the quartz deposition chamber created the plasma. Most subsequent designs have incorporated a diode configuration in which the plasma is contained between two parallel plate electrodes. Deposition takes place at a pressure of 0.1-3 Torr, which is the optimum pressure to sustain the plasma. The reactor consists of a gas inlet, the deposition chamber to hold the substrate, pumping system and source power for the discharge. The deposition process is referred to as plasma enhanced chemical vapor deposition (PECVD).

The deposition parameters must be varied to obtain a device quality film. The variation in the gas pressure determines the mean free path for collisions of the gas molecules and influences whether the reaction occurs in the gas or at the growing surface. The gas flow rate determines the residence time of the gas species in the reactor. The variation in the rf power controls the rate of gas dissociation and thereby the deposition rate of the film. The chemical reactions on the surface are determined by the temperature of the substrate.

The hydrogen content during the deposition process ranges from 8 to 40 % and decreases as the substrate temperature rises. The defect density also depends on the substrate temperature and rf power and varies by more than a factor of 1000. The lowest values are obtained at a temperature between 250 – 400º C and are the conditions for films with useful optical and electronic properties.

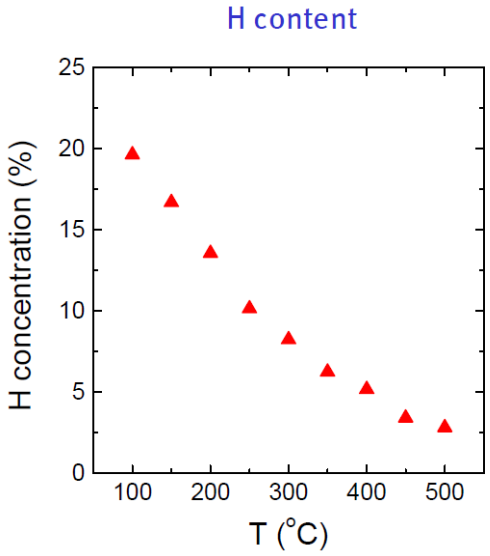

Figure 2.4 Variation in the hydrogen content in amorphous silicon with substrate temperature **[29]**.

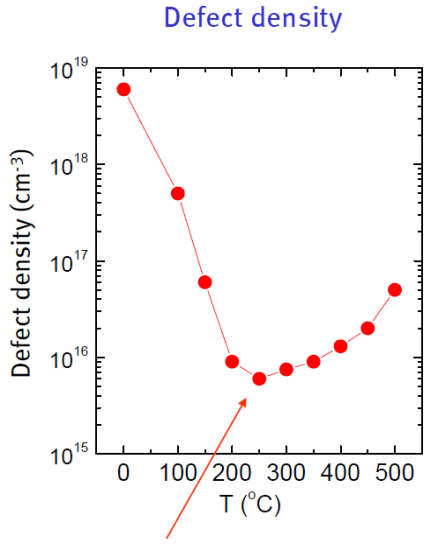

Figure 2.5 Variation in the defect density states with substrate temperature showing an optimum defect density in the 200-300 ºC range **[29]**.

Thus, addition of hydrogen during deposition process reduces the defect density states in amorphous silicon resulting in a low loss platform for photonic devices.

CHAPTER 3

BACKGROUND AND RESEARCH OBJECTIVES

3.1 Hydrogenated-amorphous silicon (a-Si:H) based planar waveguides

Interest in hydrogenated-amorphous silicon as a material for the realization of optical interconnects in integrated circuits was initially proposed with the demonstration of a thermo-optically tunable a-si:H planar waveguide based Fabry-Perot intensity modulator with > 0.7 dB/cm transmission losses [31]. The hydrogenated amorphous silicon films were deposited using plasma-enhanced chemical vapor deposition technique (PECVD). Since then, there have been numerous demonstrations of passive, low loss, planar waveguides in a-Si:H with emphasis on developing a low cost, CMOS compatible process for integrating a-Si:H planar waveguides in photonic integrated circuits. Initially, MeV level Xe ion irradiation of silicon-on-insulator (SOI), followed by annealing of the substrate in hydrogen ambient was used to define a-Si:H waveguides [32]. However, this process is fabrication intensive, and waveguides that were demonstrated had relatively high transmission losses. Plasma-enhanced chemical vapor deposition (PECVD) has since become the de facto standard process for depositing a-Si:H, since nearly all dangling bonds are passivated with hydrogen. One of the first demonstrations of low loss a-Si:H waveguides at 1550 nm was achieved with the deposition parameters [33]:

Table 3.1. PECVD deposition parameters for a-Si:H [33]

SiH_4 flow	70 sccm
Ar flow	210 sccm
Substrate temperature	300 ºC
Pressure	500 mTorr
RF power	250 W
Frequency	380 kHz
Deposition rate	96 nm/min

The transmission loss in a-Si:H waveguides patterned using the deposition parameters in Table 3.1 was measured to be < 0.5 dB/cm for multimode waveguides, and < 2 dB/cm for single mode waveguides at 1550 nm. There have been several other demonstrations of low-loss planar a-Si:H waveguides based on PECVD [34-36]. More recently, low loss (~ 2.5 dB/cm) channel a-Si:H waveguides were demonstrated using a damascene process. A 1 μm thick SiO_2 was thermally grown on a silicon substrate and 600 nm wide and 100 nm deep trenches were defined using standard photolithography, followed by a RIE etch using CHF_3 and CF_4 chemistry. A 300 nm hydrogenated amorphous silicon (a-Si:H) film was then deposited using PECVD to uniformly fill in the trenches. The excess a-Si:H was polished away using a standard chemical-mechanical polishing process (CMP) as shown in Figure 3.1.

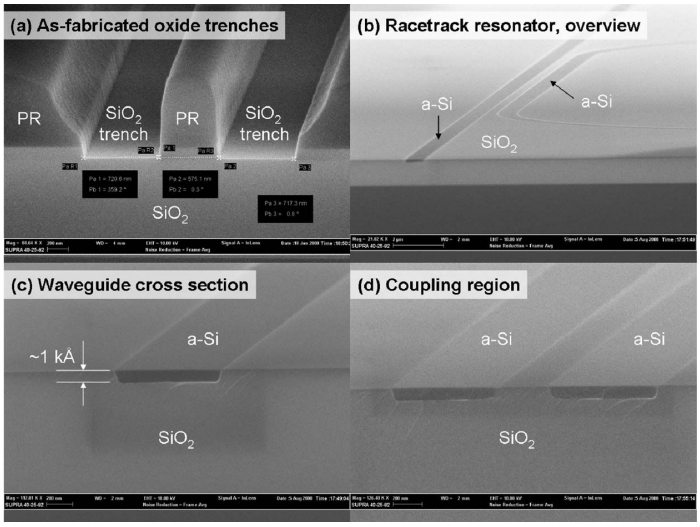

Figure 3.1 Angled cross-sectional SEM images of (a) as-etched oxide trenches before photoresist (PR) is removed; (b) overview of a racetrack resonator after CMP; (c) a-Si channel waveguide formed in the oxide trench after CMP; (d) coupling region of the racetrack resonator after CMP **[35]**.

Planar waveguides along with racetrack resonators in a-SI:H were fabricated using the damascene process. Since the undercladding layer was only 1 µm thick, only TE polarized modes could be excited in the waveguides as the TM modes were lost to substrate coupling. The racetrack resonators exhibited quality factors (Q) in the range of mid 10^4 – 10^5 as shown in Figure 3.2.

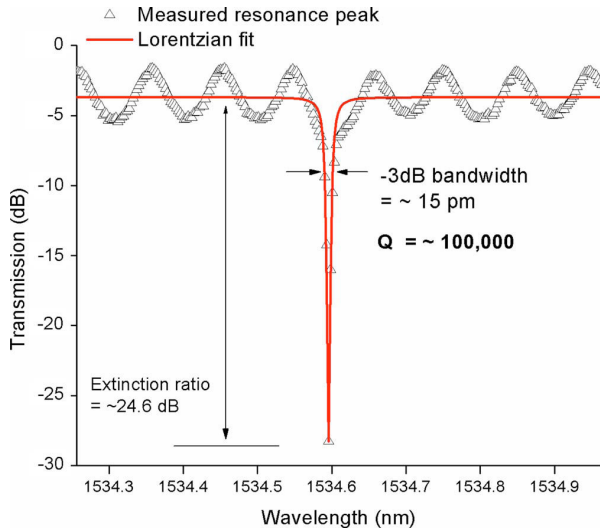

Figure 3.2 The measured quality factors in the a-Si:H racetrack resonators fabricated using the damascene process **[35]**

3.2 Modulation Schemes in a-Si:H waveguides

Thermo-optic and all-optical modulation schemes have also been exploited in a-Si:H to demonstrate modulation of optical signals in planar waveguides. The thermo-optic coefficient has been determined to be $2.3 \cdot 10^{-4}$ K^{-1} which is 20% higher than in crystalline silicon [37]. Hydrogenated amorphous silicon film was stacked between two layers of hydrogenated amorphous silicon carbide films to form a planar waveguide as shown in Figure 3.3 and glued to a Peltier heat pump. The transmitted light intensity was monitored in the temperature range between 30 ºC – 40 ºC [37].

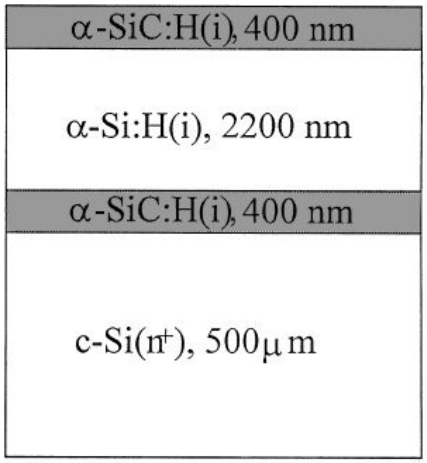

Figure 3.3 A planar a-Si:H waveguide with a-SiC:H films forming the top and bottom cladding layers **[37]**

The recorded transmitted intensity (I_t) plotted against the change in temperature is shown in Figure 3.4. The periodic amplitude modulation is because of setting up instigating interference patterns in the waveguide that acts a Fabry-Perot resonant cavity. The change in refractive index due to the change in temperature results in the tuning and detuning of the interference filter at $\lambda = 1.3$ μm.

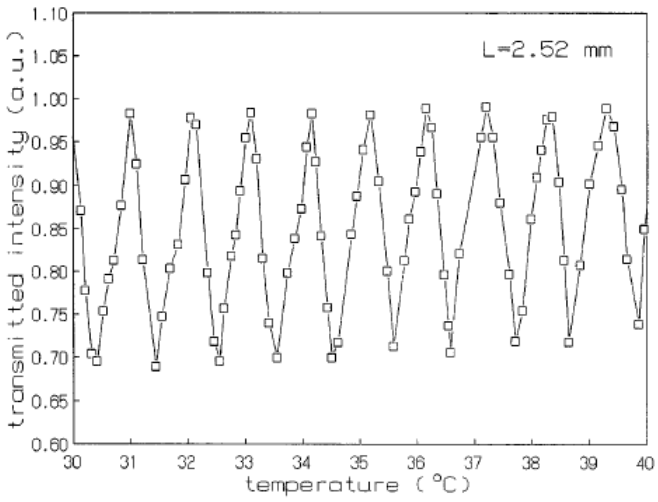

Figure 3.4 Thermo-optic modulation of light in a planar a-Si:H waveguide **[37].**

All-optical modulation of light in a-Si:H planar waveguides has also been demonstrated [38]. A boron doped a-Si:H film was deposited on top on a silicon substrate with ZnO serving as the cladding region. The waveguides were 4 mm wide and 1.75 μm thick. The pump-probe setup is shown in Figure 3.5 (a).

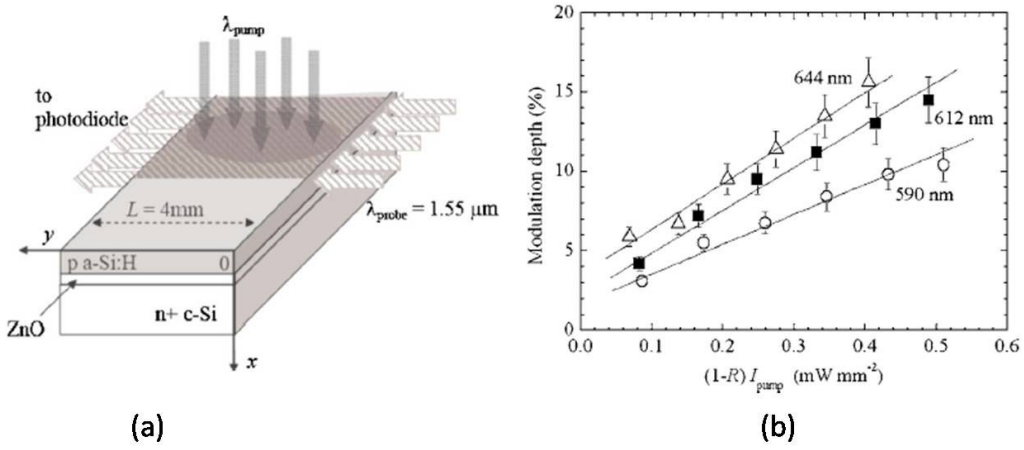

Figure 3.5 (a) The configuration between pump and the probe is schematized. (b) Modulation depth M measurements on the a-Si:H waveguide vs. the pump illumination intensity at each pump wavelength **[38].**

The probe beam at λ = 1.55 μm was incident orthogonally to the waveguide and was modulated using pump beam from AlInGaP light emitting diodes (LEDs) at different wavelengths and the modulation depth was measured as shown in Figure 3.5 (b). The

change in the modulation depth (M) of the probe signal indicates a photoinduced infrared absorption modulation of the probe signal.

More recently, all-optical modulation in amorphous silicon filled microstructured fibers was demonstrated as shown in Figure 3.6 [39]. The fiber pores, 6 μm in diameter, were filled with a-Si:H by heating the fibers to 480-496 ºC and flowing a precursor of SiH_4 and He gases. The propagation losses in the fibers were estimated to be 24.8 dB/cm and 17 dB/cm. The probe signal at λ=1.55 μm was illuminated with a pump pulse at 532 nm, (17.5 ns width, 10 Hz repetition rate) and the temporal response measured as shown below.

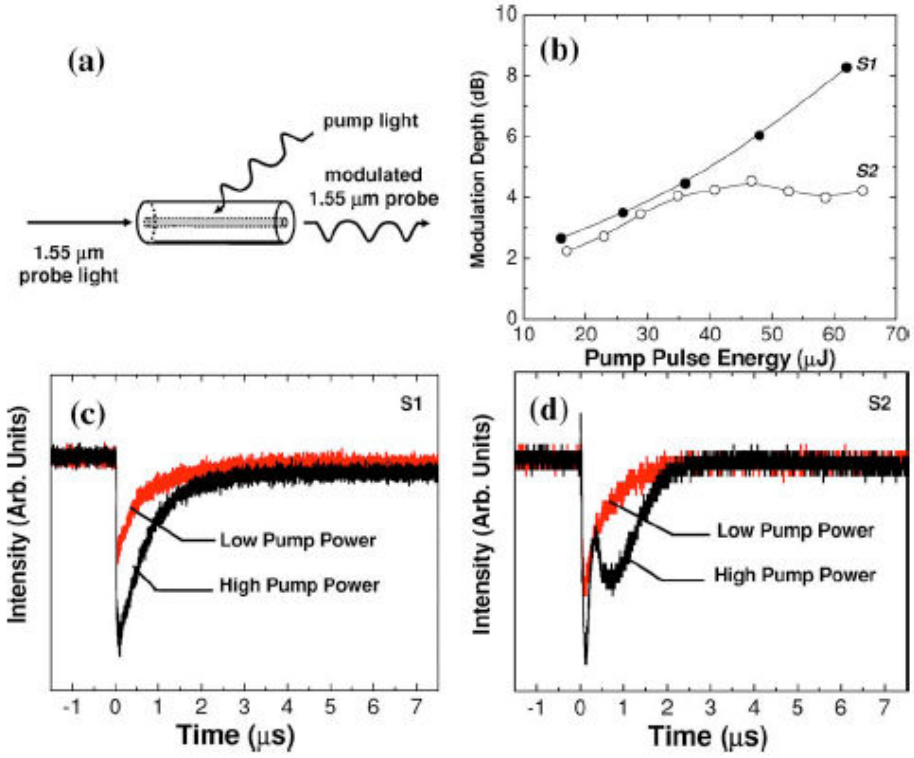

Figure 3.6 (a) Schematic diagram of the all-optical modulation setup in a-Si:H filled microstructured fibers. (b) Measured modulation depth vs. pump pulse energy in two different fibers. Time resolved transmission of the probe signal under illumination from a 532 nm probe signal at two different energies (16 μJ & 62 μJ) for two different fibers **[39]**

Based on the measured temporal response, the effective carrier lifetime in the amorphous-silicon filled microstructured fibers was measured to be 690 ns.

Electro-optic effects in a-Si:H have not been demonstrated much because of the weak quadratic electro optic effect and the difficulty in achieving a significant carrier injection across p-n junctions, due to the low mobility values of the carriers in hydrogenated amorphous silicon [40**,** 41].

A modest absorption modulation scheme has been demonstrated, based on depositing a multilayer alternating stack of hydrogenated amorphous silicon (a-Si:H) and amorphous silicon carbonitride (a-SiC_xN_y) on a heavily p-doped silicon substrate as shown in Figure 3.7 below [42].

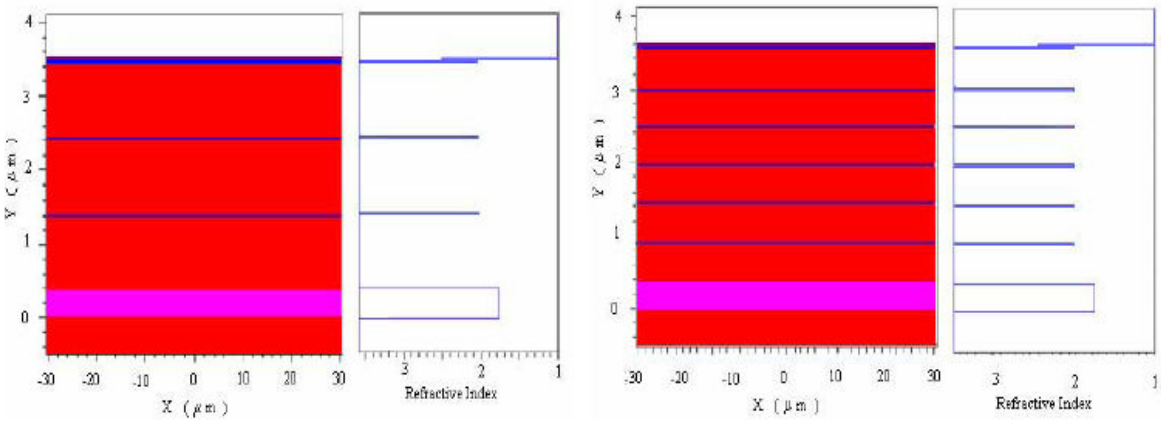

Figure 3.7 Schematic cross sections of realized planar waveguides and corresponding refractive index profiles. The crystalline silicon substrate is 300 μm thick [**42**].

The deposited a-Si:H layers were 1 μm thick and the a-SiCN layers were 30 nm in thickness. A strong vertical confinement of the optical mode is achieved due to the high index difference between the two films, $\Delta n \sim 2$. A 100 nm thick, transparent indium tin oxide (ITO) forms the top contact and the silicon substrate forms the bottom contact. The presence of a-SiCN layers between a-Si:H creates a capacitive effect and causes a distribution of free-carriers in the cross-section. A maximum modulation depth of 9% is

obtained for the three bi-layers sample (L = 1.2 cm) and a modulation depth of 27% is obtained for the six bi-layers sample (L = 1.5 cm). The effective absorption co-efficient ($\Delta\alpha$) was measured to be 0.11, 0.18 and 0.21 cm^{-1} at 10, 20 and 30 V biases respectively corresponding to an electric field of 0.15, 0.30 and 0.45 MV/cm across the insulating a-SiCN layers. The change in the optical output with respect to applied signal is shown in Figure 3.8 (a) below. The modulation depth with respect to frequency for the six bi-layer structure driven by 20 V pulses is shown in Figure 3.8 (b). The modulation bandwidth is limited by the characteristic carrier recombination times due to carrier trapping and releasing in shallow levels in disordered a-Si:H films. An enhancement of the modulation can be achieved by increasing the number of a-Si:H/a-SiCN layers in the stack and by thinning the stack as both approaches increase the relative volume of the waveguide where carrier accumulation takes place, and should also allow for a reduction in the applied bias voltages. This scheme is the only active electro-optical device demonstrated in a-Si:H.

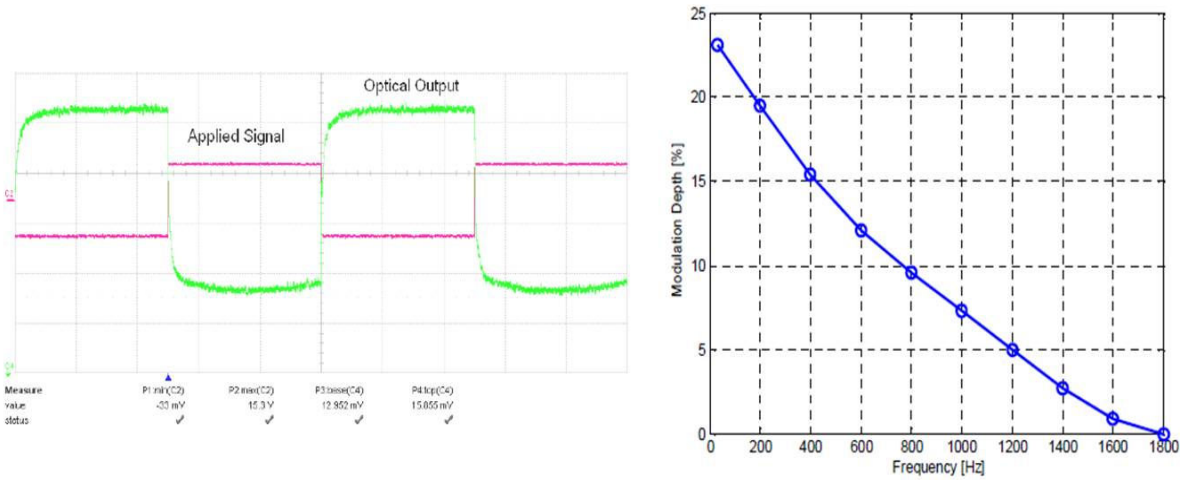

Figure 3.8 (a) Output light power and applied voltage for a six bi-layer 1-cm long waveguide. The modulating signal has V_{min} = 0 V, V_{max} = 15 V, duty cycle = 50 %, frequency = 10 Hz. (b) Modulation depth vs. Frequency [**42**].

3.3 Optical Nonlinearities in a-Si:H Waveguides

Enhanced optical nonlinearities have been measured in amorphous silicon films using a z-scan measurement technique, shown here in Figure 3.9 [43]. A comparison of the nonlinearities was made between crystalline silicon, amorphous silicon, and two hydrogenated amorphous silicon films. The amorphous silicon film was deposited using RF sputtering technique, while the hydrogenated amorphous silicon films were deposited using PECVD.

A qualitative description of the samples used in the experiments in given in Table 2 below. To quantify the nonlinearities, an enhanced nonlinear co-efficient β' was defined by combining the two-photon absorption co-efficient β of crystalline silicon and free-carrier cross section σ.

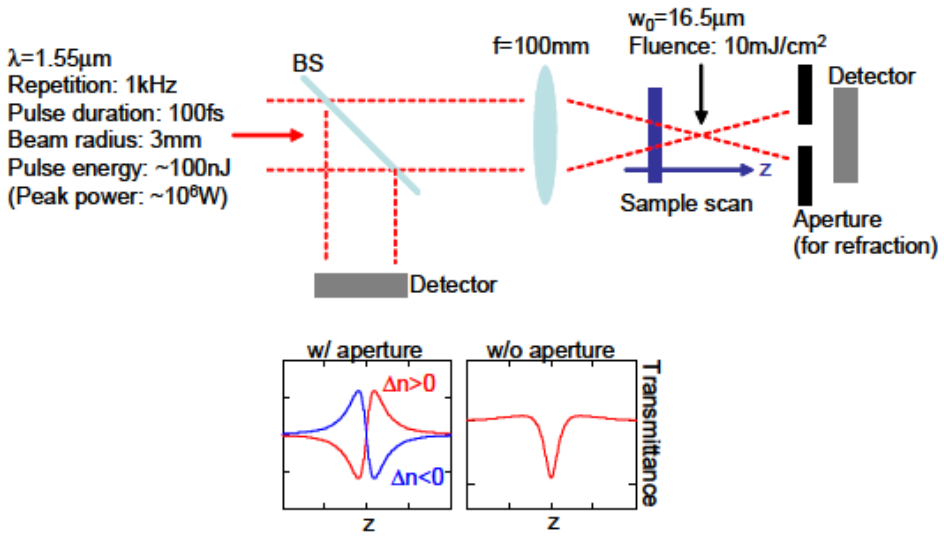

Figure 3.9 Schematic diagram of z-scan measurement set-up [**43**].

Table 3.2. Material properties and parameters for a-Si:H [43]

Material	a-Si □	a-Si:H(1) ○	a-Si:H(2) △	c-Si ×
Refractive index n_0	3.7	3.4	3.4	3.48
Thickness L	4.85μm	2.94μm	3.14μm	220μm
Absorption α at 1.55μm	0.7dB/μm	0.037dB/μm	small	small
Substrate	1mm SiO_2	150μm SiO_2	0.5mm SiO_2	-
Process	RF sputtering	PECVD	PECVD (high quality)	-

$$\beta' = \beta + \sigma \frac{\alpha}{2\hbar\omega} \frac{\sqrt{\pi}}{2\sqrt{\ln 2}} \tau_p$$

The nonlinear coefficients β's were calculated to be 104 cm/GW for a-si, 6.7 cm/GW for a-Si:H (1) and 1.4 cm/GW for a-Si:H(2). The enhanced nonlinear absorption is attributed to a "two-step absorption" (TSA) from mid-gap localized states as shown in Figure 3.10.

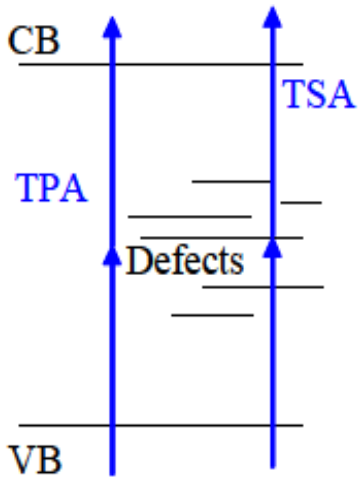

Figure 3.10 Schematic diagram describing two-step absorption (TSA) through mid-gap localized states [**43**].

There has been no measurement of the nonlinear refractive index n_2 in a-Si:H to the best of my knowledge.

In conclusion, this section reveals previous progress made in the field of amorphous silicon photonics (a-Si:H). Low-loss planar waveguides and microresonators have been demonstrated to achieve passive routing of optical signals. However, there is a need for the characterization of the nonlinear properties in a-Si:H, as well as the demonstration of an efficient electro-optic modulator that can enable active devices to route signals in an interconnect network.

3.4 Research Objectives

The primary goal of this thesis is to investigate the feasibility of hydrogenated amorphous silicon (a-Si:H) as an alternate platform to crystalline silicon, enabling backend integration of optical interconnects in a hybrid photonic-electronic network-on-chip architecture. We shall now give an outline of the thesis focusing on results achieved towards reaching the end goal and describe the theory behind the results obtained.

3.5 Thesis Outline

3.5.1 Passive Microcavities

In Chapter **4**, we demonstrate a low-loss hydrogenated-amorphous silicon (a-Si:H) platform, along with high quality factor micro-cavity devices that can enable the realization of on-chip wavelength-division multiplexing schemes. We also demonstrate a **broadband** all-optical modulation scheme in a-Si:H based on free-carrier absorption effect in stark contrast to **band-limited** modulation schemes using cavity resonators based on free-carrier plasma dispersion effect observed in crystalline silicon.

The micro-cavities described in Chapter **4** are sub-micron sized waveguides looped around to form a ring or a donut shaped structure. The optical modes traveling in these cavities build up due to interference from multiple passes around these structures. At

certain wavelengths that satisfy the condition described in Equation 3.1, the modes traveling inside the cavities interfere constructively to build up intensity inside these structures. The wavelength satisfying this condition is called the resonant wavelength.

$$M \cdot \lambda = 2 \cdot \pi \cdot R \cdot n_{eff} \tag{3.1}$$

In Equation 3.1, R is radius of the cavity, n_{eff} is the effective index of the mode traveling in the cavity, λ is the wavelength and M is the mode number. At all other wavelengths, modes interfere destructively such that there is no build-up of intensity in these structures. The transfer function of a micro resonator is shown in Figure 3.11.

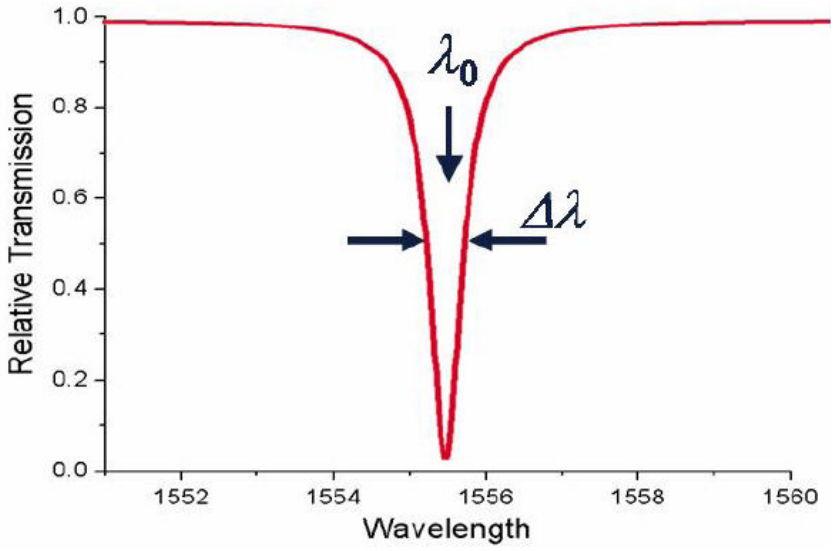

Figure 3.11 Transmission spectrum of a microring resonator. The resonance wavelength is indicated as λ0 and Δλ is full-width half maximum bandwidth of the resonator.

The full-width half maximum bandwidth defines the quality factor (Q) of the resonators. The Q-factor of a resonator is defined in Equation 3.2.

$$Q = \frac{\lambda}{\Delta\lambda} \tag{3.2}$$

The sharpness of the resonance or the quality factor (Q) determines the photon lifetime of the cavity given by Equation 3.3.

$$\tau_p = \frac{Q\lambda}{2 \cdot \pi \cdot c} \tag{3.3}$$

The group index of a ring resonator can be determined experimentally by measuring the free-spectral range (FSR) of the device. The free-spectral range is defined as the spatial distance between two adjacent resonances. The group index (n_g) can be determined from the measured FSR according to Equation 3.4.

$$FSR = \frac{\lambda^2}{n_g \cdot 2 \cdot \pi \cdot R} \tag{3.4}$$

The parameters described here are used to characterize the microresonator devices fabricated in a-Si:H as described in Chapter **4**.

3.5.2 Optical Nonlinearities in Waveguides

In chapter **5**, we comprehensively characterize the optical nonlinearities in a-Si:H waveguides and compare the properties with that of crystalline silicon waveguides. The nonlinearities in a-Si:H are measured to be 5 times that in crystalline silicon waveguides. Based on the enhanced nonlinearities, we also demonstrate low-power continuous wave four-wave mixing in a-Si:H waveguides and measure the nonlinearities based on the observed spectrum.

The need for a higher bandwidth in optical communications necessitates the use of short pulses to transmit a higher data bit rate. Ultra-short pulses result in high intensities, leading to the generation of optical nonlinearities due to the long interaction length in the submicron sized waveguides. Nonlinear optical effects in SOI waveguides, including

nonlinear two photon absorption (TPA), self-phase modulation (SPM), four-wave mixing (FWM) have been previously demonstrated [44-50].

Two-Photon Absorption

Two-photon absorption (TPA) is a nonlinear process where two photons are simultaneously absorbed to generate an electron-hole pair. TPA occurs when the energy of a photon is less than the bandgap energy but greater than one-half the energy bandgap. TPA can be classified into two different types – degenerate TPA and non-degenerate TPA as shown in Figure 3.12.

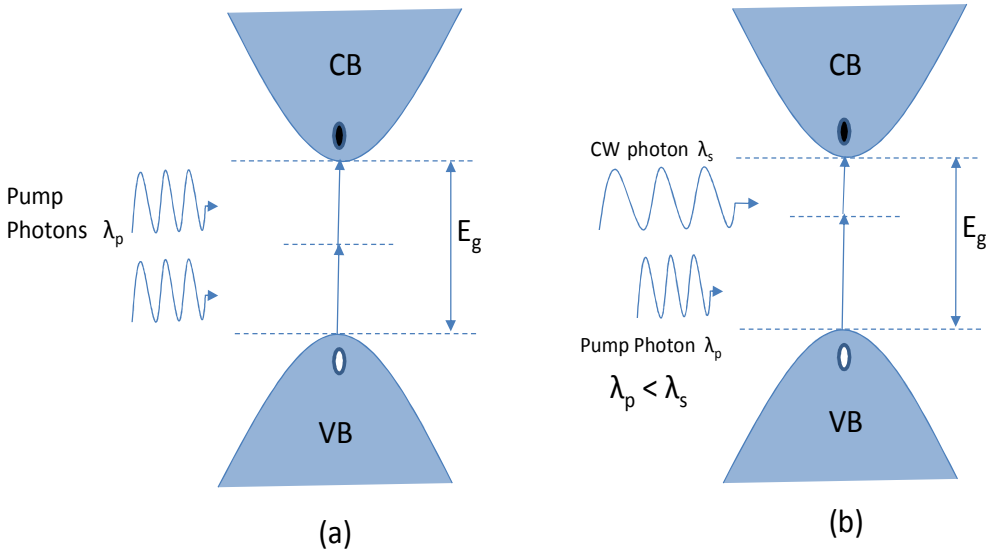

Figure 3.12 Two-photon absorption processes - (a) Degenerate TPA, (b) Non-Degenerate TPA

Degenerate TPA is caused by the absorption of two pump photons having the same frequency, whereas non-degenerate TPA is caused by the absorption of pump and signal photon. In the case of non-degenerate TPA, $\lambda_p < \lambda_s$, so that TPA occurs only if pump photon is present. Unlike other nonlinear processes such as Four-wave mixing (FWM), TPA is independent of phase matching conditions. The carriers generated in process of

TPA cause free carrier absorption (FCA) of the propagating signal, resulting in the depletion of the pump power. Thus, the process of two-photon absorption causes the material to act as an optical limiter. However, devices exploiting the nonlinear properties in silicon require that free carriers generated due to TPA be actively swept out to minimize the loss of photons. The intensity (I) of the field propagating within a material is given by the following relation

$$\frac{dI}{dz} = -(\alpha + \beta_{TPA} I + \sigma N) I \tag{3.5}$$

where α is the linear transmission loss, β_{TPA} is the two-photon absorption coefficient and σ is the free carrier absorption cross-section.

Self-Phase Modulation

Self-phase modulation (SPM) is a nonlinear process where the pump pulse undergoes an alteration in its phase, proportional to its intensity. The phase of the wave is given by the relation

$$\phi(z) = (n_o + n_2 I) k_o z - \omega t \tag{3.6}$$

n_o is the linear refractive index and n_2 is the nonlinear or Kerr coefficient. As the pump pulse propagates through the medium in time, the time derivative of phase leads to a change in the mean frequency of wavelength of the pulse as illustrated in Figure 3.13.

$$\omega(z) = -\frac{\partial \phi}{\partial t} = \omega - n_2 k_o \frac{\partial I}{\partial t} z \tag{3.7}$$

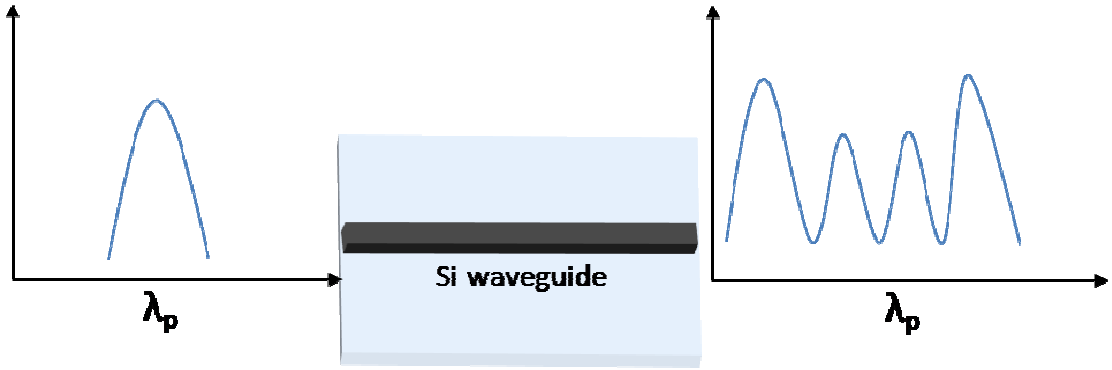

Figure 3.13 Schematic illustration of SPM in a silicon waveguide

The nonlinearities described above are characterized by propagating ultra-short optical pulses through the waveguide and modeling the measured data by solving a set of nonlinear differential equations given by [51-53]

$$\frac{\partial u}{\partial z} + i\frac{\beta_2}{2}\frac{\partial^2 u}{\partial t^2} = \left(i\frac{\omega}{c}n_2 - \frac{\beta_{TPA}}{2}\right)\frac{|u|^2}{A_{eff}}u - \frac{N_c}{2}\left(\sigma - i\frac{\omega}{c}k_c\right)u - \frac{\alpha_l}{2}u \tag{3.8}$$

$$\frac{\partial N_c}{\partial t} = \frac{\beta_{TPA}}{2h\omega}\left[\frac{|u|^2}{A_{eff}}\right]^2 - \frac{N_c}{\tau_c} \tag{3.9}$$

where u is the slowly varying field amplitude, β_2 is second-order dispersion coefficient, n_2 is nonlinear Kerr coefficient, β_{TPA} is the two-photon absorption coefficient, A_{eff} is the effective mode area, N_c is the free carrier density, σ is the free carrier absorption coefficient, k_c is free carrier dispersion coefficient, α_l is the linear loss parameter and τ_c is the free carrier lifetime. Equations 3.8 and 3.9 are solved using a split-step Fourier method [54] to model the nonlinear parameters in a-Si:H.

Split-Step Fourier Method

The split-step Fourier method can be better understood by splitting Equation 3.8 into dispersive and nonlinear parts as shown in Equation 3.10.

$$\frac{\partial A}{\partial z} = \left(\hat{D} + \hat{N}\right)A \tag{3.10}$$

$$\begin{aligned} \widehat{D} &= -\frac{i\beta_2}{2}\frac{\partial^2}{\partial T^2} + \frac{\beta_3}{6}\frac{\partial^3}{\partial T^3} - \frac{\alpha}{2} \\ \widehat{N} &= i\gamma\left(|A|^2 + \frac{i}{\omega_0}\frac{1}{A}\frac{\partial}{\partial T}\left(|A|^2 A\right) - T_R\frac{\partial|A|^2}{\partial T}\right) \end{aligned} \tag{3.11}$$

$\widehat{D}$ is the differential operator that accounts for dispersion and losses within a linear medium and $\widehat{N}$ is a nonlinear operator that governs the effect of waveguide nonlinearities on pulse propagation. In the split-step Fourier method, the solution is obtained based on the assumption that in propagating the optical field over a small distance *h*, the dispersive and nonlinear effects act independently of each other. The propagation from *z* to *z* + *h* is assumed to be carried out in two steps. In the first step, the nonlinearity acts alone, and $\hat{D} = 0$ in Equation 3.10. In the second step, the dispersion acts alone, and $\hat{N} = 0$ in Equation 3.10. Equation 3.10 then evaluates to:

$$A(z+h,T) \approx \exp(h\hat{D})\exp(h\hat{N})A(z,T) \tag{3.12}$$

The exponential operator $\exp(h\hat{D})$ can be evaluated in the Fourier domain using the relation

$$\exp(h\hat{D})B(z,T) = F_T^{-1}\exp\left[h\hat{D}(-i\omega)\right]F_T B(z,T) \tag{3.13}$$

F_T is the Fourier transform operator and $\hat{D}(-i\omega)$ is value of $\hat{D}$ in frequency space.

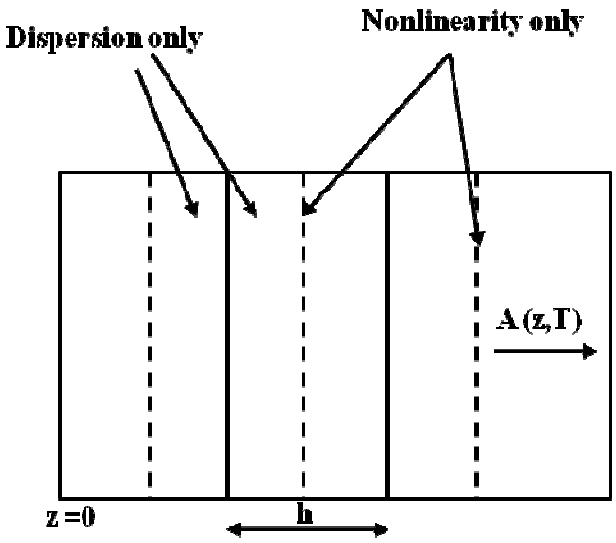

Figure 3.14 Schematic illustration of a symmetric split-step Fourier method used for numerical modeling. The waveguide length is divided into a large number of segments of width *h*. Within a segment, the effect of nonlinearity is included at the mid-plane shown by a dashed line.

$$A(z+h,T) \approx \exp(\frac{h}{2}\hat{D}) \exp(\int_{z}^{z+h} \hat{N}(z')dz') \exp(\frac{h}{2}\hat{D}) A(z,T) \qquad (3.14)$$

The split-step Fourier method can be implemented based on Equation 3.14 and Figure 3.14. The waveguide length is divided into a large number of segments that do not have to be spaced equally. The optical pulse is propagated between each segment according to Equation 3.14. The pulse is first propagated for a distance *h/2* considering dispersion only using the FFT algorithm of Equation 3.13. At the mid-plane *z+h/2*, the field is multiplied by a nonlinear term that represents the effect of the nonlinearity over the length *h*. Then the pulse is propagated over the remaining distance *h/2* with dispersion only to obtain *A(z+h,T)*.

Four-Wave Mixing

Signal amplification and wavelength conversion are essential for an integrated optical interconnect system to route signals over long distances. Signal amplification is

necessary to maintain the signal/noise ratio in the system and the ability to transfer data from an existing signal to a different wavelength has enormous potential in a wavelength division multiplexed system (WDM). Four-wave mixing (FWM), a third-order nonlinear parametric process, is capable of achieving both signal amplification as well as wavelength conversion. Four-wave mixing occurs when photons from one or more waves are annihilated and new photons are created at different frequencies such that the total momentum and energy of the process are conserved as shown in Figure 3.15.

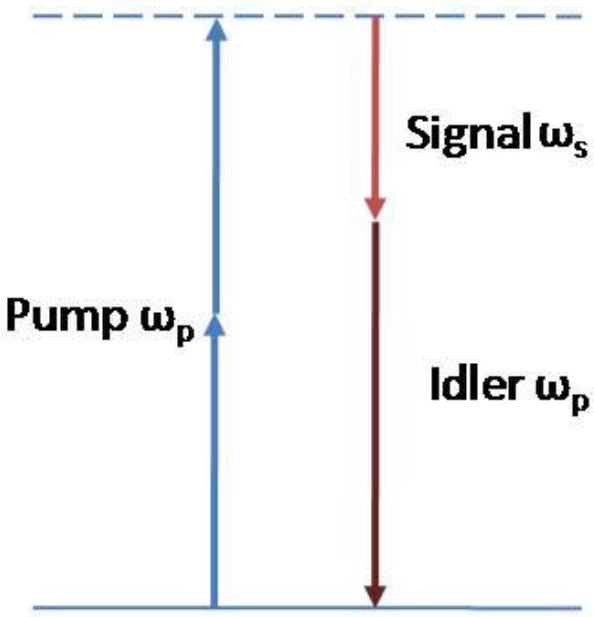

Figure 3.15 Schematic description of Four-wave mixing (FWM) process.

The creation of the signal and idler waves depends on the degree of phase mismatch between propagation constants of the waves and the nonlinear effects of self-phase modulation (SPM) and cross-phase modulation (XPM). The phase matching condition is given by [54]

$$\kappa = \gamma(P_1 + P_2) - \Delta k \tag{3.15}$$

$$\Delta k = k_1 + k_2 - k_3 - k_4 \tag{3.16}$$

$$\Delta k = (n_1\omega_1 + n_2\omega_2 - n_3\omega_3 - n_4\omega_4)/c \tag{3.17}$$

where Δk is the net propagation constant, γ is the nonlinear coefficient, P_1, P_2 are the pump powers and ω_1, ω_2, ω_3 and ω_4 are the pump, signal and idler frequencies respectively. Under the condition when the pump powers are equal (P_1=P_2, ω_1=ω_2), the phase matching condition is given as

$$\kappa = 2\gamma P_{pump} - \Delta k \tag{3.18}$$

$$\Delta k = 2k_{pump} - k_{signal} + k_{idler} \tag{3.19}$$

If a signal photon propagates along with the pump photons, then the signal photon undergoes amplification from the four-wave mixing process given by

$$g = \sqrt{(\gamma P_{pump})^2 - (\kappa/2)^2} \tag{3.20}$$

A schematic of wavelength conversion and gain in a-Si:H waveguides is shown in Figure 3.16.

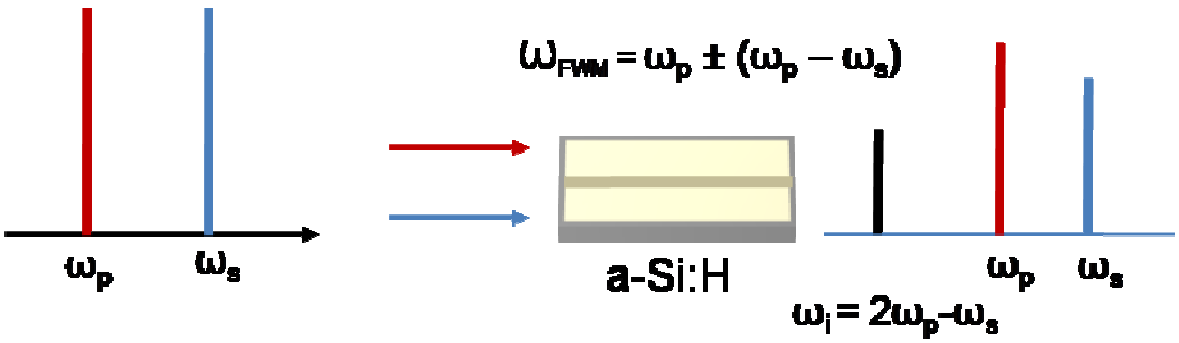

Figure 3.16 Schematic of four-wave mixing in a-Si:H with gain and wavelength conversion.

When a strong pump ω_p and co-propagating signal ω_s are launched in the waveguide, the refractive index of waveguide is modulated due to the strong nonlinear Kerr effect at the frequency ω_s-ω_p. This causes the pump wave to be modulated at the same frequency and

the generation of side-band frequencies $\omega_p \pm (\omega_s-\omega_p)$. This results in the signal frequency ω_s causing an amplification of the signal and an 'idler' frequency $\omega_i = 2\omega_p-\omega_s$.

3.5.3 Amplitude-Shift-Keying Modulation in a-Si:H Waveguides

In Chapter **6**, we demonstrate a novel data encoding scheme using a system of ring resonators in a-Si:H to increase the spectral efficiency of an interconnect link. Thermo-optic modulation of a-Si:H waveguides is utilized to demonstrate a proof-of-concept three-level data encoding scheme. A high-speed data modulation is also demonstrated using all-optical modulation of a pair of symmetric ring resonators in crystalline silicon waveguides.

CHAPTER 4

ALL-OPTICAL MODULATION IN HYDROGENATED-AMORPHOUS-SILICON (a-Si:H) WAVEGUIDES

4.1 Deposition of a-Si:H-on-Insulator Substrates

Device quality substrates in hydrogenated-amorphous silicon (a-Si:H) were obtained using plasma-enhanced chemical vapor deposition (PECVD). A 3-µm thick wet-oxide is grown on top of a lightly p-doped <100> silicon substrate by thermal oxidation. The oxide is required to prevent the coupling of the optical mode to the silicon substrate. Hydrogenated amorphous silicon is then deposited using PECVD to form a silicon-on-insulator substrate. The parameters used for the deposition of the film are given in Table 4.1. The optical properties of the films are characterized using a spectroscopic ellipsometer. The thickness of the deposited film is determined to be ~250 nm and the refractive index measured to be 3.51 at 1550 nm.

Table 4.1 PECVD deposition parameters for a-Si:H

Silane (SiH4) flow	60 sccm
Helium (He) flow	1800 sccm
RF Power	300 W
Substrate Temperature	400 C
Pressure	3 Torr
Deposition Rate	42 nm/min

Passive amorphous silicon (a-Si:H) devices are demonstrated by patterning microdisc and microring resonators on the deposited films. The devices are patterned using a Leica VB6-HR electron beam lithography system. The substrate is first coated with XR-1541

(hydrogen silsequioxane, HSQ), a negative e-beam resist before being patterned using e-beam lithography. After patterning, the features are transferred to the substrate by developing the resist using an AZ® 300 MIF developer followed by etching the silicon using a chlorine based inductively coupled plasma (ICP) etch. The etched waveguides are then clad with a 2 µm thick PECVD SiO_2 to protect the optical mode. The process steps are illustrated in Figure 4.1.

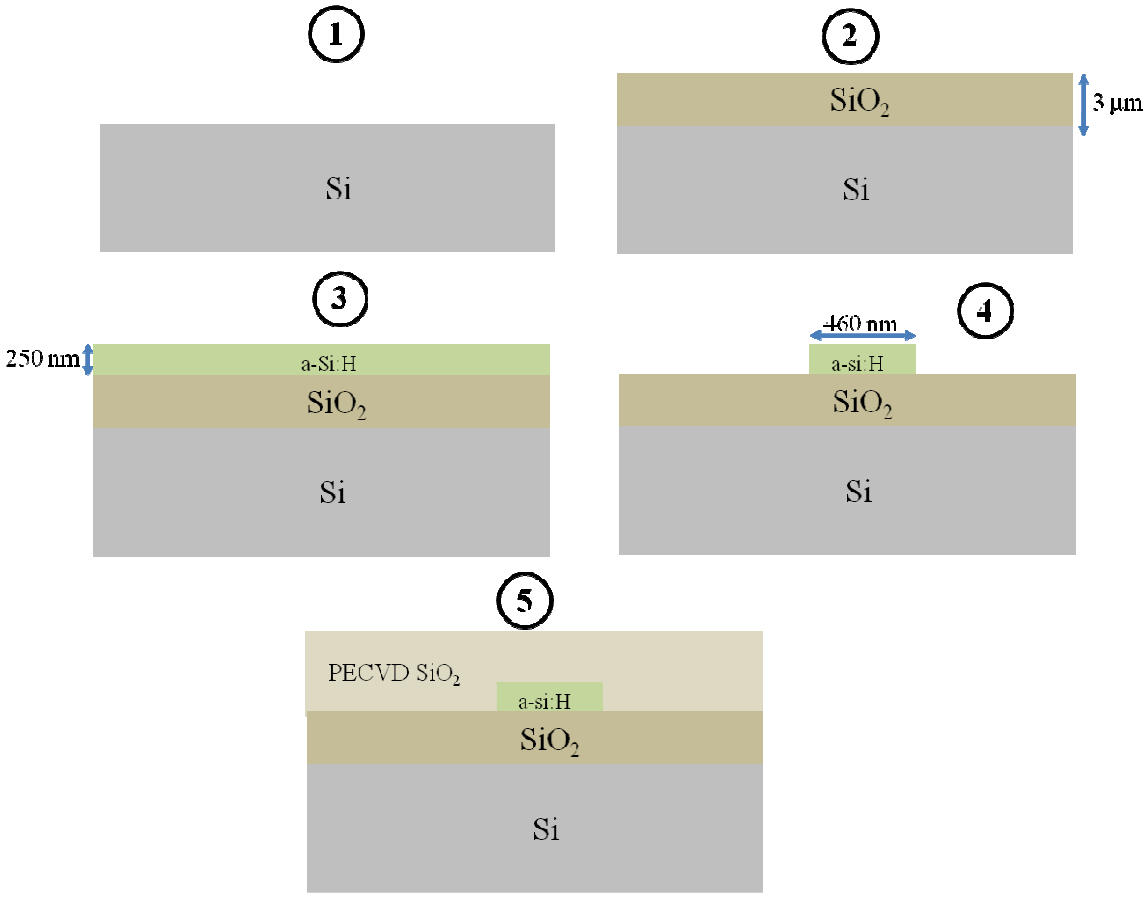

Figure 4.1 The process flow for fabrication of devices on a-Si:H-on-insulator substrates. Step 1/2: Grow 3 µm thick wet oxide on a silicon substrate. Step 3: Deposit 250 nm thick a-Si:H using PECVD. Step 4: Pattern waveguides using e-beam lithography and etch a-Si:H. Step 5: Deposit 2 is µm thick PECVD SiO_2 to protect the optical mode.

The dimensions of the waveguide are designed to be 450 nm wide and 250 nm tall in order to support the fundamental mode of propagation. Figure 4.2 illustrates a simulated

profile of a fundamental quasi-TE (electric field parallel to the substrate) mode on the designed waveguide.

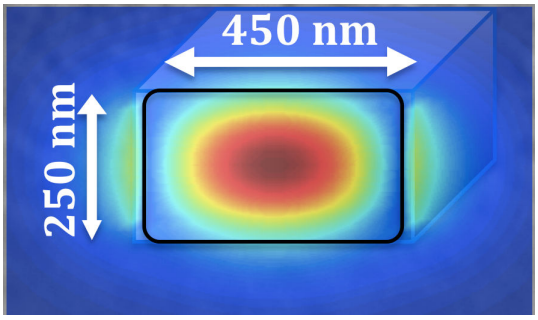

Figure 4.2 Mode profile of a fundamental quasi-TE mode in a-Si:H waveguide.

4.2 Passive Devices on a-Si:H-on-Insulator Substrates

To demonstrate low-loss high quality devices on the deposited a-Si:H film, passive microring and microdisc resonators are patterned using e-beam lithography as described in section 4.1. The fabricated resonator devices measure 10 μm in diameter. The scanning electron micrograph (SEM) images of the patterned microdisc and microring devices are shown in Figure 4.3.

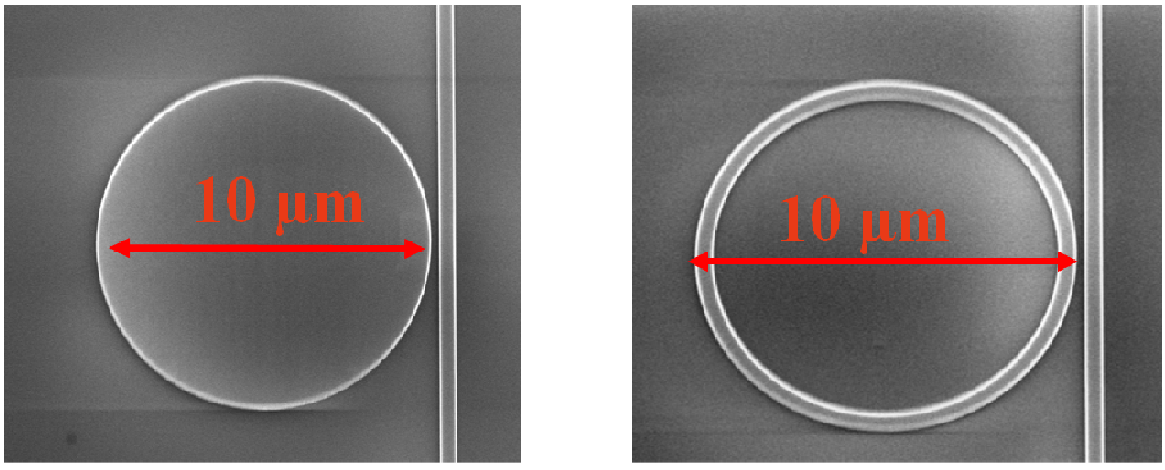

Figure 4.3 SEM images of fabricated microdisc (left) and microring (right) resonators in a-Si:H.

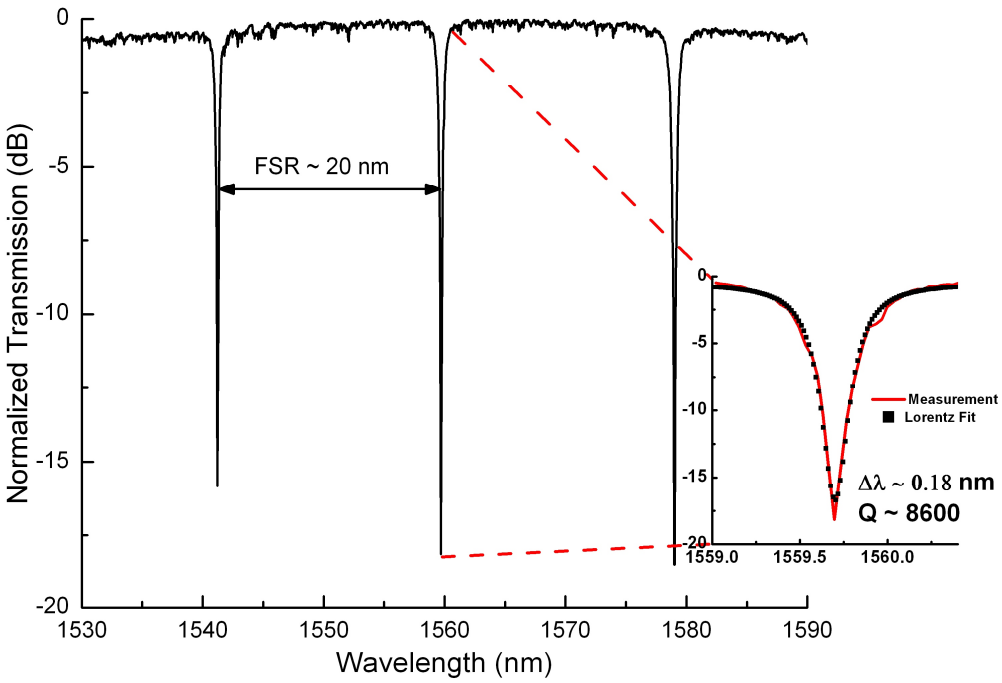

Figure 4.4 Measured transmission spectrum of ring resonators fabricated in a-Si:H. The measured free spectral range is ~ 20 nm. Inset shows the measured Q-factor to be ~ 8600 based on a Lorentzian fit to the measured spectrum.

The transmission spectrum of the resonators are measured by launching quasi-TE polarized (electric field parallel to the substrate) light into the input waveguides from a tunable continuous wave laser source through a polarization controller using tapered lens fiber. The output from the chip is collected using another tapered lens fiber and scanned to measure the transmission spectrum. Tapered adiabatic couplers were used to couple light into and out of the devices [55]. The measured transmission spectrum of the ring resonator is shown in Figure 4.4. From the spectrum, the free spectral range (FSR), defined as the spectral distance between two adjacent resonances, is measured to be ~ 20 nm. This yields a group index (n_g) of ~ 4.04 for the mode propagating in the resonator, based on the relationship between the free spectral range and the group index

$$FSR = \frac{\lambda^2}{n_g \cdot 2\pi R} \tag{4.1}$$

The measured quality factor ($Q \approx \lambda_0 / \Delta\lambda_{FWHM}$) of the ring resonators is ~ 8,600 based on a Lorenztian fit to the measured spectrum. The quality factor is related to the photon lifetime (τ_p) in the cavity as

$$\tau_p = \frac{Q\lambda}{2\pi c} \tag{4.2}$$

Based on the measured Q factor, the photon lifetime in the cavity is estimated to be ~ 7 ps.

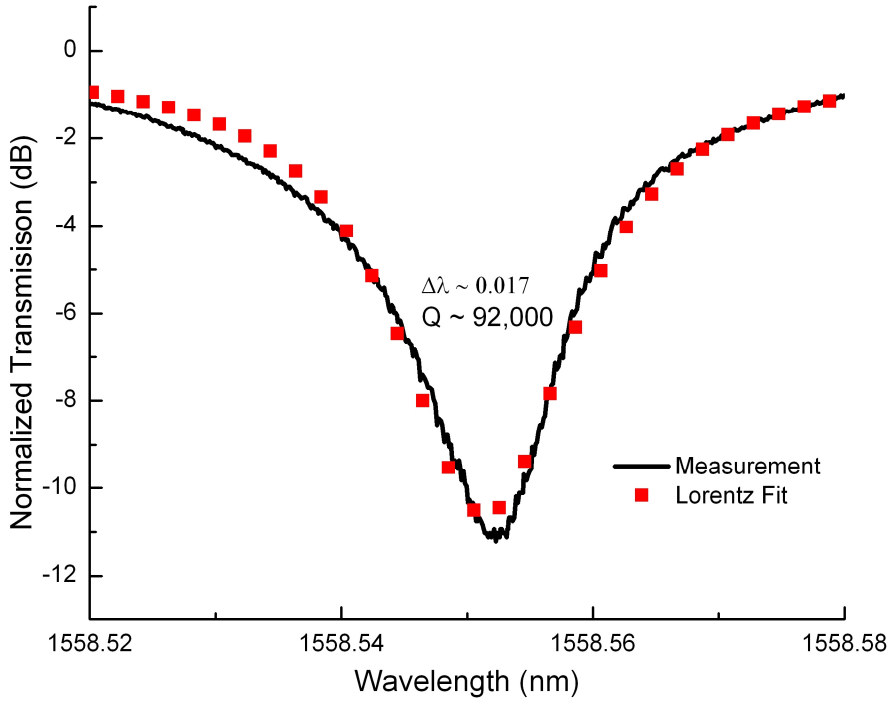

Figure 4.5 Measured response of microdisc resonators fabricated in a-Si:H. The measured Q-factor is ~ 92,000.

The transmission spectrum of the microdisc resonators with a measured Q-factor of ~ 92, 000 is shown in Figure 4.5. From these measurements, the material loss in the a-Si:H is

determined to be less than 3.5 dB/cm which can be considered to be low enough to realize a platform of high quality, low optical loss devices on a chip.

4.3 Drude-Lorentz model in Semiconductors

The transmission of information through an optical interconnect requires the need for optical carrier signals to be modulated, enabling encoding of information. Active modulation of light can be achieved from the free-carrier plasma dispersion effect, which causes a change in refractive index and absorption of silicon due to the injection of carriers. The change in refractive index and absorption due to change in free-carriers is given by the following equations [56]

$$\Delta n = -\frac{e^2\lambda^2}{8\pi^2 c^2 \varepsilon_0 n}\left[\frac{\Delta N_e}{m^*_{ce}} + \frac{\Delta N_h}{m^*_{ch}}\right] \tag{4.3}$$

$$\Delta \alpha = \frac{e^3\lambda^2}{4\pi^2 c^3 \varepsilon_0 n}\left[\frac{\Delta N_e}{m^{*2}_{ce}\mu_e} + \frac{\Delta N_h}{m^{*2}_{ch}\mu_h}\right] \tag{4.4}$$

In Equations 4.3 and 4.4, e is the electron charge, λ is the probe wavelength, ε_0 is permittivity of free space, n is the refractive index of the material, m^*_{ce} and m^*_{ch} are the effective masses of electrons and holes, μ_e and μ_h are the mobilities of the carriers in a-si:H , ΔN_e and ΔN_h are the change in the carrier concentrations of electrons and holes respectively. Active all-optical modulation of light due to photo-injection of carriers in crystalline silicon and polycrystalline silicon waveguides has already been demonstrated [57, 58]. The free-carrier lifetime is the main limiting factor in the modulation speed of the devices. The free-carrier lifetimes in crystalline silicon have been measured to be $\tau_c \sim$ 450 ps – 1 ns [57] and the carrier lifetime in polysilicon waveguides has recently been

measured to be $\tau_c \sim 135$ ps [58]. However, optical modulation of light in crystalline silicon and polysilicon needs a resonant cavity to enhance the modulation effect and is therefore bandwidth limited. Here, in order to show that a-Si:H is a viable platform for high performance active nanophotonic devices, we demonstrate broadband and high speed all-optical modulation in a compact device.

4.4 Broadband All-Optical Modulation in a-Si:H Waveguides

Modulation is achieved by using a short optical pump pulse to induce an absorption change in an a-Si:H waveguide (460 nm wide x 250 nm tall) as shown in Figure 4.6. A mode-locked Ti-Sapphire laser tuned to 810 nm provides 100 fs pump pulses at a 80 MHz repetition rate that are frequency doubled using a beta-barium borate (BBO) crystal to 405 nm. The frequency doubled pump pulses are then coupled into a SMF-28 fiber using a fiber collimator (optimized for $\lambda = 405$ nm) and are incident on top of an amorphous silicon waveguide. We estimate that at least 90% of the incident pump pulse is absorbed in the a-Si:H within a ~ 15 μm diameter spot. The free-carriers generated by the pump are used to modulate a continuous-wave tunable laser diode at λ=1550 nm. The probe (polarized to be quasi TE or E-field parallel to the substrate) is coupled into the waveguide using a tapered lens fiber. The modulated probe output is detected using a 20 GHz photodetector and the temporal response is observed with a 40 GHz digital sampling oscilloscope.

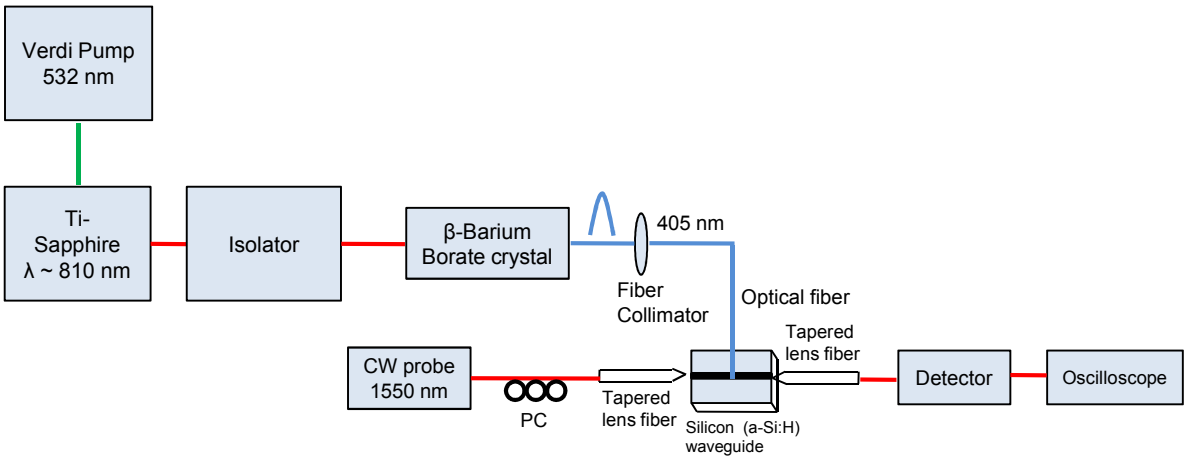

Figure 4.6 Experimental set-up to demonstrate amplitude modulation in a-Si:H waveguides. The 405 nm pump pulses are incident on an a-Si:H waveguide to modulate the 1550 nm cw probe light. PC: Polarization Controller.

It is seen in Figure 4.7 that the probe amplitude is quickly modulated by each pump pulse. This modulation can be attributed to free-carrier absorption induced by the photo-excited carriers generated through linear absorption of the pump pulse (the quasi-bandgap of a-Si:H is ~ 1.7 eV). Here, the probe undergoes a ~ 3 dB modulation when the incident pump pulse energy is E_{pump} = 75 pJ. Due to the poor overlap of the pump light with the a-Si:H waveguide, it is estimated that only 1.5 pJ of the pump energy is actually absorbed in the waveguide. Consequently, the modulation depth could be improved with better overlap. It is also observed in Figure 3.7 that there are two distinct time-scales in the modulation of the probe - a fast and a slow component. The fast transition occurs when the pump photons are absorbed.

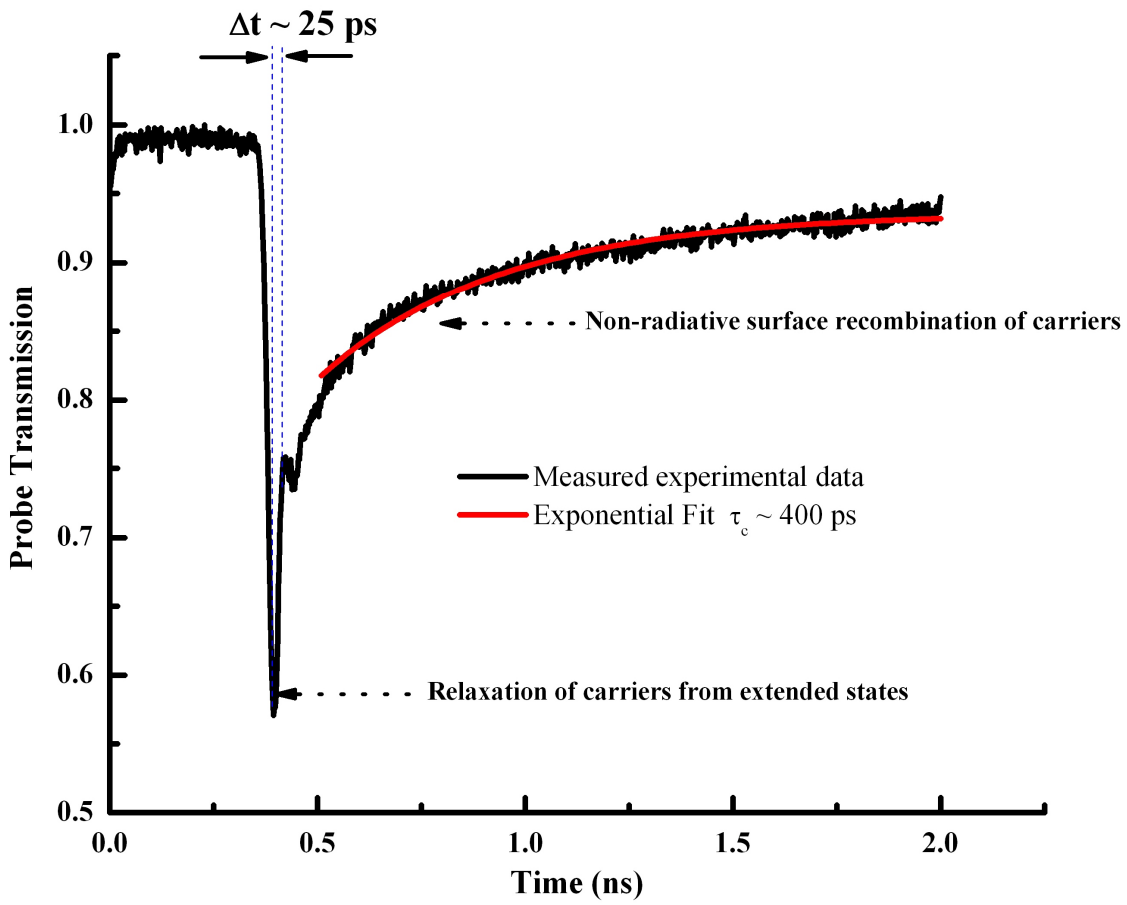

Figure 4.7 All-optical modulation in a-Si:H using a pump-probe scheme. The carriers undergo a rapid thermalization before undergoing non-radiative recombination.

Since the photon energy is much larger than the quasi-bandgap energy, the electrons are initially excited high into the conduction band, which dramatically increases the free-carrier absorption. The carriers then rapidly thermalize into the extended band tail states in the conduction band [41, 59]. The exact time-scale over which the thermalization occurs could not be determined because the transition was limited by the time-response of our detector/oscilloscope however, in other works, it was determined that the carriers thermalize over a time-scale of less than 5 picoseconds [41]. After the thermalization, there is a slow return (~ 400 ps) of the signal which is attributed to surface recombination of free carriers with the etched sidewalls of the waveguide. It

should be noted that this recombination time is comparable to what is seen in similarly sized crystalline waveguides [57, 58]. It is also to be noted that the slow temporal components' maximum absorption is less than that of the faster temporal component. We attribute this to a density-of-state dependent free-carrier absorption coefficient as previously observed and discussed in more detail in [41, 59].

In order to verify the enhancement of free-carrier absorption in a-Si:H, an identical experiment performed in crystalline silicon waveguide did not result in the modulation of the probe signal. The enhancement in a-Si:H can be understood by considering the Drude model, where free-carrier scattering introduces optical absorption. The applicability of the Drude model to an amorphous material has been shown to give good agreement with experimental results [41]. The free carrier absorption cross-section σ, describing the change in the absorption due to change in free carrier concentration is given by [56]

$$\sigma = \frac{e^3 \lambda^2}{4\pi^2 c^3 \varepsilon_0 n_0} \left(\frac{1}{m_{ce}^2 \mu_e} + \frac{1}{m_{ch}^2 \mu_h} \right) \tag{4.5}$$

In Equation 4.5, e is the electron charge, λ is the probe wavelength, ε_0 is permittivity of free space, n_0 is the refractive index of the material, m_e and m_h are the effective masses of electrons and holes, μ_e and μ_h are the mobilities of the carriers in a-si:H. Substituting for $m_e = 0.5 \cdot m_o$, $m_h = 1.0 \cdot m_o$, $m_o = 9.1 \cdot 10^{-31}$ Kg, $\mu_e = 2.0$ cm^2/V·s, $\mu_h = 0.4$ cm^2/V·s [41] in Equation 3.5, yields a theoretically estimated value of $\sigma = 1.63 \cdot 10^{-16}$ cm^2. Consequently, free-carrier absorption in a-Si:H is at least an order of magnitude higher than in crystalline silicon ($\sigma = 1.45 \cdot 10^{-17}$ cm^2) [51]. From the degree of modulation seen in Figure 4.7, it is estimated that a free-carrier density of $N \sim 1.98 \cdot 10^{18}$ cm^{-3} was injected

into the waveguide. This can be confirmed from calculating the carrier density induced by an absorbed pulse energy of 1.5 pJ, yielding a carrier density of $N \sim 1.52 \cdot 10^{18}$ cm^{-3}, which is in very good agreement with the estimate from the Drude model.

4.5 In-plane All-Optical Absorption Modulation in a-Si:H Waveguides

In order to further characterize the broadband modulation in a-Si:H waveguides, we employed an in-plane pump-probe modulation scheme as shown in Figure 4.8.

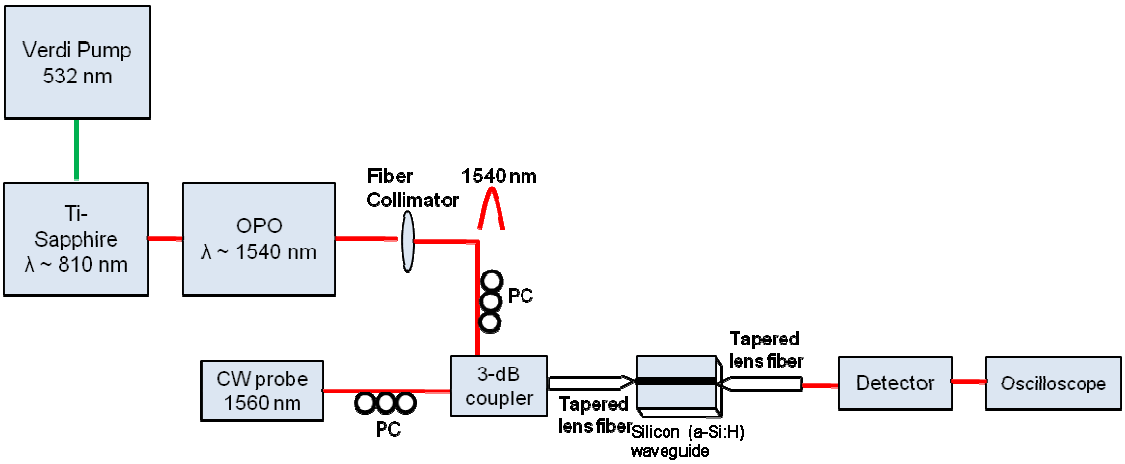

Figure 4.8 In-plane experimental set-up to demonstrate broadband amplitude modulation in a-Si:H waveguides. The 1540 nm pump pulses are coupled into an a-Si:H waveguide to modulate the 1560 nm cw probe light. PC: Polarization Controller. OPO: Optical Parametric Oscillator.

The 100 fs, 800 nm pulses from a mode-locked Ti-sapphire pulses are used as a pump source to an optical parametric oscillator (OPO) to generate ~ 180 fs pump pulses at 1540 nm. The pump pulses are coupled along with a continuous wave (cw) probe signal at 1560 nm using a 3-dB coupler. The coupled signals are then launched into an a-Si:H waveguide using tapered lens fiber as illustrated in Figure 4.8. The output from the chip is collected using another tapered lens fiber and detected using a 20 GHz detector and the temporal response observed on a 40 GHz digital sampling oscilloscope.

The response observed on the oscilloscope is seen in Figure 4.9 shows that the cw probe undergoes ~ 80% modulation due to the strong pump pulse. The observed temporal response is similar to Figure 4.7. The absorption of the pump pulse (1540 nm) generates carriers due to the strong two-photon-absorption (TPA) coefficient in a-Si:H. The generated carriers cause an absorption modulation of the probe signal (1560 nm) as seen in the spectral response. The excited carriers rapidly thermalize to the bottom of the band tail states and then gradually recombine with the etched sidewalls of the waveguide. The strong modulation (~ 80%) can be attributed to the strong overlap between the pump and the probe pulses and also to the enhanced free-carrier absorption coefficient in a-Si:H measured in Section 4.4. The recombination lifetime of the carriers is estimated with an exponential fit to the measure spectrum to be ~ 400 ps as measured with the scheme described in Section 4.4.

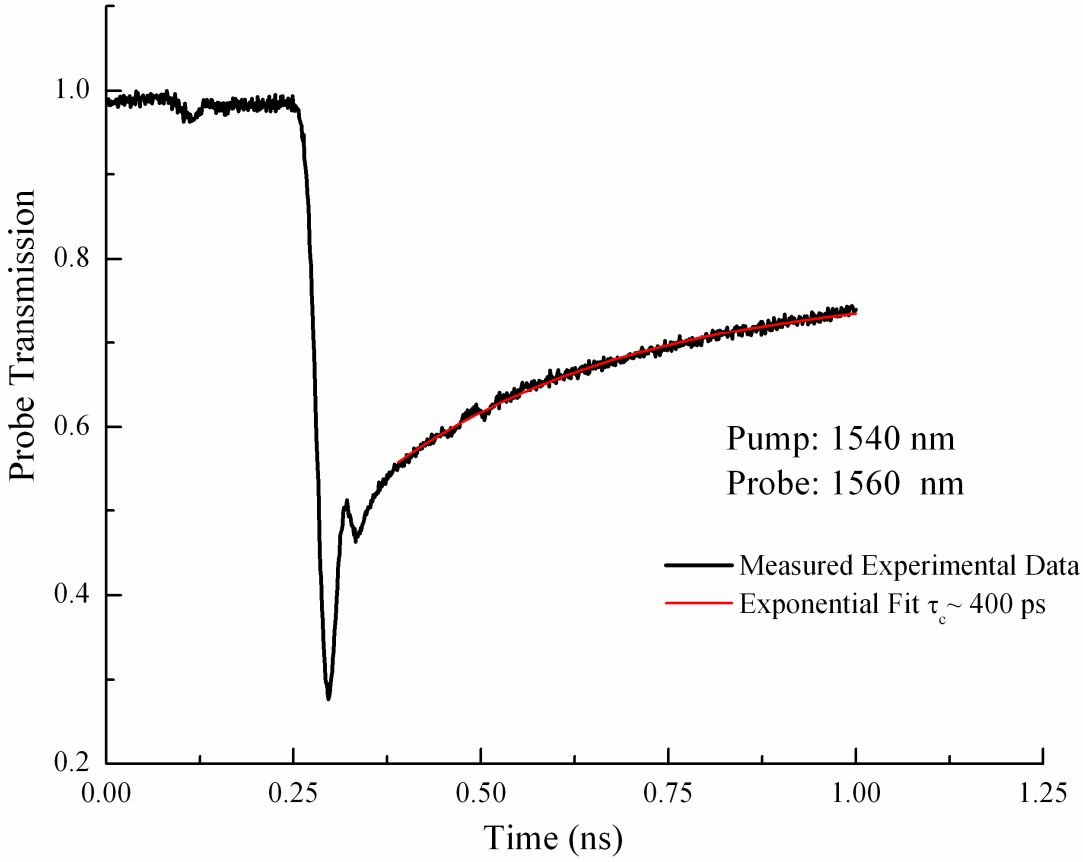

Figure 4.9 In-plane all-optical modulation in a-Si:H using a pump-probe scheme. The carriers undergo a rapid thermalization before undergoing non-radiative recombination with a carrier lifetime of ~ 400 ps.

4.6 All-Optical Modulation in SOI Ring Resonator

To measure the free-carrier lifetime in SOI waveguides, the pump-probe modulation scheme was used to switch a probe signal operating below resonance in a 10 μm wide ring resonator similar to that seen in Figure 4.3. The probe signal, initially, below the resonance wavelength, is not coupled into the ring resonator resulting in a high transmission of the signal as seen in the inset in Figure 4.10. The experimental set-up used is similar to Figure 4.6. The modulation is achieved with 75 pJ, 410 nm pump pulses incident on the ring resonator operating slightly below resonance. The absorption of the

pump pulse results in the generation of carriers in the ring resonator. The resultant carriers cause a change in the effective index in the ring resonator according to equation (4.3). The resultant change in index causes the probe signal to be on resonance; thereby resulting in a transmission minimum of the probe signal. The plot of the probe signal undergoing modulation is shown in Figure 4.10. The generated carriers undergo a gradual recombination with the etched sidewalls of the ring resonator thereby resulting in a transmission maximum of the probe signal. An exponential fit to the measured spectrum yields a carrier recombination lifetime of 450 ps that is consistent with measured values in similar sized SOI waveguides [57].

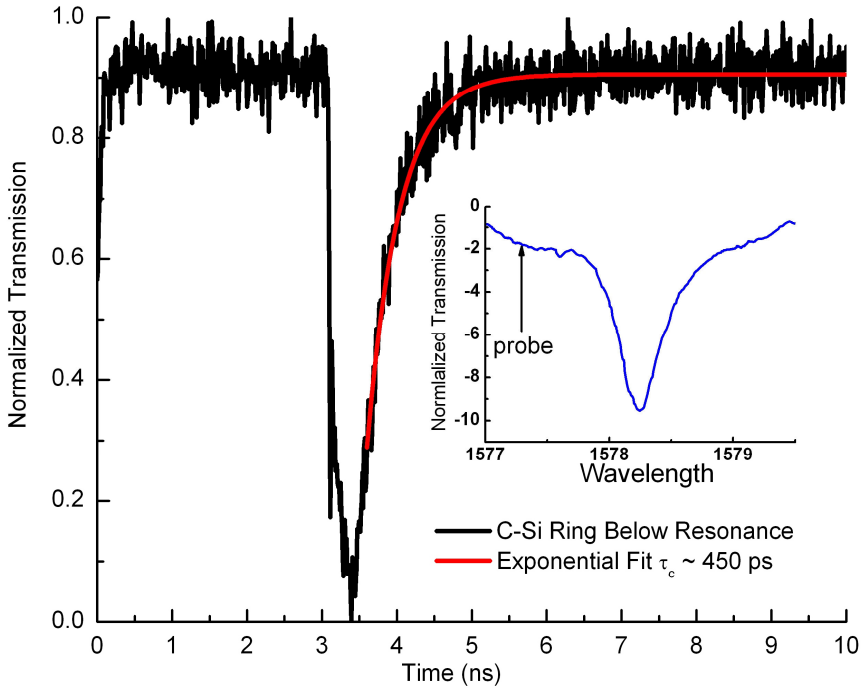

Figure 4.10 All-optical modulation in a SOI ring resonator using a pump-probe scheme. Inset shows the transmission spectrum of the ring resonator with the probe signal wavelength below the resonance wavelength of the ring resonator.

Table 4.2 Comparison between free-carrier lifetimes and free-carrier absorption coefficient in a-Si:H and SOI

Parameter	a-Si:H	SOI
Free-carrier lifetime	400 ps	450 ps
σ_{fca}	$1.63 \cdot 10^{-16}$ cm^2	$1.45 \cdot 10^{-17}$ cm^2

A comparison of free-carrier lifetime and free-carrier absorption co-efficient between a-Si:H and SOI is given in Table 4.2.

In this chapter, low loss, high quality factor passive optical devices in hydrogenated-amorphous silicon have been demonstrated that can form the basis of wavelength-division multiplexing based optical interconnects. Furthermore, broadband, all-optical modulation in low loss a-Si:H waveguides have also been demonstrated. Significant modulation (~ 3 dB) occurs with a device of only 15 μm without the need for cavity interference effects in stark contrast to an identical crystalline silicon waveguide. The enhanced modulation is attributed to the significantly larger free-carrier absorption effect of a-Si:H, estimated here to be $\Delta\alpha = 1.63 \cdot 10^{-16} \cdot \Delta N$ cm^{-1}. The modulation time is measured to be only $\tau_c \sim 400$ ps, which is comparable to recombination rate measured in sub-micron crystalline silicon waveguides illustrating the strong dominance of surface recombination in similar sized (460 nm x 250 nm) a-Si:H waveguides. Consequently, a-Si:H could serve as a high performance platform for backend integrated CMOS photonics.

CHAPTER 5

OPTICAL NONLINEARITIES IN HYDROGENATED-AMORPHOUS- SILICON WAVEGUIDES

5.1 Experimental Set-up for Measurement of Optical Nonlinearities

In this chapter, we characterize the optical nonlinearities in hydrogenated-amorphous silicon waveguides through the propagation of ultra-short (~ 180 fs) pulses through a sub-micron waveguide. The nonlinear processes are modeled using a modified nonlinear Schrödinger equation (NLSE) which takes into account free-carrier effects.

The amorphous silicon waveguides are fabricated from a 250 nm thick a-Si:H-on-insulator film deposited using plasma enhanced chemical vapor deposition (PECVD) at 400 ºC. The deposition parameters of the film can be found in Chapter 4. Strip waveguides, 460 nm wide, were patterned using electron beam lithography, followed by inductively coupled plasma (ICP) chlorine etch. Silicon waveguides of similar dimensions were patterned on a 250 nm thick silicon-on-insulator substrate.

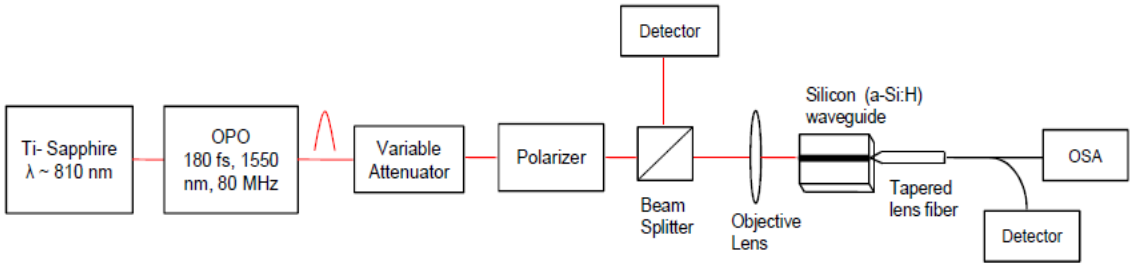

Figure 5.1 Experimental set-up to measure optical nonlinearities in a-Si:H waveguides. OPO: Optical Parametric Oscillator, OSA: Optical Spectrum Analyzer.

The optical nonlinear properties in amorphous silicon were determined by launching ultra short pulses into sub-micron sized waveguides and measuring the output as a function of the input power as shown in Figure 5.1. The input pulses (~100 fs, 810 nm)

from a mode-locked Ti-sapphire laser were used as a pump source to an optical parametric oscillator (OPO) to generate ~180 fs pulses at a repetition rate of 80 MHz at 1550 nm. The input power, controlled using a variable attenuator, passes through a polarizer, a beam splitter, and then is coupled through free space into the waveguides using a 0.25 NA, 12 mm focal length objective lens. The polarizer was adjusted to excite TE (electric field parallel to substrate) mode in the waveguides. Free space coupling was used to launch light into the waveguides in order to eliminate nonlinearities induced in fibers from affecting the transmission spectra through the waveguides. The output from the chip was collected using a tapered lensed fiber and measured using an optical spectrum analyzer (OSA). Adiabatic inverse tapers were used to couple light on and off the chip [55].

5.2 Theory of Non-linear Propagation in Waveguides

The propagation of optical pulses through a waveguide can be modeled based on the following set of nonlinear differential equations, which are derived from the nonlinear Schrödinger equation [51-54],

$$\frac{\partial u}{\partial z}+i\frac{\beta_2}{2}\frac{\partial^2 u}{\partial t^2}=\left(i\frac{\omega}{c}n_2-\frac{\beta_{TPA}}{2}\right)\frac{|u|^2}{A_{eff}}u-\frac{N_c}{2}\left(\sigma-i\frac{\omega}{c}k_c\right)u-\frac{\alpha_l}{2}u \tag{5.1}$$

$$\frac{\partial N_c}{\partial t}=\frac{\beta_{TPA}}{2h\omega}\left[\frac{|u|^2}{A_{eff}}\right]^2-\frac{N_c}{\tau_c} \tag{5.2}$$

where u is the slowly varying field amplitude, β_2 is second-order dispersion coefficient, n_2 is nonlinear Kerr coefficient, β_{TPA} is the two-photon absorption coefficient, A_{eff} is the effective mode area, N_c is the free carrier density, σ is the free carrier absorption

coefficient, k_c is free carrier dispersion coefficient, α_l is the linear loss parameter and τ_c is the free carrier lifetime. Equations (5.1) and (5.2) are solved using a split-step Fourier technique [54] as explained in Section 3.4 of this thesis, to model the behavior of the pulses in a-Si:H waveguides. The second order dispersion co-efficient was neglected in the analysis, since the waveguide lengths used were smaller than the dispersion lengths given by $L_D = T_0^2 / |\beta_2|$, where T_0 is the initial pulse width. The carrier lifetime in the crystalline silicon waveguide is measured to be τ_c = 450 ps [57] and the lifetime in a-Si:H waveguide with similar dimensions is τ_c = 400 ps [60]. Since the carrier lifetimes are much shorter than the repetition rate of the pump pulses, the carrier density accumulation due to prior pulses can be neglected in the analysis. The effective area of the waveguides was determined using a mode solver to be A_{eff} = 0.085 μm^2 for both crystalline and amorphous silicon waveguides. The patterned amorphous silicon (a-Si:H) waveguides are 7 mm long, while the crystalline silicon waveguides measure 6 mm in length.

5.3 Nonlinear Absorption Characterization

To characterize the absorption nonlinearities, the output powers from the waveguides are measured as a function of the coupled input powers. The total insertion loss from the a-Si:H waveguides is measured to be 23 dB at low input powers where nonlinear effects from the waveguide are negligible. The linear transmission loss in the waveguide is measured to be 3.5 dB/cm using the cutback method. The free space coupling loss is calculated to be 15 dB, and the output fiber coupling to be 5 dB. Such a large free-space coupling loss is to be expected with the low numerical aperture (NA) of the lens used.

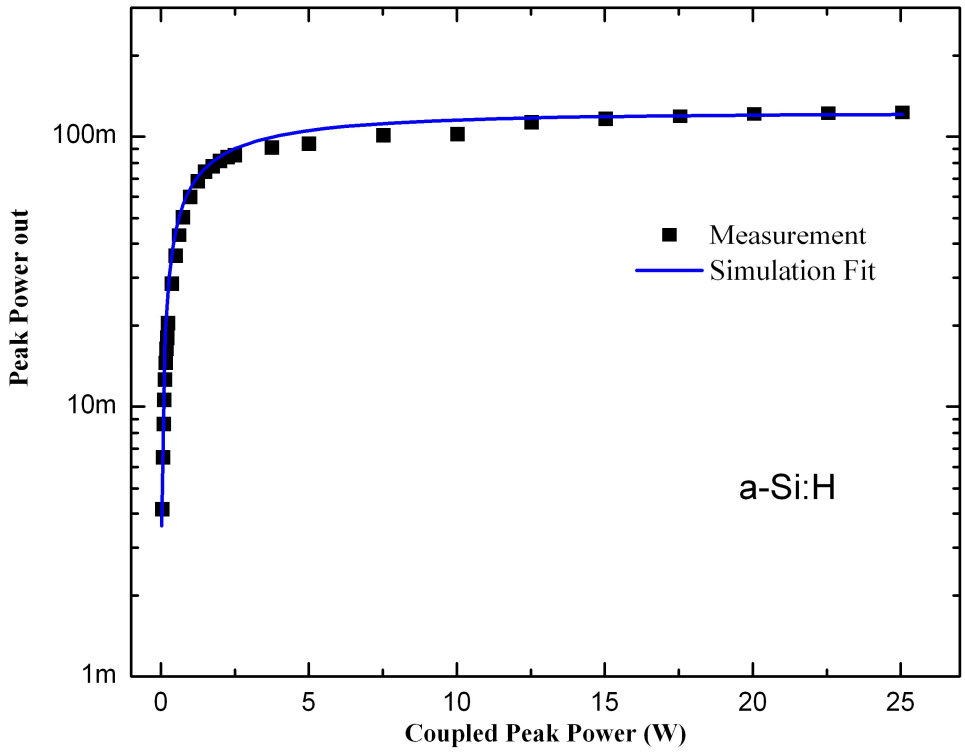

Figure 5.2 Output power (black squares) as function of coupled input power for a-Si:H waveguide. The blue line indicates the fit measured data based on solving the nonlinear equations.

From Figure 5.2, it is observed that output power from the waveguide shows a nonlinear behavior as a function of the coupled input power. The optical limiting of the output in a-Si:H waveguide is attributed to the generation of free carriers due to two photon absorption. From the fit to the measured data, the two-photon absorption coefficient β in a-Si:H is estimated to be 4.1 ± 0.4 cm/GW. Such a large TPA coefficient may come as a surprise since the effective bandgap of a-Si:H is ~ 1.7 eV. However, due to the amorphous nature of the material, there are exponential band tails that exhibit a very high density of states of 10^{19} - 10^{20} cm^{-3} even below 1.6 eV, in turn, allowing for the efficient two-photon absorption observed here [29]. This enhancement in absorption may also be due to two-state absorption where mid-gap localized defect states aid absorption as modeled in [43]. Equations 5.1 and 5.2 were modified to account for mid-

gap states but a much better fit of the experimental data is observed with TPA alone as observed in Figure 5.3.

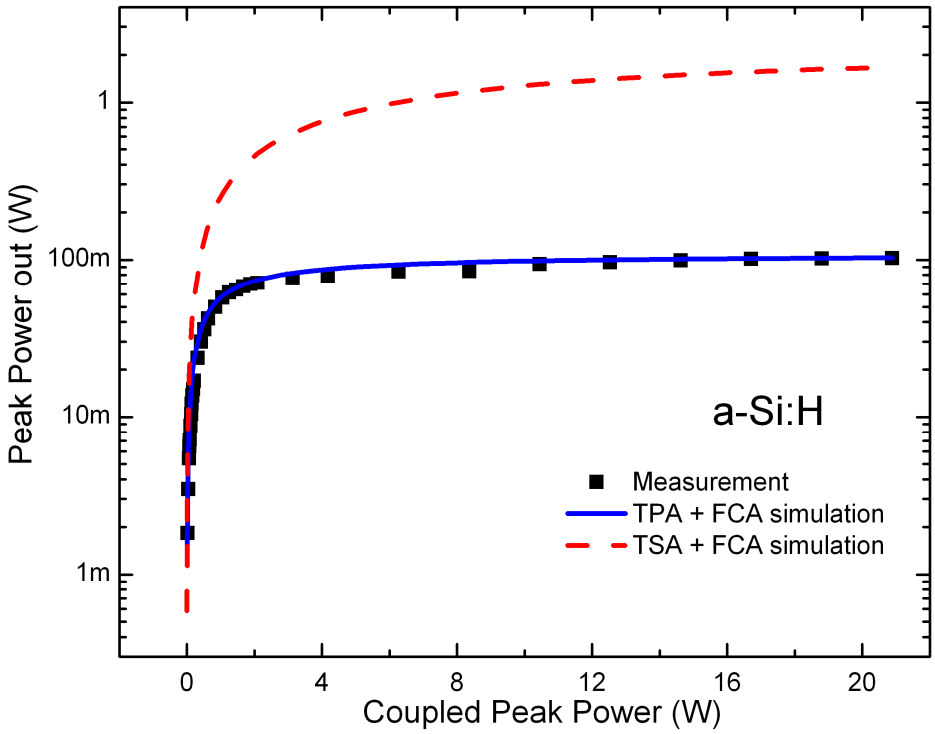

Figure 5.3 Modeling fit to measured data using the two-photon absorption (TSA) and two-state absorption (TSA) model in a-Si:H waveguide.

However, TPA is not the dominating effect in a-Si:H; free-carrier absorption significantly saturates the output. This is observed in Figure 5.2(a) where the output power begins to saturate at 3W peak coupled power. It was determined that this power corresponds to a free carrier density of $1.16 \cdot 10^{17}$ cm^{-3} which is significant enough to induce considerable free-carrier absorption. Through our modeling, the free-carrier absorption coefficient is determined to be $(1.9 \pm 0.3) \cdot 10^{-16}$ cm^2. This can be verified by calculating the free-carrier absorption coefficient σ using the Drude-Lorenz model as given by [56]

$$\sigma = \frac{e^3 \lambda^2}{4\pi^2 c^3 \varepsilon_0 n_0} \left(\frac{1}{m_e^2 \mu_e} + \frac{1}{m_h^2 \mu_h} \right) \tag{5.3}$$

In Equation 5.3, e is the electron charge, λ is the probe wavelength, ε_0 is permittivity of free space, n_0 is the refractive index of the material, m_e and m_h are the effective masses of electrons and holes, μ_e and μ_h are the mobilities of the carriers in a-Si:H. Substituting for $m_e = 0.5 \cdot m_o$, $m_h = 1.0 \cdot m_o$, $m_o = 9.1 \cdot 10^{-31}$ Kg, $\mu_e = 2.0$ cm^2/V·s, $\mu_h = 0.4$ cm^2/V·s [41] in Equation 5.3, yields a theoretically estimated value of $\sigma = 1.6 \cdot 10^{-16}$ cm^2. The measured free carrier absorption coefficient is in very good agreement with the value predicted based on the Drude-Lorentz model. It is to be noted that the measured enhancement of nonlinear absorption in a-Si:H corroborates the reported enhancement in free-carrier nonlinearities in [43].

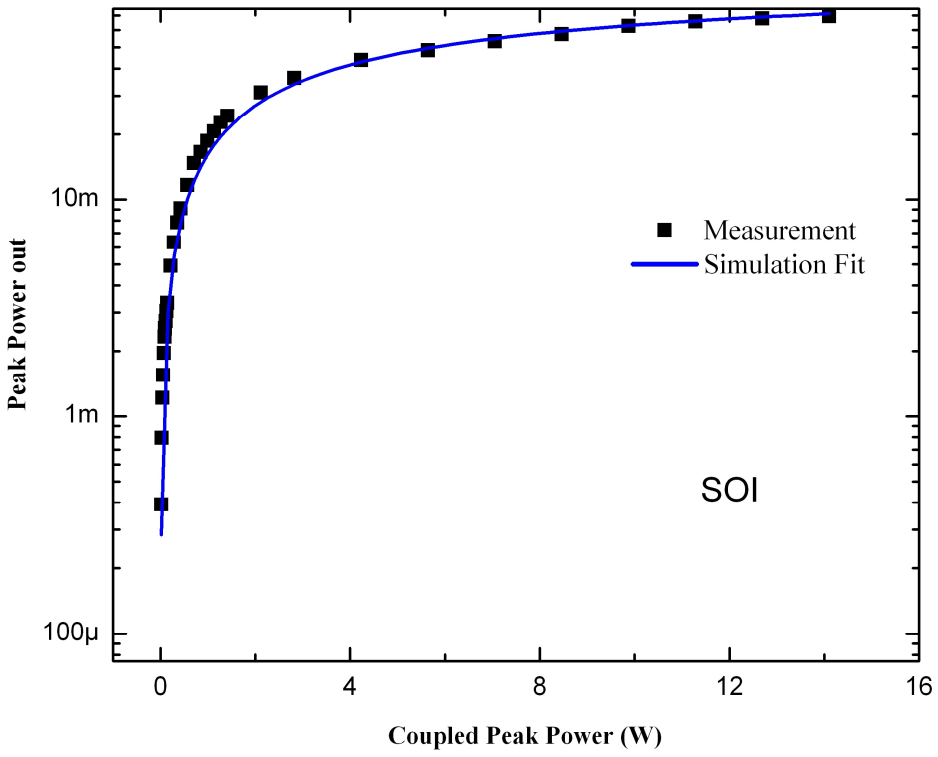

Figure 5.4 Output power (black squares) as function of coupled input power for SOI waveguide. The blue line indicates the fit measured data based on solving the nonlinear equations.

Similar measurements are performed on a SOI waveguide to extract the nonlinear parameters. The insertion loss at low powers is measured to be 33 dB with a transmission loss of 13.5 dB/cm. From the fits to the measurements shown in Figure 5.4, the two photon absorption coefficient and free carrier absorption are estimated to be 1.0 ± 0.1 cm/GW and 1.45 $\cdot 10^{-17}$ cm^2. These values are consistent with measurements reported in crystalline silicon [46, 47]. It can be noted from the measurements that the transmission through SOI waveguides begins to saturate at 4 W peak power coupled in the waveguides which yields a free carrier density of $2.8 \cdot 10^{16}$ cm^{-3}. In contrast to a-Si:H, it is determined that the saturation in the output is dependent more on the two-photon absorption (TPA) effect than from free-carrier absorption (FCA), since not enough carriers are generated in SOI waveguides in order for FCA to become considerable (owing to the considerably smaller free-carrier absorption coefficient). Consequently, on comparing the simulation fit parameters between a-Si:H and SOI waveguides, there is a significant enhancement of the nonlinear absorption in hydrogenated amorphous silicon over crystalline silicon. This could enable high performance all-optical or electro-optic modulators with the material [60].

5.4 Nonlinear Refraction Characterization

The nonlinear refractive index n_2 was determined by modeling the measured spectral broadening due to self-phase modulation (SPM) of the pulses in the waveguides. The measured transmission spectra and the simulation of the spectral broadening of the pulses through the a-Si:H waveguides for different coupled powers is shown in Figure 5.5. It is seen that there is an increase in the spectral broadening along with induced phase shifts

with increasing coupled powers. A nonlinear phase shift of 3.5π is obtained at 4.1 W coupled input power. It was observed through simulations that TPA plays a role in limiting the maximum achievable phase shift. It is known that TPA reduces the induced phase shift while leaving the pulse spectrum symmetric while FCA results in an asymmetric pulse spectrum [51]. From the measured spectral data, it can be observed that the symmetric pulse spectrum indicates that TPA is the more dominant effect as compared to FCA. The modeling fits closely match the measured spectrum. From the modeling, the nonlinear refractive index of a-Si:H is estimated to be $(4.2 \pm 1) \cdot 10^{-13}$ cm^2/W. We should note that the enhanced nonlinear Kerr index of a-Si:H observed here is in agreement with the enhancement of the DC Kerr effect of a-Si:H previously observed [40]. Based on the measurement of the Kerr index, the nonlinear coefficient in a-Si:H waveguides is (2000 ± 500) $(W \cdot m)^{-1}$.

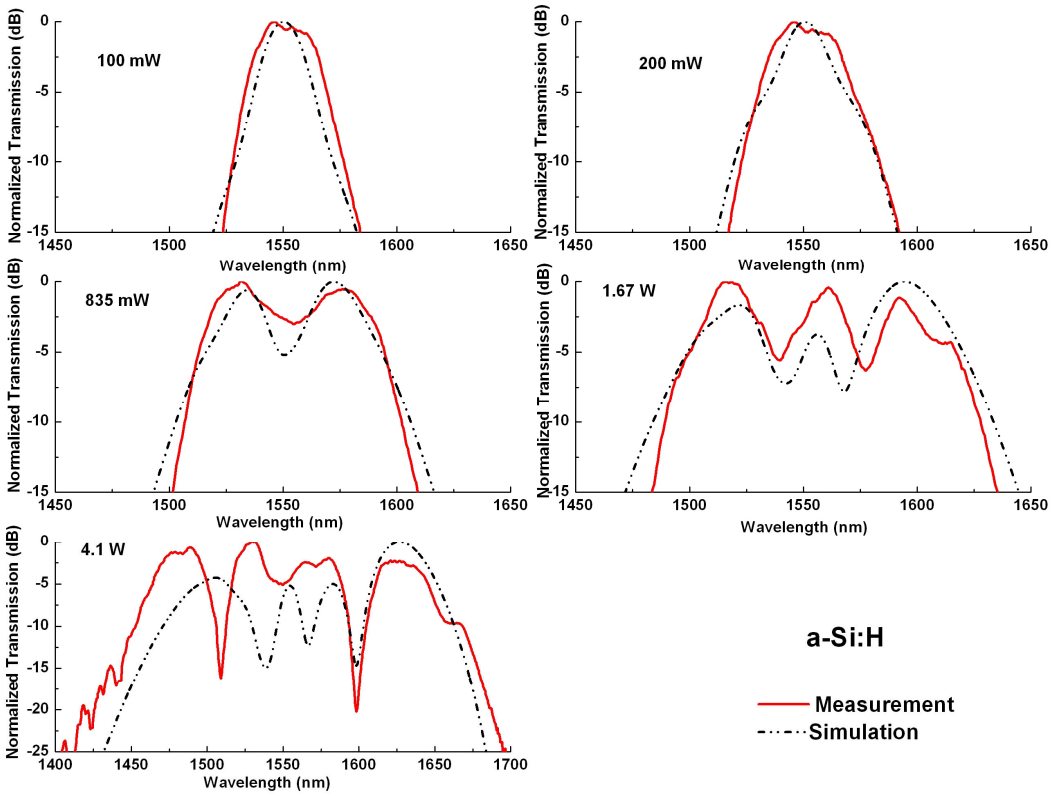

Figure 5.5 Measured spectral broadening in a-Si:H waveguides at different coupled powers due to self phase modulation and modeling fits based on solving nonlinear Schrödinger equations.

Spectral broadening was also observed in SOI waveguides as shown in Figure 5.6. A nonlinear phase shift of 1.5π is obtained at 1.4 W coupled power. Based on the simulation fits to the measured spectrum, the nonlinear refractive index n_2 is inferred to be $(8 \pm 2) \cdot 10^{-14}$ cm^2/W which is consistent with other values reported in crystalline silicon [46, 47, 50]. The measured nonlinear Kerr index corresponds to a nonlinear coefficient γ in crystalline silicon of (380 ± 100) $(W \cdot m)^{-1}$. Consequently, the nonlinear coefficient of a-Si:H waveguides is at least 5 times that in SOI. It should be noted here that the uncertainties in the reported values are based on measurements made on a number of different waveguides (> 10) on different chips and an uncertainty in the coupling coefficients of ± 3 dB.

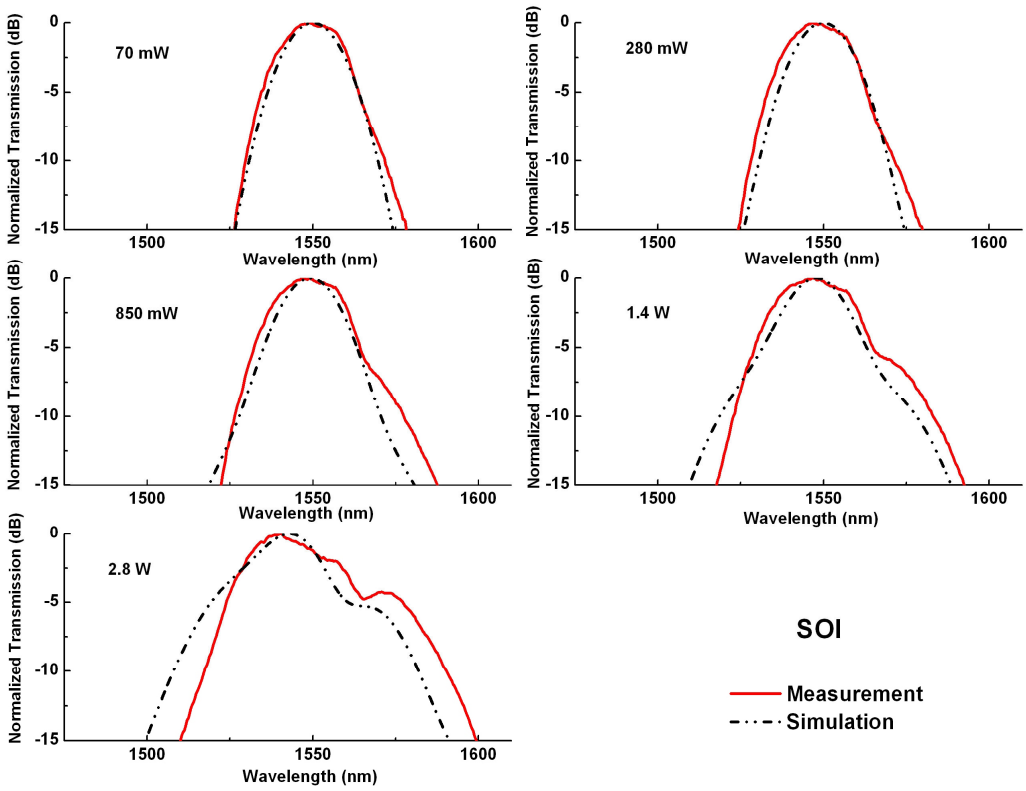

Figure 5.6 Measured spectral broadening in SOI waveguides at different coupled powers due to self phase modulation and modeling fits based on solving nonlinear Schrödinger equations.

5.5 Four-wave-mixing (FWM) in a-Si:H waveguides

To characterize FWM in a-Si:H waveguides, we employed an experimental set-up as shown in Figure 5.7. In this measurement, the pump and the signal were generated from two tunable CW lasers. The pump was amplified using an erbium-doped fiber amplifier (EDFA) and coupled with the signal using a 3-dB coupler. The pump signal after being amplified by the EDFA was filtered using a 1 nm wide band pass filter (BPF) centered around 1555.75 nm to suppress the amplified noise from the EDFA. The pump and the signal are then coupled into the a-Si:H waveguides using a tapered lens fiber. The output is collected using another pair of tapered lens fiber and observed on an optical spectrum analyzer (OSA). The a-Si:H waveguides used in this measurement have dimensions of 400 nm x 300 nm.

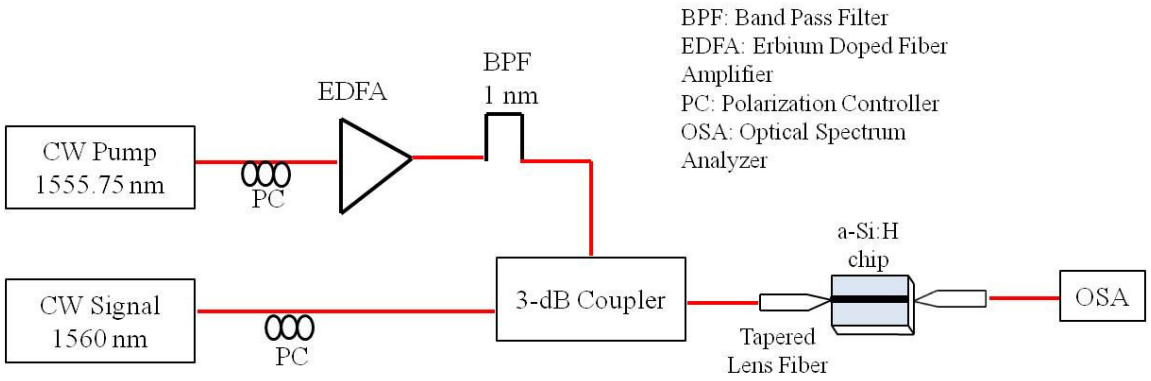

Figure 5.7 Experimental set-up to characterize four-wave mixing in a-Si:H waveguides.

Figure 5.8 shows the output spectrum observed on the OSA. With a pump centered at 1555.75 nm and a signal at 1560 nm, an idler is observed at 1551.5 nm. With a signal centered at 1550 nm, an idler is observed at 1561.5 nm. The idler frequency is observed at $\omega_i = 2\omega_p - \omega_s$, where ω_p and ω_s correspond to the pump and signal frequencies respectively.

The coupled pump power into the a-Si:H waveguides is calculated to be 16 mW. The conversion efficiency (G) of the idler frequency can be calculated using Equation 5.4.

$$G = \frac{P_{idler}^{out}}{P_{signal}^{in}} \tag{5.4}$$

Based on the measured spectrum in Figure 5.8, the conversion efficiency of the idler frequency is estimated to be ~ -35 dB. The conversion efficiency can be improved by operating at or near the anomalous dispersion region of the material [61]. It can also be improved by tailoring the material band-gap to reduce the two-photon absorption coefficient as has been recently demonstrated [62].

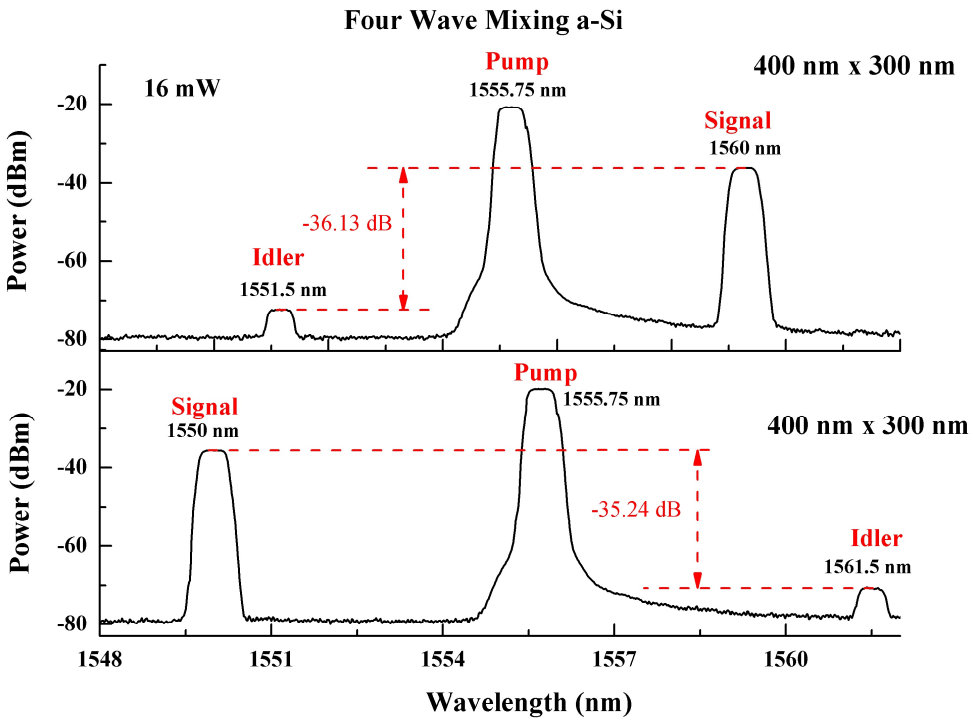

Figure 5.8 FWM output spectrum measured after a-Si:H waveguide with 16 mW pump power.

However, it is to be noted that due to the enhanced nonlinear coefficient in a-Si:H, FWM can be observed at relatively low pump powers as compared to crystalline silicon waveguides that have been demonstrated to require much higher pump powers [63]. It can be observed in Figure 5.9 that an idler frequency can be generated at pump powers as low as 3 mW.

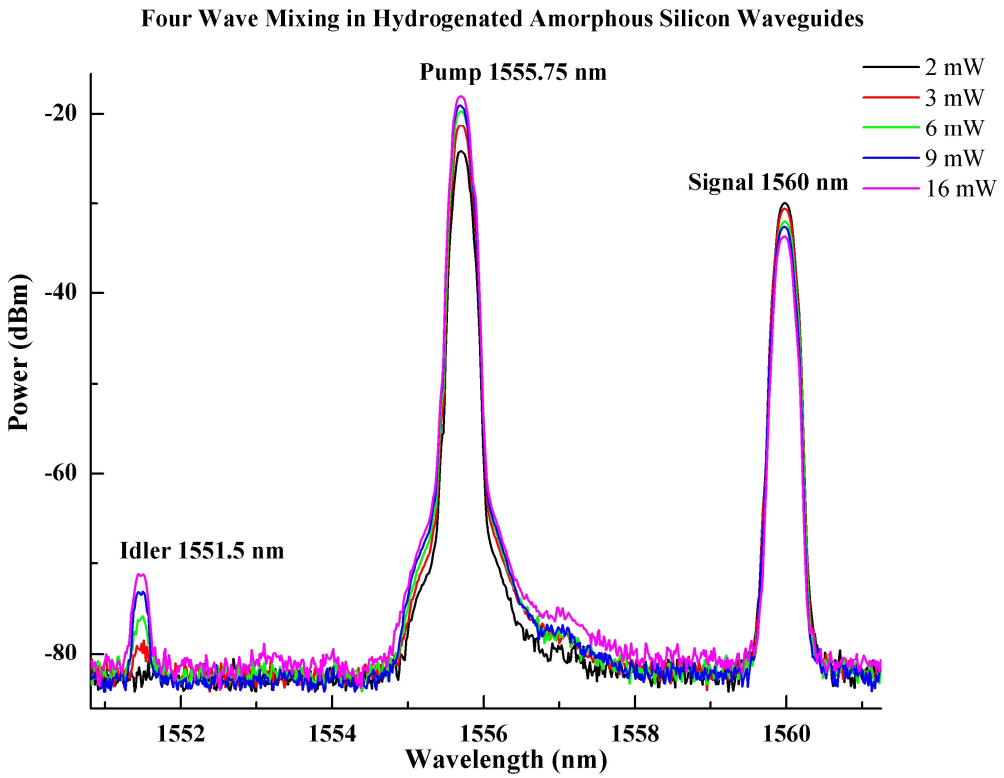

Figure 5.9 FWM in a-Si:H as function of pump power.

FWM can also be used to estimate the nonlinear Kerr index of a material. As observed in Figure 5.8, FWM produces sidebands whose amplitudes and frequencies depend on the nonlinear parameter γ. The power ratio of the pump and the idler frequencies is given according to Equation 5.5.

$$\frac{P_0}{P_1} = \frac{J_0^2(\phi_{\max}/2) + J_1^2(\phi_{\max}/2)}{J_1^2(\phi_{\max}/2) + J_2^2(\phi_{\max}/2)} \tag{5.5}$$

This power ratio can be computed from the frequency spectrum observed in Figure 5.9 and provides the phase shift $\phi_{\max}$. The phase shift $\phi_{\max}$ is then used to determine γ and the nonlinear index n_2 according to Equation 5.6.

$$\phi_{\max} = 2 \cdot \gamma \cdot P_{av} \cdot L_{eff} \tag{5.6}$$

$$L_{eff} = \left(1 - e^{-\alpha L}\right) / \alpha \tag{5.7}$$

In Equation 5.6, P_{av} is the average power of the signal launched into the waveguide and L_{eff} is the effective length of the waveguide that depends on the linear loss α of the waveguide according to Equation 5.7. The linear loss in the a-Si:H waveguide was measured to be ~ 6.5 dB/cm.

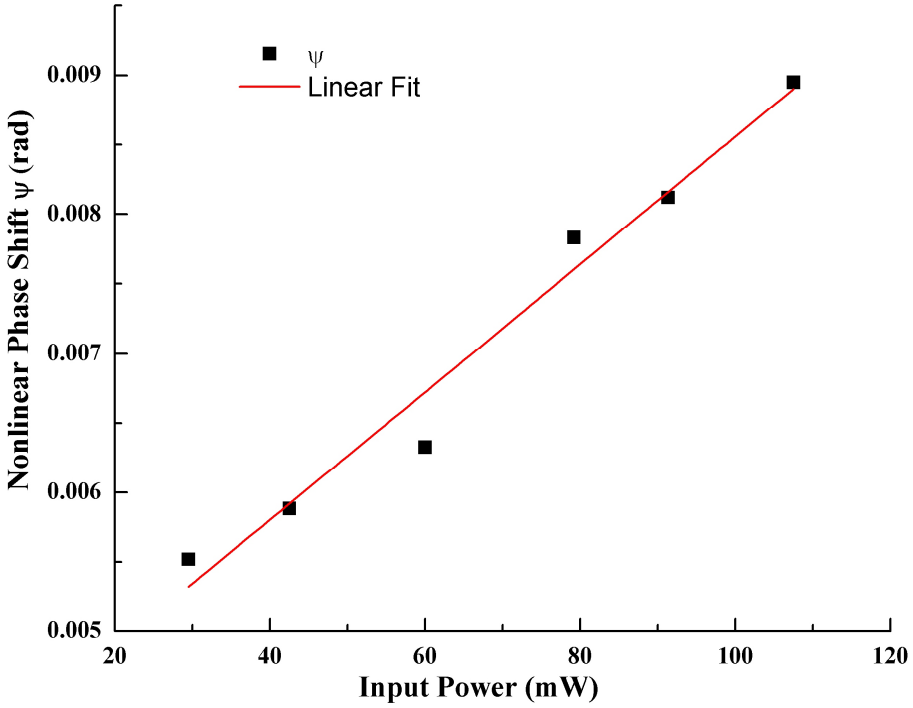

Figure 5.10 Linear change in phase of the idler frequency with increasing pump powers in a-Si:H waveguides.

Figure 5.10 shows the linear evolution of the phase with increasing pump powers. The nonlinear index estimated by plugging numbers in Equation 5.6 is $n_2 \sim 3.65 \cdot 10^{-17}$ m^2/W. It can be noted that this value in a-Si:H matches closely with the nonlinear index computed in section 5.4. It can therefore be concluded that a-Si:H waveguides exhibit an enhanced nonlinear coefficient as compared to crystalline silicon waveguides. A

comparison of the nonlinearities in a-Si:H and SOI waveguides is given in Table 5.1 below.

Table 5.1 Comparison of optical nonlinearities between a-Si:H and SOI waveguides.

Parameters	a-Si:H waveguide	SOI waveguide	Unit
Length	7	6	cm
Transmission Loss (α)	3.5	13.5	dB/cm
Effective Area (A_{eff})	0.085	0.085	μm^2
Free carrier lifetime (τ_c)	400	450	ps
Two-photon absorption (β)	4.1	1.05	cm/GW
Free-carrier absorption (σ)	$1.9 \cdot 10^{-16}$	$1.45 \cdot 10^{-17}$	cm^2
Kerr coefficient (n_2)	$4.2 \cdot 10^{-13}$	$8 \cdot 10^{-14}$	cm^2/W
Nonlinear coefficient γ	2003	381	$(W \cdot m)^{-1}$
Figure of Merit (FOM)	0.66	0.49	

Summary

In this chapter, we experimentally measure the optical nonlinearities in hydrogenated-amorphous silicon (a-Si:H) waveguides through the transmission of ultra-short pulses. The measured two-photon absorption coefficient β is 4.1 cm/GW and we obtain a 3.5π nonlinear phase shift at 4.1 W coupled input power corresponding to a nonlinear refractive index n_2 of $4.2 \cdot 10^{-13}$ cm^2/W. The measured nonlinear coefficient γ = 2003 $(W \cdot m)^{-1}$ is at least 5 times the value in crystalline silicon. The measured free carrier absorption coefficient $\sigma = 1.9 \cdot 10^{-16}$ cm^2 agrees with the values predicted from the Drude-Lorenz model. It is seen that a-Si:H exhibits enhanced nonlinear properties at 1550 nm and is a promising platform for nonlinear silicon photonics. We also demonstrate low-

power continuous wave four-wave-mixing in a-Si:H in the amorphous silicon waveguides. The value of the nonlinear index n_2 extracted from FWM matches the index value determined through modeling the nonlinear differential equations.

CHAPTER 6

GENERATION OF AMPLITUDE-SHIFT-KEYING SIGNALS USING SILICON RING RESONATORS

6.1 Modulation formats for on-chip communication

Recent innovations and breakthroughs in silicon photonics are paving the way for the realization of high speed on-chip optical interconnects. The transfer of information between components requires that data be superimposed on the optical carrier signal by electro-optic modulation. Numerous high performance silicon electro-optic modulators have been demonstrated which generate non-return-to-zero (NRZ) encoding at bit-rates as high as 40 Gbps [64, 65]. However, there are numerous other optical modulation formats which could yield improved performance of the optical links, such as better Signal/Noise ratio, reduced non-linearity, or even higher bit-rates [66]. Some recent examples of alternate encodings on a silicon photonic platform are the use of ring resonators to convert non-return-to-zero (NRZ) to pseudo-return-to-zero (PRZ) in order to aid clock recovery and the generation of return-to-zero-differential-phase-shift-keying (RZ-DPSK) signals with improved chirp [67, 68].

Here, a scheme for generating amplitude-shift-keying (ASK) format in order to significantly increase the bit-rate of on-chip optical links is proposed. In an ASK signal, multiple logic levels are used to encode information, which effectively increases the bit-rate of an optical link [69]. In this scheme, three amplitude level signals are generated using a pair of symmetric microring resonators arranged in parallel in a Mach-Zehnder configuration as seen in Figure 6.1. The device works by splitting the input light

into two separate paths with a 3-dB coupler. When the light is on resonance with the rings, it is coupled to the drop ports where it constructively interferes at the output port. If one ring resonator is shifted off-resonance, the output of the system is halved because only half of the light transfers to the output port as illustrated in Figure 6.1 (b), and if both ring resonators are shifted off-resonance, then there is no field at the output port, as shown in Figure 6.1 (c). Therefore, with two ring resonators it is possible to generate three states. So, in general N+1 amplitude levels can be realized by N ring resonators cascaded in parallel.

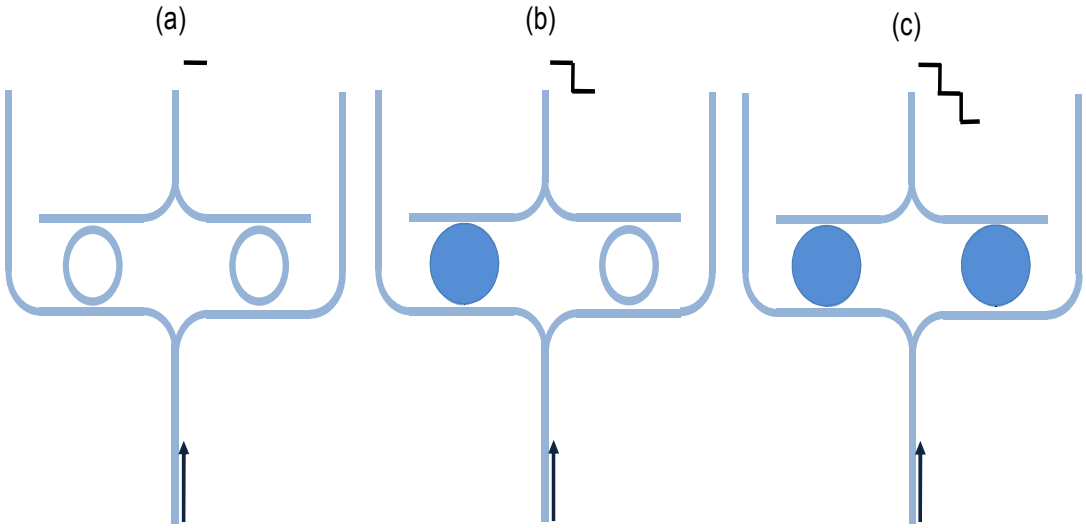

Figure 6.1 Principle of operation of the device is illustrated: (a) two unmodulated ring resonators result in amplitude level 1. (b) Modulating one ring (blue) resonator independently results in amplitude level 2 and (c) modulating both resonators results in amplitude level 3.

The operation of the structure can be understood by considering the transmission of an individual ring resonator to the drop port, which is given by coupled mode theory [70]

$$T_{drop} = \frac{e^{-2\gamma} \cdot \kappa_1^2 \cdot \kappa_2^2}{\left(1 - t_1 t_2 \cdot e^{-\gamma}\right)^2 + 4 t_1 t_2 \cdot e^{-\gamma} \sin^2[\theta]} \tag{6.1}$$

In Equation 6.1, $e^{-\gamma}$ is the field transmission per round in the ring, κ_1 and κ_2 are the coupling coefficients at add and drop ports respectively, $t_{1,2} = \sqrt{1-\kappa_{1,2}^2}$, and

$\theta = \pi \cdot n \cdot 2\pi R / \lambda$ is phase the mode accumulates in one round trip (n is the refractive index, λ is the resonant wavelength). Equation 6.1 has a peak value when $\theta = m2\pi$ and quickly drops off to zero for any other values (i.e. off-resonance) [70]. Therefore the overall transmission of our structure can be modeled by

$$T = \frac{\sum_{m=1}^{N} u \cdot T_{drop}^{m}}{N} \tag{6.2}$$

In Equation 6.2, N is the total number of ring resonators in parallel and u takes on a value of $\{1 \mid 0\}$ when the individual rings are $\{\text{on} \mid \text{off}\}$ resonance, respectively.

6.2 Demonstration of ASK Modulation using Thermo-Optic Tuning

As a proof of concept of the generation of amplitude-shift-keying optical signals using silicon ring resonators, here the structure shown in Figure 6.1 is tuned using a thermo-optic modulation scheme. The device is fabricated on 250 nm thick hydrogenated-amorphous silicon deposited using plasma enhanced chemical vapor deposition technique (PECVD) at 400ºC onto 3 microns of thermally grown oxide. The ring resonators are patterned using electron-beam lithography followed by an etch using an inductively coupled plasma (ICP) chlorine etching system. The process flow involved in the fabrication of the microrings structure is illustrated in Figure 6.2.

The ring resonator waveguides are 460 nm wide, have a diameter of 10 μm and are spaced 40 μm apart as seen in Figure 6.3 (a). The device is clad with 600 nm of PECVD silicon dioxide to protect the optical mode, but is thin enough to ensure efficient coupling of heat to the silicon waveguides [71]. The heat is supplied by Nickel-Chromium heaters that are patterned on top of the 600 nm oxide. The heaters are 2 μm wide and are defined

using standard optical lithography and lift-off processing of a sputtered nickel-chromium film, 80 nm thick. An optical microscope image of the device with heaters is shown in Figure 6.3(b).

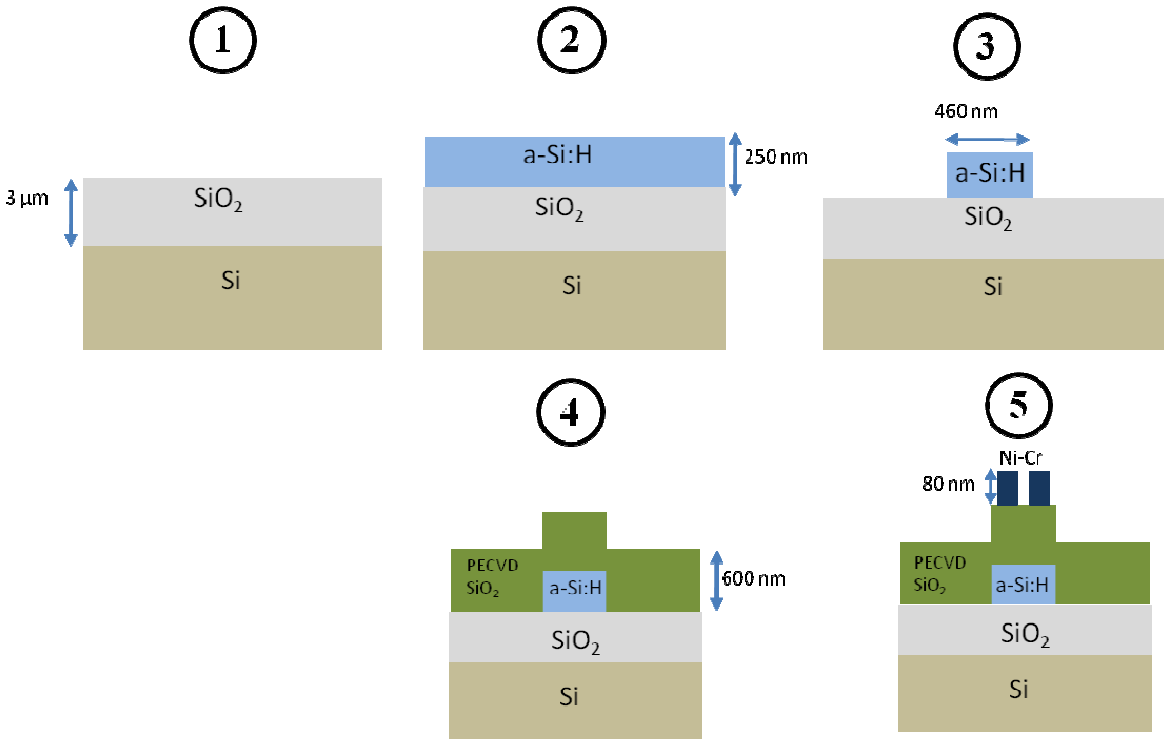

Figure 6.2 Process flow in the fabrication of a-Si:H microring resonators with resistive heaters. Step 1: 3 µm thick thermal oxide is grown on a silicon substrate. Step 2: 250 nm thick a-Si:H film is deposited using PECVD. Step 3: Waveguides are patterned on a-Si:H using e-beam lithography. Step 4: 600 nm thick PECVD SiO2 is deposited to protect the optical mode. Step 5: 80 nm thick Ni-Cr resistive heaters are patterned using optical lithography.

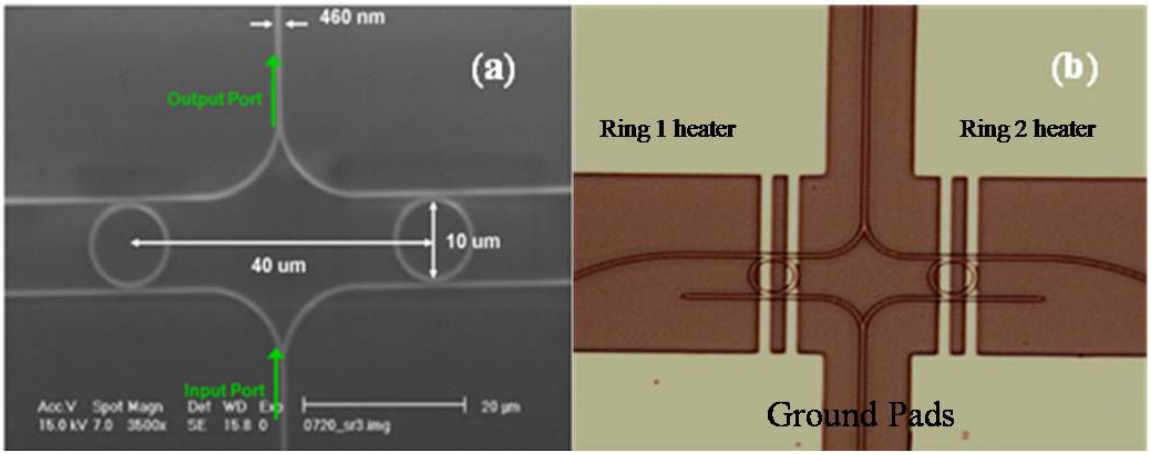

Figure 6.3 (a) SEM image of the fabricated device. (b) Optical microscope image of the device with heaters.

The thermo-optic generation of ASK signals is achieved using the experimental setup shown in Figure 6.4. Heat is applied to each ring resonator, which effectively shifts its resonance. The thermo-optic co-efficient in hydrogenated-amorphous silicon at room temperature is measured to be $\partial n/\partial T = 2.4\times10^{-4} K^{-1}$ [37]. The change in amplitude of the optical field at the drop port due to the applied heat can be modeled based on Equation 6.2.

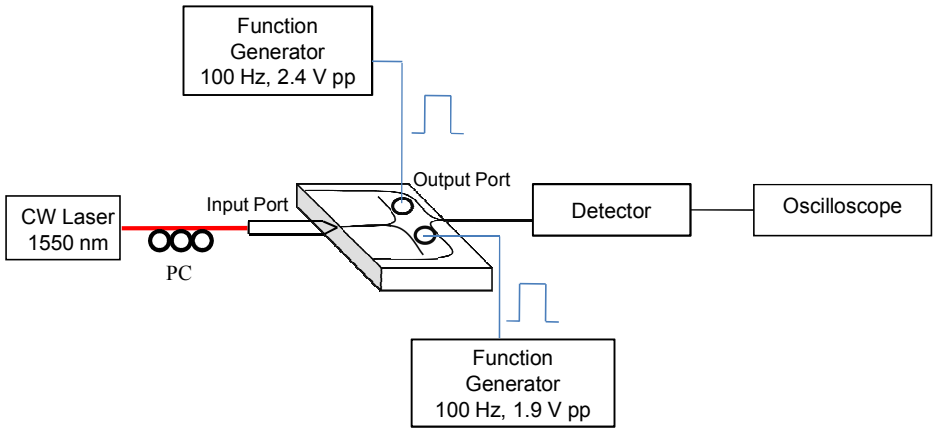

Figure 6.4 Experimental set-up to measure simultaneous thermo-optic switching of two ring resonators. The two rings are switched individually using the thermo-optic effect by applying square wave electrical pulses at 100 Hz to produce modulated signal observed on an oscilloscope.

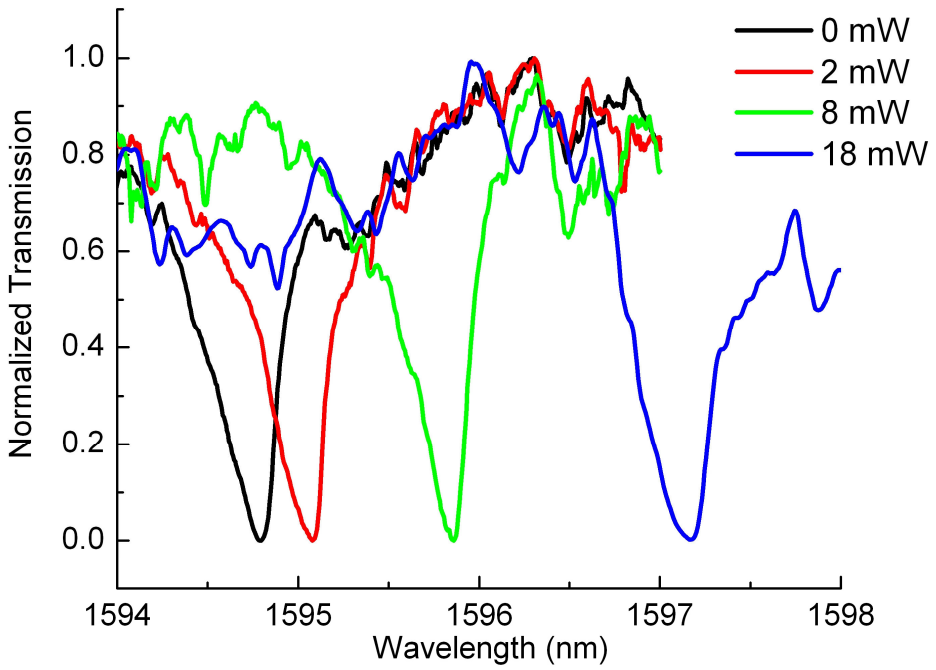

Figure 6.5 Thermal tuning of resonator wavelengths is achieved by applying heat to the individual rings.

The measured shift in resonance of one of the ring resonators is shown in Figure 6.5 where a shift of 0.14 nm/mW is observed due to the applied electric power. By driving this single resonator at 100 Hz with a 2 V_{pp} electronic signal, it is seen in Figure 6.6 (a) that two amplitude levels are generated from the structure. The high level is where both ring resonators are in resonance with the input light and the ~ 0.5 level is generated when one ring resonator is shifted off-resonance due to the application of heat.

In order to generate three amplitude levels, both ring resonators are modulated simultaneously. As seen in Figure 6.6 (b) when both rings are on resonance, a "1" is generated, when one is off-resonance, a "0" is generated and lastly when both are off resonance, a "-1" is generated. Note that "-1" and "1" can be reversed if the wavelength of the light is such that it is off-resonance when no heat is applied. Therefore, it is observed that with two ring resonators it is possible to generate up to three different

amplitude levels on a single optical carrier. This scheme can simply be scaled up to more logic levels by adding additional ring resonators and splitters to the system.

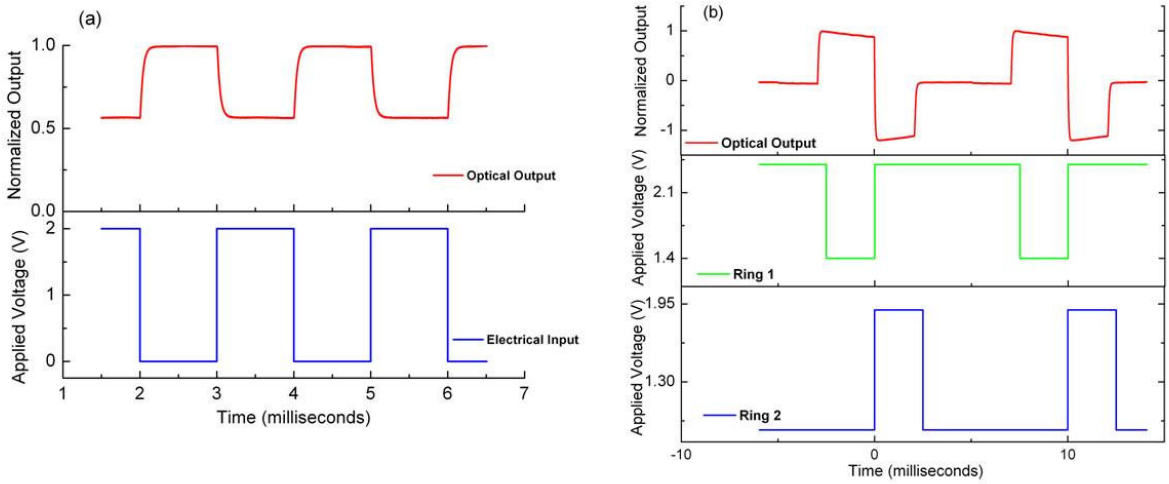

Figure 6.6 (a) Temporal response of the system due to modulation of one resonator. The other resonator is always on resonance. (b). Modulating both resonators generates three amplitude levels on a single carrier.

6.3 ASK Modulation Using All-Optical Switching

In order to demonstrate the operation of the ASK modulation scheme at ~ Gbps data rates, an all-optical modulation scheme similar to those previously demonstrated in section 5.2 is utilized. A detailed schematic of the pump-probe all-optical modulation set-up is shown in Figure 6.7.

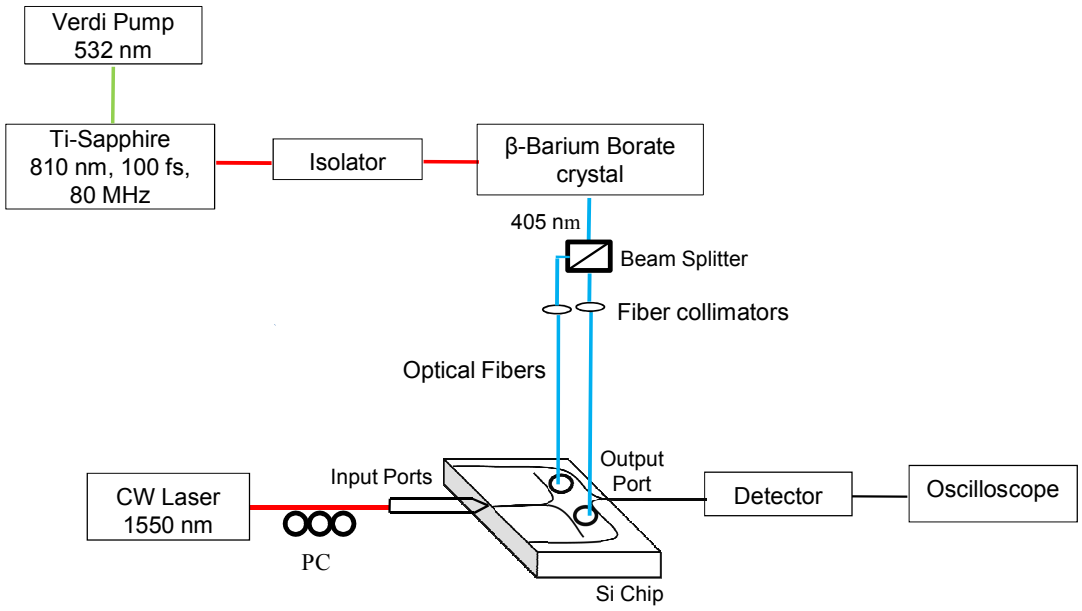

Figure 6.7 Measurement set-up to generate all-optically modulated ASK signals. Two pump pulses are delayed by 200 ps to enable the demonstration of three switching levels. PC: Polarization Controller.

The pump source is a mode-locked Ti-sapphire laser generating 100 fs pulses centered at 810 nm with an 80 MHz repetition rate. A β-barium borate crystal is used to generate second harmonic pulses centered at 405 nm. A beam-splitter and a pair of fiber collimators are used to couple the 405 nm pulses into a pair of optical fibers. The second harmonic pulses are absorbed by the silicon waveguides and generate photo-excited carriers. These photo-excited carriers change the effective index of the ring resonators, shifting the resonances. It is to be noted that an identical crystalline silicon device was used for this experiment. The probe signal obtained from a tunable continuous wave laser using a tapered lens fiber passes through a polarization controller and is coupled on and off the silicon chip using adiabatic inverse tapers [55]. The output from the chip is detected using a 20 GHz photodetector and sampling oscilloscope.

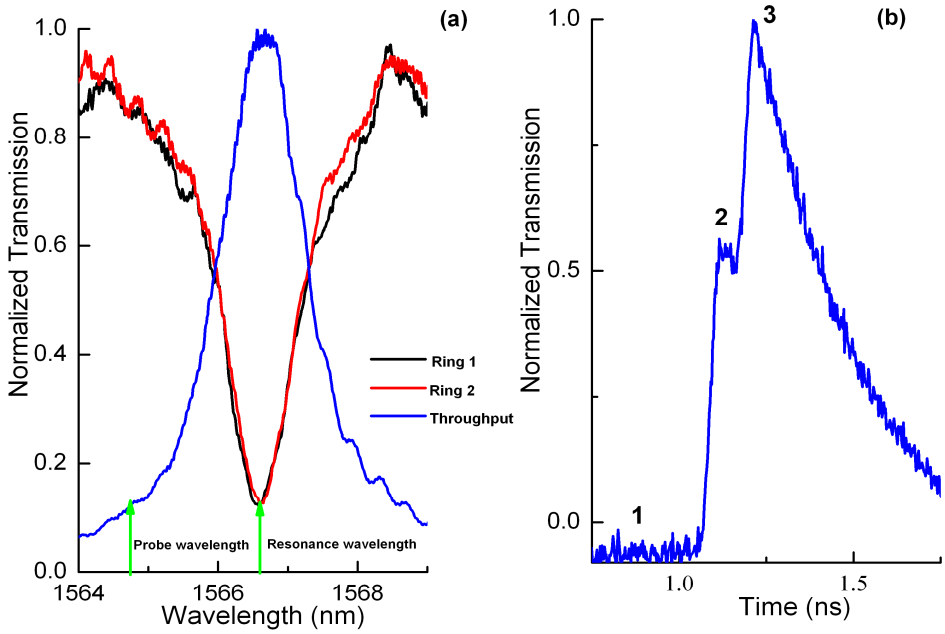

Figure 6.8 (a) The resonances of the individual resonators and through port of the entire system. The probe wavelength used is slightly blue-shifted off-resonance. (b) Three level temporal response of the system by switching two ring resonators with a 200 ps delay.

To achieve the modulation, the system is initially operated with the probe signal slightly off-resonance as indicated in Figure 6.8 (a). The system does not transmit in this state which corresponds to the first logic level of the system. The system is modulated to the next logic level by switching one ring resonator on resonance using a pump pulse, which causes the transmission of the system to rise to half its maximum, corresponding to the second logic level. However, before the carriers can completely recombine, the second ring resonator is switched on-resonance after a delay of ~200 picoseconds. This results in the maximum transmission of the system corresponding to the third logic level as indicated in Figure 6.8 (b). The switching speed of the system is limited by the free-carrier recombination lifetime which can be improved by incorporating p-i-n diodes to sweep out the carriers, thereby improving the data-rate of the overall system [72].

In this chapter, generation of three-level amplitude-shift-keying signals using a pair of symmetric silicon microring resonators arranged in parallel is demonstrated by independently modulating the individual resonators. The proposed scheme can be extended to any number of logic levels, which effectively increases the data rate of an optical link using slower modulators. This enables an increase in the spectral efficiency of single optical carrier in an on-chip optical communication link. Thermo-optic tuning and ultrafast all-optical modulation schemes are utilized to generate the ASK signals on a silicon photonic chip. Drawbacks of ASK are the number of levels that can be utilized is limited by the signal/noise ratio of the optical link and by the discrimination of the amplitude levels at the receiver. However, recent implementation of on-chip transceivers and low loss waveguides enables the integration of the necessary circuitry with sufficient S/N for at least a three-level ASK format [64, 73, 74].

CHAPTER 7

CONCLUSION AND FUTURE WORK

7.1 Summary

This thesis has sought to characterize hydrogenated-amorphous silicon as a high performance platform to enable on-chip optical interconnects in multi-core processors. The research described in this thesis involved fabrication, measurement and characterization of a-Si:H as a material platform.

Firstly, I demonstrated a low-loss hydrogenated-amorphous silicon (a-Si:H) platform, along with high quality factor micro-cavity devices that can enable the realization of on-chip wavelength-division multiplexing schemes. The a-Si:H was deposited using plasma enhanced chemical vapor deposition (PECVD) and devices fabricated using electron-beam lithography followed by a reactive ion etch.

Next, I demonstrated broadband, all-optical modulation in the low loss a-Si:H waveguides using a pump-probe scheme. Significant modulation is observed in a-Si:H waveguides without the need for cavity interference effects in stark contrast to an identical crystalline silicon waveguide. The enhanced modulation is attributed to the significantly larger free-carrier absorption effect of a-Si:H. The modulation time is measured to be only $\tau_c \sim 400$ ps, which is comparable to recombination rate measured in sub-micron crystalline silicon waveguides illustrating the strong dominance of surface recombination in similar sized a-Si:H waveguides.

Further, I comprehensively characterized the optical nonlinearities in a-Si:H waveguides and compared the properties with that of crystalline silicon waveguides. The nonlinearities characterized were two-photon absorption, nonlinear refractive index, and

free-carrier absorption co-efficient. The nonlinearities in a-Si:H are measured to be 5 times that in crystalline silicon waveguides. The nonlinearities were characterized by solving a set of nonlinear differential equations using a split-step Fourier Technique. Based on the enhanced nonlinearities, I also demonstrated low-power continuous wave four-wave mixing in a-Si:H waveguides and measured the nonlinearities based on the observed spectrum.

Finally, I demonstrated a novel data encoding scheme using a system of ring resonators in a-Si:H to increase the spectral efficiency of an interconnect link. Thermo-optic modulation of a-Si:H waveguides is utilized to demonstrate a proof-of-concept three-level data encoding scheme. A system of two ring resonators arranged in parallel can lead to three amplitude levels. The scheme can be extended by using N ring resonators to generate a N+1 level amplitude scheme. A high-speed data modulation is also demonstrated using all-optical modulation of a pair of symmetric ring resonators in crystalline silicon waveguides.

7.2 Future Work

Compact, high-speed electro-optic modulators have been demonstrated in crystalline and polycrystalline silicon. However, there has been no demonstration of an electro-optic modulator in a-Si:H. The enhanced free-carrier absorption coefficient can enable a compact, broadband, low-power electro-optic modulator in a-Si:H. The free-carrier lifetime in a-Si:H waveguides can be reduced by incorporating a p-i-n diode structure to sweep out the charge carriers. A p-i-n diode structure in a-Si:H was designed to enable the demonstration of an electro-optic modulator in a-Si:H. The schematic structure consists of an intrinsic a-si:H waveguide sandwiched between n-doped and p-doped

regions as shown in Figure 7.1. Free-carrier lifetime simulations were carried out using Atlas-Silvaco by applying a reverse bias across the p-i-n structure. The results of the simulation are shown in Figure 7.2.

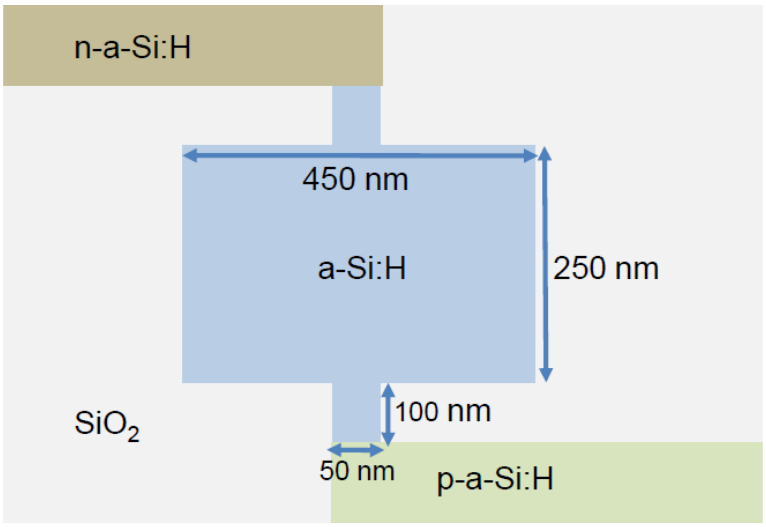

Figure 7.1 Schematic layout of a p-i-n diode based a-Si:H modulator. The p and n doped regions are 100 nm in thickness.

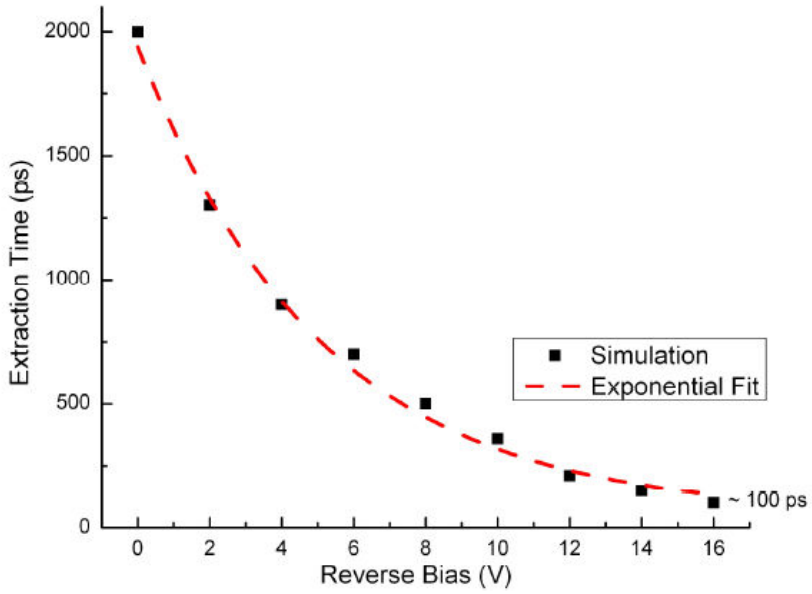

Figure 7.2 Application of a reverse bias across the p-i-n junction results in a decrease of the free carrier lifetime of the carriers in a-Si:H. An exponential fit results in a carrier lifetime of ~ 100 ps at 16 V applied reverse bias.

Application of a reverse-bias across the p-i-n junction results in the decrease of free-carrier lifetime of the carriers in a-Si:H waveguides. The free-carrier lifetime can be reduced to ~ 100 ps with a 16 V applied reverse bias across the p-n junction. The free-carrier lifetime is limited by the low carrier mobilities in a-Si:H. The carrier mobilities are estimated to be: $\mu_e \sim 2.0$ cm^2/V·s and $\mu_h \sim 0.4$ cm^2/V·s. The fabrication of an electro-optic modulator in a-Si:H is a challenge due to the amorphous nature of the material combined with low carrier mobility and the low temperature deposition technique. The low thermal budget (200– 400°C) during deposition precludes ion-implantation followed by subsequent anneal as a means to establish a p-n junction. Instead, in-situ doping is the preferred technique to fabricate a p-n junction. Based on the simulation shown in Figure 7.1 and Figure 7.2, it should be possible to demonstrate an electro-optic modulator in a-Si:H.

The amount of hydrogen-content in the a-Si:H films is also known to influence the properties of devices including film density. Recently, it has been demonstrated that hydrogen content in the deposited films can be altered by annealing the films [75]. It was observed that by annealing the fabricated devices in a nitrogen ambience, the propagation losses in the devices increased with increasing temperature. Propagation loss increased with an increase in the annealing temperature and measurements were not possible upon annealing beyond 400 °C as shown in Figure 7.3 [75]. The increase in propagation losses is attributed to the breaking of Si-H bonds resulting in desorption of H from the Si network. This is an important property to consider in a-Si:H based devices. It would be useful to study the nonlinear properties in a-Si:H films post-annealing at different

temperatures. A Fourier Transform Infrared Spectroscopy (FTIR) was performed on two different a-Si:H films as shown in Figure 7.4.

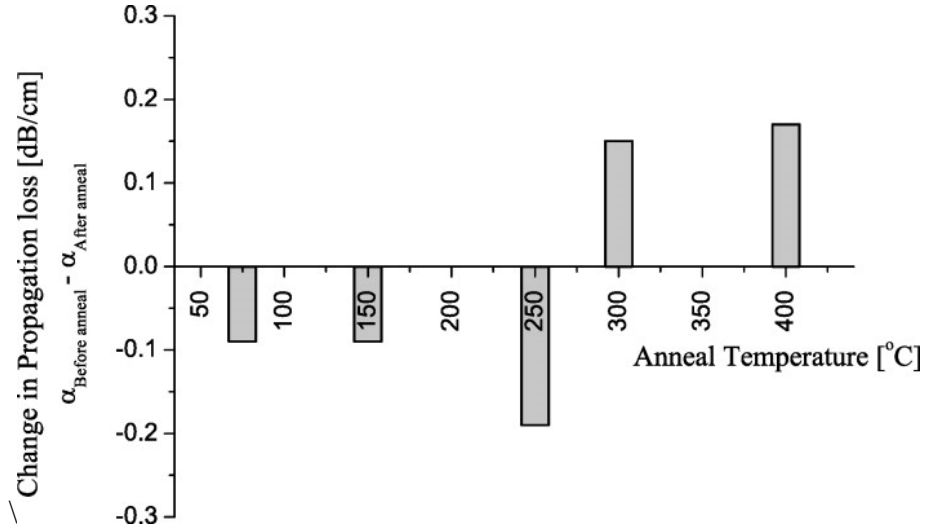

Figure 7.3 Change in propagation loss in the a-S:H films post-annealing in nitrogen ambience **[75]**.

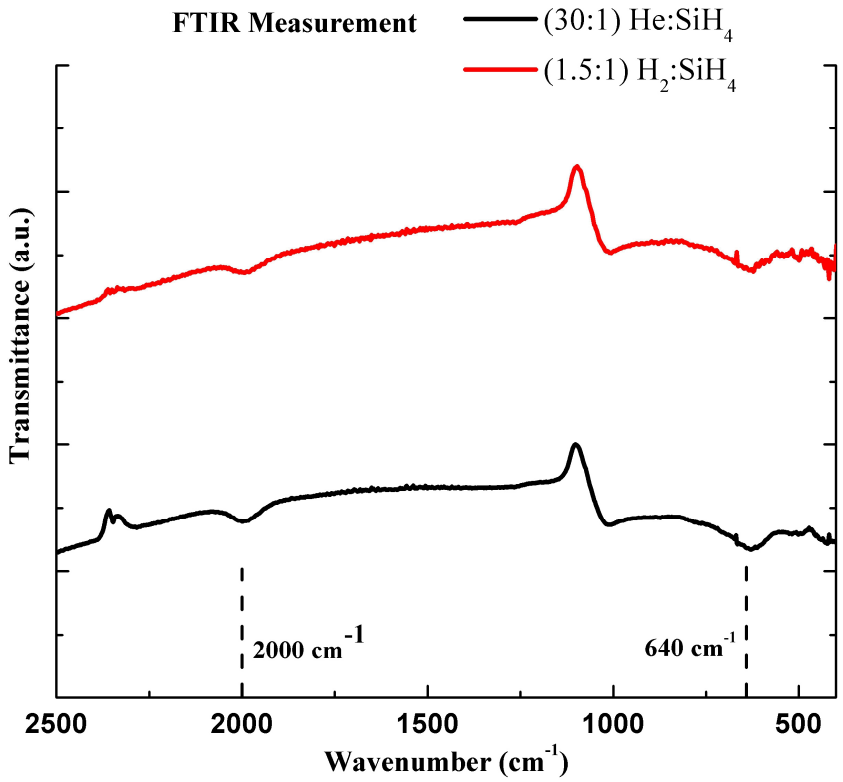

Figure 7.4 Fourier Transform Infrared Spectroscopy (FTIR) measurements on two different a-Si:H samples show Si-H bonds at 640 cm^{-1} and 2000 cm^{-1}.

In an initial study, the FTIR was performed on two different films with a $He:SiH_4$ gas ratio of 30:1 and $H_2:SiH_4$ gas ratio of 1.5:1. The deposition parameters of the two films are given in table 7.1 below.

Table 7.1 PECVD deposition parameters for a-Si:H sample 1

He:SiH4 ratio	30:1
Substrate Temperature	400 C
RF Power	300 W
Pressure	3 Torr

Table 7.2 PECVD deposition parameters for a-Si:H sample 2

H2:SiH4 ratio	1.5:1
Substrate Temperature	320 C
RF Power	3 W
Pressure	500 mTorr

The observations from the spectroscopic measurements show the existence of Si-H phonon mode bands at 640 cm^{-1} and at 2000 cm^{-1}. The actual H_2 content in the individual films could not be measured due to the lack of the standard wafer. The nonlinearities measured in this thesis are based on a sample deposited using parameters shown in Table 7.1. However, the variation in the nonlinear properties with variation in H_2 content in a-Si:H films is an important study that needs to be performed to thoroughly establish the nonlinear properties in a-Si:H films.

APPENDIX I

The nonlinear properties of a-Si:H and SOI waveguides were characterized based on modeling the measured parameters by solving the nonlinear differential equations given by Equations 5.1 and 5.2. The equations were solved using a split-step Fourier method described in Section 3.4.2. A computer program written in FORTRAN® to solve the equations is given below.

```
!*******************************************************************************
PROGRAM nlse
IMPLICIT NONE
REAL, PARAMETER :: pi = 3.1415926536, c = 2.99792458e8, hbar = 1.05459e-34,
h=6.626068e-34
COMPLEX, ALLOCATABLE, DIMENSION(:) :: uz,uzstart
REAL, ALLOCATABLE, DIMENSION(:) :: Nc,aFCA,nFCD
REAL, ALLOCATABLE,DIMENSION(:) :: InPowers, OutPowers

REAL :: nfun,ugh
REAL :: totaltime,dt,L,dz,lambda,alpha,Aeff,n2,beta
REAL :: sigFCA,kFCD
REAL :: RepetitionRate,PulseWidth
REAL :: InputPowerStart,InputPowerEnd,NumberPowers,dPower
REAL :: IpCouplingEff, OpCouplingEff
COMPLEX :: ci
INTEGER :: i,j,M,N,grad,nord,z

REAL :: k1,k2,k3,k4

REAL :: gamma, beta_tpa,f

INTEGER :: TotalTimePoints,StartTime,EndTime,Number
INTEGER :: TotalZPoints

REAL, ALLOCATABLE, DIMENSION(:) :: t
REAL :: power,energy, ppeak, powerin, powerout

ci = cmplx(0.,1.)

100 format(9999E15.6)
```

```
!************************** Defining Input Parameters ************************************

OPEN(UNIT=15,file = 'inpdata.txt',status = 'OLD')

read(15,*) totaltime,dt,L,dz,lambda
print*,  totaltime,dt,L,dz,lambda
read(15,*) alpha,Aeff,n2,beta
print*,alpha,Aeff,n2,beta
read(15,*) sigFCA,kFCD
print*, sigFCA,kFCD
read(15,*) RepetitionRate,PulseWidth
print*,RepetitionRate,PulseWidth
read(15,*) InputPowerStart,InputPowerEnd,Number
print*,InputPowerStart,InputPowerEnd,Number
read(15,*) IpCouplingEff,OpCouplingEff
print*,IpCouplingEff,OpCouplingEff
CLOSE(15)

!*****************************************************************************************

f=c/lambda

gamma=2*pi*n2/(lambda*Aeff)
beta_tpa=beta/(2*Aeff)
print*,'absorption (cm-1)',alpha*1.e-2
print*,'Gamma ',gamma
print*,'Beta TPA ', beta, beta_tpa
TotalTimePoints=totaltime/dt
StartTime=-TotalTimePoints/2
EndTime=TotalTimePoints/2

PRINT*,'Total Time, dt(s), Number of Points',totaltime,dt,TotalTimePoints
PRINT*,'Start Time Index, End Time Index',StartTime,EndTime

ALLOCATE(t(StartTime:EndTime))
do j = StartTime,EndTime
  t(j) = j*dt
enddo

TotalZPoints=L/dz
PRINT*,'Length(m), dz(m), TotalZPoints',L,dz,TotalZPoints

ALLOCATE(uzstart(StartTime:EndTime))
ALLOCATE(uz(StartTime:EndTime))
ALLOCATE(Nc(StartTime:EndTime))
ALLOCATE(aFCA(StartTime:EndTime))
```

```
ALLOCATE(nFCD(StartTime:EndTime))

dPower = (InputPowerEnd-InputPowerStart)/Number

ALLOCATE(InPowers(1:Number+1),OutPowers(1:Number +1))

do i=1,(Number+1)
! Loop through all of powers
 power=InputPowerStart+dPower*(i-1)
 powerin=power*IpCouplingEff
 energy=powerin/RepetitionRate
 ppeak = energy/(dt*sum(exp(-t**2/(PulseWidth*0.6006)**2)))
 PRINT*,'AveragePower(mW) Peak Power(W)',power/1e-3,ppeak
 InPowers(i)=power/1e-3

 uz=0
 uzstart=0
 Nc=0
 uz(:)=sqrt(ppeak)*exp(-0.5*(t**2/(PulseWidth*0.6006)**2))
 PRINT*,'Start:Peak Power ',uz(0)**2
 uzstart=uz

aFCA=0
nFCD=0
Nc=0

!******************** Solving the Differential Equations ********************************

 ! MAIN z Integration
 do z=1,TotalZPoints
          uz(:)=uz(:)+dz*(-alpha/2+(ci*gamma-beta_tpa)*abs(uz(:))**2-
(ci*(2*pi/lambda)*kFCD*Nc)-(0.5*sigFCA*Nc))*uz(:)
          Nc(:)=0
          do j=(StartTime),(EndTime)
             k1=dt*((cabs(uz(j))**2)**2)/(Aeff**2)
          k1=k1*beta/(2*h*f)
             k2=dt*((cabs(uz(j))**2)**2)/(Aeff**2)+dt*((cabs(uz(j+1))**2)**2)/(Aeff**2)
             k2=k2/2
             k2=k2*beta/(2*h*f)
             k3=k2
             k4=dt*((cabs(uz(j+1))**2)**2)/(Aeff**2)
             k4=k4*beta/(2*h*f)
          Nc(j)=Nc(j-1)+(k1+2*k2+2*k3+k4)/6
          !k1=(cabs(uz(j))**2)/(Aeff)
             !ugh=dt*(cabs(uzstart(j))**2)/(Aeff)
             !ugh=ugh*(cabs(uzstart(j))**2)/(Aeff)
          !ugh=ugh*beta
```

```
          !ugh=ugh/(2*h*f)
             !Nc(j)=Nc(j-1)+ugh
           enddo
           !Nc=(beta/(2*h*f))*Nc
        if (z==1) then
OPEN(UNIT=1,file='nc',status='unknown')
DO j=StartTime,EndTime
WRITE(1,100) t(j),Nc(j)
ENDDO
CLOSE(1)

           endif
           aFCA=0.5*sigFCA*Nc
           nFCD=ci*(2*pi/lambda)*kFCD*Nc
           !nFCD=1000
        !aFCA=0
 enddo
 energy=0
 do z=StartTime,EndTime
   energy=energy+dt*abs(uz(z))**2
 enddo
 power=energy*RepetitionRate
 powerout=power*OpCouplingEff
 OutPowers(i)=powerout/1e-6

PRINT*,'End Average and Peak Power ',OutPowers(i),abs(uz(0))**2
enddo

!*******************************************************************************

do i=1,(Number+1)
  PRINT*,InPowers(i),OutPowers(i)
enddo

OPEN(UNIT=1,file='u.txt',status='unknown')
DO i=StartTime,EndTime
WRITE(1,100) t(i),uzstart(i),uz(i)
!WRITE(1,100) uz(i)
ENDDO
CLOSE(1)
DEALLOCATE(t,uz,uzstart,Nc,aFCA,nFCD)
DEALLOCATE(InPowers,OutPowers)
END PROGRAM

function nfun(x,a)
     real, intent(in)::x
     real, intent(in)::a
```

```
    nfun = ((x**2)**2)/(a**2)
 end function nfun

!*************************************************************************************


!*************************inpdata.txt ***********************************************

5E-12 7.62E-15 5.4E-3 1.7E-6 1.58E-6  !Total Time, dt, Length, dz, Wavelength
165.0 0.85E-13 6E-18 0.860E-11 !alpha,Aeff,n2,beta
13.60E-21 3E-27 !sigFCA,kFCD
80E6 200E-15 !RepetitionRate,PulseWidth
0E-3 8E-3 25 !InputPowerStart,InputPowerEnd,Number
0.25 0.8  !IpCouplingEff, OpCouplingEff

!*************************************************************************************
```

REFERENCES

[1] Silicon Photonics, Intel Technology Journal, May 10 2004.

[2] International Technology Roadmap for Semiconductors, 2007.

[3] D. A. B. Miller, "Optical Interconnects to electronic chips," Appl. Optics **49**, F59-F70 (2010).

[4] M. Haurylau, G. Chen, H. Chen, J. Zhang, N. A. Nelson, D. H. Albonesi, E. G. Friedman, and P.M. Fauchet, "On-Chip Optical Interconnect Roadmap: Challenges and Critical Directions," IEEE Journal of Selected Topics in Quantum Electronics, **12**, 1699-1705 (2006).

[5] J. H. Collet, F. Caignet, F. Sellaye, and D. Litaize, "Performance constraints for On-chip Optical interconnects," IEEE J. Selected Topics in Quantum Electronics **9**, 425-432 (2003).

[6] L. Benini, and G. De. Micheli, "Networks on Chips: A new SOC paradigm," Computer **35**, 70-78 (2002).

[7] E. Salminen, A. Kulmala, and T. D. Hamalainen, "Survey of network-on-chip proposals," White Paper, OCP-IP, 1-13 (2008).

[8] R. Ho, K. W. Mai, and M. A. Horowitz, "The future of wires," Proc. IEEE **89**, 490-504 (2001).

[9] L. Li, N. Vijaykrishnan, M. Kandemir, and M. J. Irwin, "Adaptive error protection for energy efficiency," Proc. Intl. Conf. on Computer Aided Design (ICCAD'03), San Jose, CA, USA, 2-7 (2003).

[10] M. Petrecca, K. Bergman, L. P. Carloni, "Photonic networks-on-chip: Opportunities and Challenges," in IEEE International Symposium on Circuits and Systems, (ISCAS 2008), 2789-2792 (2008).

[11] N. Kirman, M. Kirman, R. K. Dokania, J. Martinez, A. B. Apsel, M. A. Watkins, and D. H. Albonesi, "On Chip Optical Technology in Future Bus-Based Multicore Designs," IEEE Micro **27**, 56-66 (2007).

[12] A. Shacham, K. Bergman, and L. Carloni, "Photonic Networks-on-Chip for future generations of Chip Multiprocessors," IEEE Transactions on Computers **57**, 1246-1260 (2008).

[13] A. Liu, R. Jones, L. Liao, D. Samara-Rubio, D. Rubin, O. Cohen, R. Nicolaescu, and M. Paniccia, "A high-speed silicon optical modulator based on a metal-oxide semiconductor capacitor," Nature **427**, 615-618 (2004).

[14] W. M. Green, M. J. Rooks, L. Sekaric, and Y. A. Vlasov, "Ultra-compact, low RF power, 10 Gb/s silicon Mach-Zehnder modulator, "Opt. Express **15**, 13965-13971 (2007).

[15] Q. Xu, S. Manipatruni, B. Schmidt, J. Shakya, and M. Lipson, "12.5 Gb/s carrier-injection-based silicon micro-ring silicon modulators," Opt. Express **15**, 430-436 (2007).

[16] T Yin, R. Cohen, M. M. Morse, G. Sarid, Y. Chetrit, D. Rubin, and M. J. Paniccia, "31 GHz Ge n-i-p waveguide photodetectors on Silicon-on-Insulator substrate," Opt. Express **15**, 13965-13971 (2007).

[17] L. Chen, K. Preston, S. Manipatruni, and M. Lipson, "Integrated GHz silicon photonic interconnect with micrometer-scale modulators and detectors," Opt. Express **17**, 15248-15256 (2009).

[18] V. F. Pavlidis, and E. G. Friedman, "3-D Topologies for Networks-on-Chip," IEEE Transactions on Very Large Scale Integration (VLSI) Systems **15**, 1081-1090 (2007).

[19] P. Koonath, and B. Jalali, "Multilayer 3-D photonics in silicon," Opt.Express **15**, 12686-12691 (2007).

[20] L. Liao, "Low Loss Polysilicon Waveguides for Silicon Photonics," (Master's Thesis, MIT 1997).

[21] A. Saynatjoki, J. Riikonen, H. Lipsanen, "Optical waveguides on polysilicon-on-insulator," J. Mat. Sci: Materials in Elect. **14**, 417-420 (2003).

[22] K. Preston, B. Schmidt, and M. Lipson, "Polysilicon photonic resonators for large-scale 3D integration of optical networks," Opt. Express **15**, 17283-17290 (2007).

[23] G. Cocorullo, F. G. Della Corte, I. Rendina, C. Minarini, A. Rubino, and E. Terzini, "Amorphous silicon waveguides and light modulators for integrated photonics realized by low-temperature plasma-enhanced chemical-vapor deposition," Opt. Letters **21**, 2002-2004 (1996).

[24] M. J. A. de Dood, A. Polman, T. Zijlstra, and E. W. J. M. van der Drift, "Amorphous silicon waveguides for microphotonics," J. Appl. Phys. **92**, 649-653 (2002).

[25] A. Harke, M. Krause, and J. Muller, "Low-loss singlemode amorphous silicon waveguides," Electron. Lett. **41**, 1377-1379 (2005).

[26] D. K. Sparacin, R. Sun, A. M. Agarwal, M. A. Beals, J. Michel, L. C. Kimerling, T. J. Conway, A.T. Pomerene, D. N. Carothers, M. J. Grove, D. M. Gill, M. S. Rasras, S. S. Patel, and A. E. White, "Low Loss Amorphous Silicon Channel Waveguides for Integrated Photonics," in *Group IV Photonics, 2006, 3rd IEEE International Conference on*, pp. 255-257 (2006).

[27] Y. C. Wang, A. K. Zaitsev, C. L. Pan, and J. M. Shieh, "New low temperature poly-silicon fabrication technique by near infrared femtosecond laser annealing," *Conference on Lasers and Electro-Optics/International Quantum Electronics Conference and Photonic Applications Systems Technologies,* Technical Digest (CD) (Optical Society of America, 2004), paper CThD1.

[28] K. Preston, C. B. Poitras, M. O. Thompson and M. Lipson, "Photonics Devices in Low-Temperature Laser-Crystallized Deposited Silicon," *Conference on Lasers and Electro-Optics/International Quantum Electronics Conference and Photonic Applications Systems Technologies,* Technical Digest (CD) (Optical Society of America, 2010), paper CThW4.

[29] R. A. Street, *Hydrogenated Amorphous Silicon* (Cambridge University Press, Cambridge NY 1991).

[30] A. W. Fang, H. Park, O. Cohen, R. Jones, M. J. Paniccia, and J. E. Bowers, "Electrically pumped hybrid AlGaInAs-silicon evanescent laser," Opt. Express **14**, 9203-9210 (2006).

[31] G. Cocorullo, F. G. Della Corte, I. Rendina, C. Minarini, A. Rubino, and E. Terzini, "Amorphous silicon waveguides and light modulators for integrated photonics

realized by low-temperature plasma-enhanced chemical-vapor deposition," Opt. Letters **21**, 2002-2004 (1996).

[32] M. J. A. de Dood, A. Polman, T. Zijlstra and E. W. J. M. van der Drift, "Amorphous silicon waveguides for microphotonics," J. Appl. Phys. **92**, 649-653 (2002).

[33] A. Harke, M. Krause, and J. Mueller, "Low-loss singlemode amorphous silicon waveguides," Electron. Lett. **41**, 1377-1379 (2005).

[34] D. K. Sparacin, R. Sun, A. M. Agarwal, M. A. Beals, J. Michel, L. C. Kimerling, T. J. Conway, A. T. Pomerene, D. N. Carothers, M. J. Grove, D. M. Gill, M. S. Rasras, S. S. Patel, and A. E. White, "Low Loss Amorphous Silicon Channel Waveguides for Integrated Photonics," in *Group IV Photonics, 2006. 3rd IEEE International Conference on,* pp. 255-257 (2006).

[35] R. Sun, J. Cheng, J. Michel, and L. Kimerling, "Transparent amorphous silicon channel waveguides and high-*Q* resonators using a damascene process," Opt. Lett. **34**, 2378-2380 (2009).

[36] R. Sun, P. Dong, N. Feng, C. Hong, J. Michel, M. Lipson, and L. Kimerling, "Horizontal single and multiple slot waveguides: optical transmission at λ = 1550 nm," Opt. Express **15**, 17967-17972 (2007).

[37] F. G. Della Corte, M. E. Montefusco, L. Moretti, I. Rendina, and A. Rubino, "Study of the thermo-optic effect in hydrogenated amorphous silicon and hydrogenated amorphous silicon carbide between 300 K and 500 K at 1.55 μm," Appl. Phys. Lett **79**, 168-170 (2001).

[38] F. G. Della Corte, M. Gagliardi, M. A. Nigro, and C. Summonte, "In-guide pump and probe characterization of photoinduced absorption in hydrogenated amorphous silicon thin films," J. Appl. Phys **100**, 033104 (2006).

[39] D. J. Won, M. O. Ramirez, H. Kang, V. Gopalan, N. F. Baril, J. Calkins, J. V. Badding, and P. J. A. Sazio, "All-optical modulation of laser light in amorphous silicon-filled microstructured optical fibers," Appl. Phys. Lett. **91**, 161112 (2007).

[40] M. Zelikson, K. Weiser, A. Chack, and J. Kanicki, "Direct determination of the quadratic electro-optic coefficient in an a-Si:H based waveguide," Jour. Non Cryst. Sol. **198-200** 107-110 (1996).

[41] P. M. Fauchet, D. Hulin, R. Vanderhaghen, A. Mourchild, and W. L. Nighan Jr., "The properties of free carriers in amorphous silicon," J. Non-Cryst. Sol., **141**, 76-87 (1992).

[42] F. G. Della Corte, S. Rao, M. A. Nigro, F. Suriano, and C. Summonte, "Electro-optically induced absorption in α-Si:H/α-SiCN waveguiding multistacks," Opt. Express **16**, 754-7550 (2008).

[43] K. Ikeda, Y. Shen, and Y. Fainman, "Enhanced optical nonlinearity in amorphous silicon and its application to waveguide devices," Opt. Express **15**, 17761-17771 (2007).

[44] H. Yamada, M. Shirane, T. Chu, H. Yokoyama, S. Ishida, and Y. Arakawa, "Nonlinear-Optic Silicon-Nanowire Waveguides," Jpn. J. Appl. Phys. **44**, 6541-6545 (2005).

[45] H. K. Tsang, C. S. Wong, T. K. Liang, I. E. Day, S. W. Roberts, A. Harpin, J. Drake, and M. Asghari, "Optical dispersion, two-photon absorption and self-phase modulation in silicon waveguides at 1.5 um wavelength," Appl. Phys. Lett **80**, 416-418 (2002).

[46] M. Dinu, F. Quochi, and H. Garcia, "Third-order nonlinearities in silicon at telecom wavelengths," Appl. Phys. Lett. **82**, 2954-2956 (2003).

[47] G. W. Rieger, K. S. Virk, and J. F. Young, "Nonlinear propagation of ultrafast 1.5um pulses in high-index-contrast silicon-on-insulator waveguides," Appl. Phys. Lett **84**, 900-902 (2004).

[48] O. Boyraz, T. Indukuri, and B. Jalali, "Self-phase-modulation induced spectral broadening in silicon waveguides," Opt. Express **12**, 829-834 (2004).

[49] E. Dulkeith, Y. A. Vlasov, X. Cheng, N. C. Panoiu, and R. M. Osgood Jr, " Self-phase-modulation in submicron silicon-on-insulator photonic wires," Opt. Express **14**, 5524-5534 (2006).

[50] H. Fukuda, K. Yamada, T. Shoji, M. Takahashi, T. Tsuchizawa, T. Watanabe, J. Takahashi, and S. Itabashi, "Four-wave mixing in silicon wire waveguides," Opt. Express **13**, 4629-4637 (2005).

[51] L. Yin, and G. P. Agrawal, "Impact of two-photon absorption on self-phase modulation in silicon waveguides," Opt. Lett **32**, 2031-2033 (2007).

[52] S. Roy, S. K. Bhadra, and G. P. Agrawal, "Femtosecond pulse propagation in silicon waveguides: Variational approach and its advantages," Opt. Communications **281**, 5889-5893 (2008).

[53] P. Apiratikul, A. M. Rossi, and T. E. Murphy, "Nonlinearities in porous silicon optical waveguides at 1550 nm," Opt. Express **17**, 3396-3406 (2009).

[54] G. P. Agrawal, *Nonlinear Fiber Optics,* (Academic Press, New York, Third Edition 2001).

[55] V. R. Almeida, R. R. Panepucci, and M. Lipson, "Nanotaper for compact mode conversion," Opt. Lett. **28**, 1302-1304 (2003).

[56] R. A. Soref and B. R. Bennet, "Electrooptical effect in silicon," IEEE J. Quantum Electron. **23**, 123-129 (1987).

[57] V. R. Almeida, C. A. Barrios, R. R. Panepucci, and M. Lipson, "All-optical control of light on a silicon chip," Nature, **431**, 1081-1083 (2004).

[58] K. Preston, P. Dong, B. Schmidt, and M. Lipson, "High-speed all-optical modulation using polycrystalline silicon microring resonators," Appl. Phys. Lett. **92**, 151104 (2008).

[59] J. Tauc and Z. Vardeny, "Picosecond transient optical phenomena in a-Si:H," Crit. Rev. Solid State Mater. Sci **16**, 403-416 (1990).

[60] K. Narayanan, A. W. Elshaari, and S. F. Preble, "Broadband all-optical modulation in hydrogenated-amorphous silicon waveguides," Opt. Express **18**, 9809-9814 (2010).

[61] A. C. Turner, C. Manolatou, B. S. Schmidt, M. Lipson, M. A. Foster, J. E. Sharping, and A. L. Gaeta, "Tailored anomalous group-velocity dispersion in silicon channel waveguides," Opt. Express **14**, 4357-4362 (2006).

[62] B. Kuyken, S. Clemmen, S. K. Selvaraja, W. Bogaerts, D. Van Thourhout, P. Emplit, S. Massar, G. Roelkens, and R. Baets, "On-chip parametric amplification with 26.5 dB gain at telecommunication wavelengths using CMOS-compatible hydrogenated amorphous silicon waveguides," Opt. Lett (to be published)

[63] M. A. Foster, A. C. Turner, R. Salem, M. Lipson, and A. L. Gaeta, "Broad-band continuous-wave parametric wavelength conversion in silicon nanowaveguides," Opt. Express **15**, 12949-12958 (2007).

[64] B. Schmidt, Q. Xu, J. Shakya, S. Manipatruni, and M. Lipson, "Compact electro-optic modulator on silicon-on-insulator substrates using cavities with ultra-small modal volumes," Opt. Express **15**, 3140-3148 (2007).

[65] A. Liu, L. Liao, D. Rubin, H. Nguyen, B. Ciftcioglu, Y. Chetrit, N. Izhaky, and M. Paniccia, "High-speed optical modulation based on carrier depletion in a silicon waveguide," Opt. Express **15**, 660-668 (2007).

[66] P. J. Winzer and R.J. Essiambre, "Advanced Optical Modulation Formats," In Proc. IEEE, 94, 952-985 (2006).

[67] L. Zhou, H. Chen, and A. W. Poon, "On-Chip NRZ-to-PRZ Format Conversion Using Narrow-Band Silicon Microring Resonator-Based Notch Filters," J. Lightwave Technol. **26**, 1950-1955 (2008).

[68] L. Zhang, Y. Li, J. Yang, R. G. Beausoleil, and A. E. Willner, "Creating RZ Data Modulation Formats Using Parallel Silicon Microring Modulators for Pulse Carving in DPSK," in *C* (Optical Society of America, 2008), paper CWN4.

[60] R. Ramaswami and K. N. Sivarajan, *Optical Networks: A Practical Perspective*, (Morgan Kaufmann, 2002).

[70] Q. Xu, "Controlling the flow of light on chip with microring- resonator-based silicon photonic devices," (PhD Thesis, Cornell University 2007).

[71] N. Sherwood-Droz, H.Wang, L. Chen, B. G. Lee, A. Biberman, K. Bergman, and M. Lipson, "Optical 4x4 hitless silicon router for optical networks-on-chip (NoC)," Opt. Express **16**, 15915-15922 (2008).

[72] S. F. Preble, Q. Xu, B. S. Schmidt, and M. Lipson, "Ultrafast all-optical modulation on a silicon chip," Opt. Lett. **30**, 2891-2893 (2005).

[73] P. J.Winzer, R. J. Essiambre, "Receivers for advanced optical modulation formats," in *Lasers and Electro-Optics Society, 2003. LEOS 2003. The 16th Annual Meeting of the IEEE*, 27-28 Oct. 2003.

[74] J. Cardenas, C.B. Poitras, J.T. Robinson, K. Preston, L. Chen, M. Lipson, "Low loss etchless silicon photonic waveguides," Optics Express **17**, 4752-4757 (2009).

[75] S. K. Selvaraja, W. Bogaerts, D. Vanthourhout, M. Schaekers, "Thermal Trimming and tuning of hydrogenated amorphous silicon nanophotonic devices," Appl. Phys. Lett. **97**, 071120 (2010).